CLAUDIA PATRICIA VALDÉS ESCOBAR

NEW LASER SPECKLE METHODS FOR *IN VIVO* BLOOD FLOW IMAGING AND MONITORING

NEW LASER SPECKLE METHODS FOR *IN VIVO* BLOOD FLOW IMAGING AND MONITORING

CLAUDIA PATRICIA VALDÉS ESCOBAR

Medical Optics Group
ICFO - Institut de Ciències Fotòniques
Universitat Politècnica de Catalunya

DiMABio
Institut Fresnel
Aix-Marseille Université

October 2014

SUPERVISORS:
Dr. Turgut Durduran
Dra. Anabela Da Silva

A Efrain,
Sebastian y Beatrix

ABSTRACT

Blood flow and its regulation, as well as hemodynamics in general, are important for the health of tissues, and hence, the measurement of these quantities has many applications in research and clinical environments. Various optical techniques are attractive for the measurement of blood flow since they are often non- or minimally-invasive, continuous and are relatively inexpensive. During my PhD I have contributed to the monitoring of blood flow in experimental animal models with the construction of a multimodal device, based on laser speckle flowmetry and optical intrinsic signals, capable of measuring superficial microvascular cerebral blood flow, blood oxygenation and blood volume for translational research. This device was applied in animal models of ischemic stroke and is flexible to be modified and used for other purposes. In doing so, I have developed new experimental methods and image processing protocols that allowed us to perform longitudinal studies where the animal can be removed from the device several times. Furthermore, this device has been used as a tool in a multi-disciplinary study to understand the role of the Mannose-binding lectin protein in reperfusion injury after an ischemic stroke in animal models. This, then led to the main contribution of this work which is the development of the speckle contrast optical spectroscopy and tomography, a new non-invasive, optical technique for deep blood flow measurement that paves the way for deeper and three dimensional imaging of blood flow. This new method was first developed from a theoretical perspective, then it was validated in tissue simulating phantoms and demonstrated to be feasible in measurements on the human arm muscle. Overall, these contributions will allow the development of cost-effective, non-invasive tomographic methods for the measurement of blood flow even in humans.

RESUMEN

El flujo sanguíneo y su regulación, así como la hemodinámica en general, son parámetros importantes para determinar el estado de salud de los tejidos; por esto, su medición tiene numerosas aplicaciones en los ámbitos clínico y de investigación. Varias técnicas ópticas resultan atractivas para la medición del flujo sanguíneo dado su carácter no invasivo o mínimamente invasivo, continuo y relativamente económico. Durante mi trabajo doctoral he contribuido con la monitorización del flujo sanguíneo en modelos de experimentación animal, con la construcción de un dispositivo multimodo basado en la flujometría de speckle láser (laser speckle flowmetry, LSF) y las señales ópticas intrínsicas (optical intrinsic signals, OIS), capaz de medir flujo sanguíneo de la microvasculatura superficial del cerebro, oxigenación sanguínea y volumen sanguíneo, en investigación traslacional. Este dispositivo fue aplicado en modelos animales de infarto cerebral; sin embargo, es flexible y puede ser modificado y utilizado para otros propósitos. Así pues, he desarrollado nuevos métodos experimentales y protocolos de procesamiento de imágenes que nos permitieron llevar a cabo estudios longitudinales, donde los animales pueden ser removidos del dispositivo en repetidas ocasiones. Adicionalmente, este dispositivo fue utilizado como herramienta en un estudio multidisciplinario para entender el papel de la proteína lectina de unión a la manosa (MBL) en las lesiones por isquemia-reperfusión después de un infarto cerebral en modelos animales. Este estudio dio origen a la mayor contribución de este trabajo, siendo esta el desarrollo de la espectroscopía y tomografía óptica de contraste de speckles; una novedosa técnica óptica, no invasiva para medición de flujo sanguíneo profundo que allana el camino para la obtención de imágenes tridimensionales de flujo sanguíneo más profundo. Este nuevo método, se desarrolló primero desde una perspectiva teórica, y posteriormente se validó en phantoms the tejido biológico y demostró ser factible en mediciones realizadas en el músculo del antebrazo de un paciente. En general, estas con-

tribuciones permitirán el desarrollo de métodos tomográficos no invasivos y rentables para la medición de flujo sanguíneo, exensibles incluso a seres humanos.

CONTENTS

LIST OF FIGURES

ACRONYMS

ASL-MRI	arterial spin labeled magnetic resonance imaging
BFI	blood flow index
CBF	cerebral blood flow
CCD	charge-coupled device
CDE	correlation diffusion equation
CTE	correlation transport equation
CW	continuous wave
FOV	field-of-view
DCS	diffuse correlation spectroscopy
DCT	diffuse correlation tomography
DE	diffusion equation
DOT	diffuse optical tomography
DP	differential pathlength
DWS	diffuse wave spectroscopy
KO	knocked-out
LDF	laser Doppler flowmetry

LED	light emitting diode
LSF	laser speckle flowmetry
MBL	Mannose-binding lectin
MCAO	middle cerebral artery occlusion
MFP	mean free path
MRI	magnetic resonance imaging
MSD	mean-square displacement
OIS	optical intrinsic signal imaging
PET	positron emission tomography
PID	peri-infarct depolarization
RTE	radiative transport equation
ROI	region of interest
S-D	source-detector separation
sCMOS	scientific complementary metal-oxide-semiconductor
SCOS	speckle contrast optical spectroscopy
SCOT	speckle contrast optical tomography
SNR	signal-to-noise ratio
SPECT	single photon emission computed tomography
tMCAO	temporal middle cerebral artery occlusion
TMFP	transport mean free path
TRS	time resolved spectroscopy
TTC	Triphenyl tetrazolium chloride
WT	wild type

SYMBOLS

α	ratio of moving scatterers to the total number of scatterers
κ	speckle contrast
ϵ	absorptivity
λ	wavelength
μ_a	absorption coefficient
μ_s	scattering coefficient
μ_s'	reduced scattering coefficient
μ_t	total attenuation coefficient
σ	standard deviation
σ^2	variance
τ	delay time
τ_c	decorrelation time
A	absorbance
c	speed of light in vacuum
C	concentration
D	photon diffusion coefficient
D_B	Brownian diffusion coefficient
$\vec{E}$	Electric field
g	anisotropy factor
G_1	field autocorrelation function

g_1	normalized field autocorrelation function
G_2	intensity autocorrelation function
g_2	normalized intensity autocorrelation function
I	Intensity
$\vec{K}_{in}$	Incident wave vector
$\vec{K}_{sc}$	Scattered wave vector
L	radiance
n	refractive index
$\vec{q}$	scattering vector
R_F	reflection Fresnel coefficient
T	exposure time
v	speed of light in a medium

1

INTRODUCTION

Human body welfare and its proper functioning rely on the orchestrated work of the body systems: nervous, endocrine, skeletal, muscular, cardiovascular, lymphatic, among others. In particular, the cardiovascular system, composed of the heart, blood and the blood vessels (arteries, veins and capillaries) plays an important role as it guarantees the transport of oxygen, nutrients and hormones that the tissues and organs require to perform its duties; as well as the clearance of the metabolic end products, and carbon dioxide from the tissues. Apart from the transportation role, the cardiovascular system contributes to maintain the homeostasis, i. e., keeping the equilibrium status of the body. This is done by regulating or adjusting the *blood flow*, according to the conditions of the body at a given time and the specific needs of an organ, even in case of a disease or any other abnormal situation.

According to this, blood flow is an important physiological parameter that constitutes an indicator of the proper functioning of the body/organs or an alteration thereof. Hence, measuring the blood flow provides essential information for the understanding of the body/organ functions, the diagnosis or the evolution of a disease [1]. These measurements are relevant in studies of brain, muscular tissue, skin, eye retina and cancerous tumours.

Special attention is paid to the brain hemodynamics, due to the fact that any disruption in the cerebral blood flow, will lead to brain damage and consequently, impairment of the body functions controlled by the brain, including motor, sensory, visual functions. Having information about cerebral blood flow (CBF) is ex-

tremely useful to the diagnosis and monitoring of many diseases such as stroke, ischemic injuries, traumatic brain injury, as well as neurodegenerative diseases such as the Alzheimer's [2, 3].

A stroke, is the rapid loss of cerebral functions (brain damage) due to a critical change in the CBF, i. e., blood supply in time, and it is classified into two types namely ischemic and hemorrhagic. When there is a reduction or complete cessation of the blood supply, it is called *ischemic stroke*. On the other hand, if the blood goes out of the vessels, it is called a *hemorrhagic stroke*. For the purposes of this work, only the ischemic stroke is being considered.

Ischemic stroke arises mainly due to the blockage of a major artery, i. e., the blockage of cerebral blood flow to a region of the brain. It has a large socioeconomic impact as it is the leading cause of morbidity and long term disability in western hemisphere and is among the leading causes of death [4]. Not only that, but also the cost for rehabilitation of people who have suffered stroke is expected to rise to trillions of euros in the next fifty years.

Stroke is a very complex and heterogeneous condition and despite decades of massive research efforts there is still an unmet need for new imaging modalities both in humans and in experimental animal models [5]. Animal modeling of ischemic stroke serves as an indispensable tool to investigate mechanisms of ischemic cerebral injury, and to develop novel anti-ischemic treatments. Experimental ischemic stroke models, usually carried out in rodents, contribute to our understanding of the events occurring in the ischemic and the reperfused brain [6]. For example, this kind of studies have led to the development of the recombinant tissue plasminogen activator (rt-PA), which nowadays, is the unique approved and efficient treatment (under special conditions) for ischemic stroke.

Nevertheless, there are many cases in which the translation from a procedure from animals to humans has failed [7, 8]. One promising strategy for improving this translation is an increased role for neuroimaging methods that are applicable both in rodents and humans [9]. Since ischemic stroke arises mainly due to the blockage

of a major artery, i.e. due to the blockage of CBF to a region of the brain, the measurement of the local CBF and its management play a crucial role in understanding stroke pathophysiology and stroke care.
Currently, the measurement of CBF in humans is done by several methods [10] where the only non-invasive, local, microvascular and whole-brain imaging method is the arterial spin labeled magnetic resonance imaging (ASL-MRI). In order to have a direct comparison, the same method has to be adopted in animal models, but the use of this technique in rodents is not practical for large throughput studies because of their brain size, which needs a high resolution and a high signal to noise ratio, only possible with specialized high field magnets [11], making the technique very expensive and relatively inaccessible. There are other methods used in animal research, many are highly invasive, such as auto-radiography techniques where tracer accumulation is measured after dissecting the brain. In contrast to this, it is preferred to have an imaging tool that allows the monitoring of CBF in the whole brain with a hundreds of microns spatial resolution in a continuous, safe and repeatable fashion.This imaging tool should be capable of semi/non-invasive, three dimensional depth resolved imaging in addition to being fast and cost effective. Optical imaging methods are found to posses most of the above features, making them promising imaging tools [12].

The commonly used imaging modality to measure CBF during temporal ischemia in rodents is the laser Doppler flowmetry (LDF) [13] which only gives information about the point of the brain where the fiber optic probe is positioned and relies on single scattering with limited depth penetration (<1mm). LDF can also be utilized for imaging by scanning the probe but as of today it is prohibitively slow. Other technique that is able to measure relative changes in CBF is the laser speckle flowmetry (LSF) [14], which gives wide-field information but also penetrates $\leqslant$1mm to the cortex, without giving information of the whole brain hemodynamics and, as LSF, it often requires thinning of the skull. Optical intrinsic signal imaging (OIS) is another imaging modality that measures blood oxygen saturation and total hemoglobin concentration [15]. None of the above modalities is capable measuring deep tissue

blood parameters.

There are also other optical techniques that allow imaging the rodent's brain with good resolution and with larger depth penetration like 2-photon microscopy [16], optical coherence tomography (OCT) [17] and photoacoustic tomography (PAT) [18]. All the above methods either give structural information with limited functional information or have a very limited field of view. Recently, laminar optical tomography (LOT) [19] was introduced allowing noncontact imaging with 100-200μm resolution and with a 1.5 mm penetration depth. The key difference between LOT and other techniques is that it employs a dense scanning of small source-detector separations for data acquisition and single- and/or few-scattering but it still does not give CBF information. It also requires the use of the more complex photon transport model.

In order to measure deep blood flow, diffuse optical technologies, such as diffuse correlation spectroscopy/tomography (DCS/DCT) have been proven to be an appropriate choice. Although it is possible to image the rat brain through intact skull, the axial and depth resolution is ~0.5mm, and in general, it is a few point technique, which for a tomographic application makes it relatively slow and expensive, limiting the use of this type of techniques in the rodent animal research [10]. Future technological advances may change this and our group is actively working on this topic.

The aim of this thesis is twofold. First, I present an LSF-OIS imaging device to monitor ischemic stroke in small animal models. However, this method is limited to superficial imaging of blood flow, which necessitates the invention of a new imaging modality capable of measuring deep tissue blood flow. The second aim of this thesis is the development of such deep tissue imaging method by integrating selected features of laser speckle flowmetry (LSF) and diffuse correlation spectroscopy (DCS).

A multimodal device based on LSF and optical intrinsic signal imaging (OIS) for the simultaneous measurement of CBF, blood oxygenation and hemoglobin concentration was developed. This system was optimized for ischemic stroke longitudinal studies in

rodent models. It has been shown that after an ischemic stroke, the reperfusion, i. e., the restoration of blood supply to the affected area, will not restore the normal function of the brain, but will cause inflammation and in some cases increase the damage originally caused by the stroke. It has been found that subjects with reduced amount of a protein called Mannose-binding lectin (MBL), will have better outcome after suffering an ischemic stroke. We employed the LSF-OIS system to study the role of the MBL protein in the first few hours following the reperfusion after an ischemic stroke caused by occlusion of the middle cerebral artery in mice.

In LSF the tissue to be imaged for its blood flow is homogeneously illuminated with a coherent light source and the scattered light intensity (speckles) is collected using an array detector, e. g., charge-coupled device (CCD) camera as depicted in Figure 1.1a. LSF provides fast acquisition and comprises inexpensive source and detector. Nevertheless, due to the uniform illumination, it only probes superficial tissues, typically 1 mm. On the other hand, deep tissue imaging is possible by using DCS, which is based on photon diffusion principle. In DCS, the sample is illuminated with a point source and the random fluctuations in intensity, induced by the blood flow, are measured using an optical detector localized at a given distance from the source (Figure 1.1b). Depending on the S-D, the blood flow at different depths is measured. One of the disadvantages of DCS is the need of expensive single photon counting detectors in addition to have a slow data acquisition.

I present a new deep tissue blood flow imaging method, which we called speckle contrast optical spectroscopy (SCOS). In SCOS we integrate the point source illumination as used in DCS, with the array detectors as used in LSF, resulting in an inexpensive, fast, deep tissue blood flow imaging system (Figure 1.1c). SCOS inherits the quantitative deep tissue blood flow capabilities of DCS and the fast acquisition features from LSF. The use of two dimensional array of detectors, allows SCOS to measure a wide field-of-view (FOV) in a single shot. Since there are millions of pixels in a camera sensor, multiple pixels could be combined to form one detector resulting in a greater improvement of the signal-to-noise ratio (SNR). I developed a photon diffusion model based method to quantitatively recover the blood flow. I also present a noise

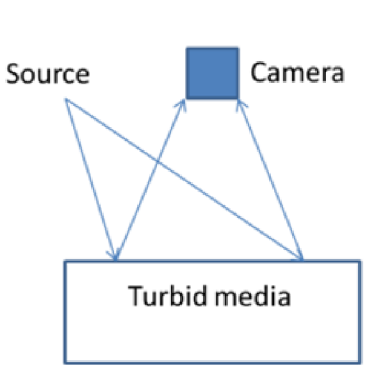

(a) Laser speckle flowmetry (LSF).

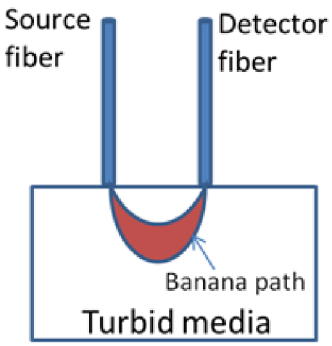

(b) Diffuse correlation spectroscopy (DCS).

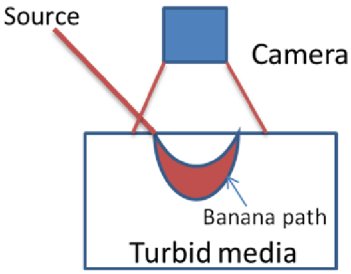

(c) Speckle contrast optical spectroscopy (SCOS).

Figure 1.1: A novel imaging method for deep tissue blood flow (SCOS).

correction method to account for the noises associated with the detectors, which is crucial while employing SCOS for *in vivo* measurements.

When there is heterogeneous distribution of blood flow, it is desirable to have a three dimensional tomographic imaging method which samples the tissue using multiple source and detector locations. I introduce a novel tomographic method called speckle contrast optical tomography (SCOT), where an inversion methodology is integrated to the principles of SCOS. The inversion methodology involves the algorithm/computational procedures to recover the three dimensional distribution of blood flow using the measured intensity fluctuations. I demonstrated SCOT in tissue mim-

icking phantoms and validated SCOS in human tissue.

The outline of the thesis is as follows. Following the introduction, the second chapter includes the physical models and the mathematical background that underlie the methods developed in this thesis. The third chapter is devoted to the LSF-OIS multimodal device, its instrumentation, the image processing and coregistration techniques. I also present experimental methods developed for the ischemic stroke animal studies and finally, the study regarding the effect of MBL protein in the reperfusion following an ischemic stroke in mice.

In chapter 4, I present a novel deep tissue blood flow imaging method, speckle contrast optical spectroscopy (SCOS). SCOS principles based on photon diffusion model, along with the necessary optical instrumentation are presented. Afterwards, the experiments in tissue mimicking phantoms and *in vivo* for the validation of SCOS are described. Based on SCOS principles, I present a novel tomographic imaging method, SCOT, along with the necessary inversion algorithm, and its validation in tissue mimicking phantoms. Finally, in chapter 5, I present the conclusions drawn from the studies performed in this work.

This thesis has been done under the Europhotonics Erasmus Mundus Joint Doctorate program between ICFO and Institute Fresnel in France, with the supervision of Prof. Dr. Turgut Durduran and Dr. Anabela Da Silva, respectively. The animal experiments and the MBL study were done in collaboration with Dr. Anna M. Planas from the Department of Brain Ischemia and Neurodegeneration at the Institute of Biomedical Research of Barcelona (IIBB). For the development of SCOT we have collaborated with Prof. Dr. Joseph Culver from the Optical radiology Lab at the Washington University at Saint Louis, USA.

2

THEORETICAL BACKGROUND

Optical methods for probing tissues rely on light-tissue interactions. In our case, the medium is illuminated with a light source, and, transmitted or reflected light that has undergone single or multiple scattering is collected using detectors. In order to extract optical properties from this detected light, we need a mathematical model, based on physical principles, representing the propagation of the light inside the sample by assuming the optical properties of sample are known.

One of the models to describe light propagation in a turbid medium, such as tissues, where scattering, absorption and emission take place, and neglecting the polarization and the coherence effects, is the radiative transport equation (RTE). The RTE describes the light propagation in the medium as an energy balance equation where a beam of radiation gains energy from source, losses energy due to absorption and redistributes energy by scattering in the medium.

The RTE is an integro-differential equation where its solution gives the spectral radiance of the propagating beam at each spatial coordinate in a given direction and at a given time. Solving the RTE either analytically or numerically for the imaging applications in multiple scattering medium, like tissue, is a difficult task. Hence, a simplified form of the RTE, called diffusion equation (DE), is adopted based on the fact that the number of scattering events dominate the absorption events under certain conditions that pertain to deep tissue imaging. These two models account for the propagation of photons when the medium is considered static,

that is, the particles responsible for the scattering are not moving. However, in the biological tissues, apart from the static scatterers, there are moving scatterers, e. g., the red blood cells. Thus, the motion of the scatterers has to be incorporated to the RTE or the DE in order to make those models useful for imaging the dynamics, e. g., blood flow in tissue.

In order to achieve this, we first consider the so-called speckle phenomena where a coherent radiation interacting with a medium composed of randomly distributed particles, like tissue, produces random interference patterns of scattered light called speckle pattern. This pattern will fluctuate if the scattering particles are moving, which constitute the dynamic speckles. Detecting these intensity fluctuations over time, will provide information about the dynamic properties of the tissue, in particular blood flow information. Depending on how the speckles are detected and how the signal is analysed, different methods have been developed to measure the dynamics of the tissue, although their foundations are the same [20]: laser Doppler, photon correlation spectroscopy and laser spec-kle methods. Laser Doppler works in the frequency domain measuring the broadening of the power spectrum of the signal, photon correlation spectroscopy uses the time autocorrelation properties of the speckle and the laser speckle methods make use of statistical quantities like contrast (ratio of variance to mean of the speckles) to measure the dynamic properties of the medium, i. e., information about the motion of the scatterers.

Based on the decay of the temporal correlation function measured from the light that has travelled through a medium, a different propagation model was proposed which considers the transport of the correlation of the field in a similar way the RTE considers the transport of photons, and which constitute the correlation transport equation (CTE). Again, as in the case of the RTE, the CTE could be simplified for highly scattering media, resulting in the correlation diffusion equation (CDE). CDE models the propagation of the field autocorrelation function with a mathematical structure similar to that of the DE, but including an additional term that accounts for the dynamics of the scatterers in addition to its dependencies on the optical properties. The first section of this

chapter is dedicated to the detailed theory of above light propagation models in tissue.

All the mathematical models based on physical principles, i. e., RTE, DE, CTE and CDE, as explained above can be categorized as forward models. By assuming the optical and dynamic properties of the medium are known it is possible to solve the equation either numerically or analytically to obtain photon fluence rate or field autocorrelation, etc. But in optical imaging problems we are interested on extracting the optical or dynamic properties at each point in the medium from the measurements of the scattered light intensity that is made on the surface of the medium. Any algorithm or mathematical model which achieves this is termed as the inversion problem which is in fact developed based on the forward model. One of the difficulties encountered while developing the inverse model is the nonlinearity which is quite common to many optical imaging problems. In such scenarios, a linearization method is often adopted which results in the so-called sensitivity model (Jacobian) which relates the sensitivity of the measurements to the sensitivity of the dynamic properties in the medium. We will explain how sensitivity model along with forward model constitute the inversion model in the subsequent sections of this chapter.

2.1 LIGHT PROPAGATION IN BIOLOGICAL TISSUES

Light interaction in biological tissues can be described by three main processes: reflection, absorption and scattering. When light arrives to the tissue, some light is reflected by the surface, and the rest is transmitted, where, depending on its optical properties, light is going to be absorbed and/or scattered. Usually, biological tissues exhibit both scattering and absorption effects, and are considered *turbid media*. Biological tissues are compound of a large number of cells and organelles, causing the scattering while different bands of absorption due to its components: water, lipids, hemoglobin, melanin.

The optical properties of a turbid medium can be quantified on the distance light can travel into it without being absorbed or scat-

tered, and it is illustrated in Figure 2.1. For an absorbing medium, the inverse of the distance light travels within the medium is defined as the *absorption coefficient*, μ_a [cm^{-1}]. On the other hand, for a scattering medium, the inverse of the distance that light travels within the medium between two scattering events is the *scattering coefficient*, μ_s [cm^{-1}]. For turbid media, we will define a *total attenuation coefficient*, defined as the sum of the absorption and scattering coefficients, μ_a and μ_s: $\mu_t = \mu_a + \mu_s$. Hence, the inverse of μ_t, represents the mean free path (MFP) between two consecutive interactions:

$$\text{MFP} = \frac{1}{\mu_t} = \frac{1}{\mu_a + \mu_s}. \tag{2.1}$$

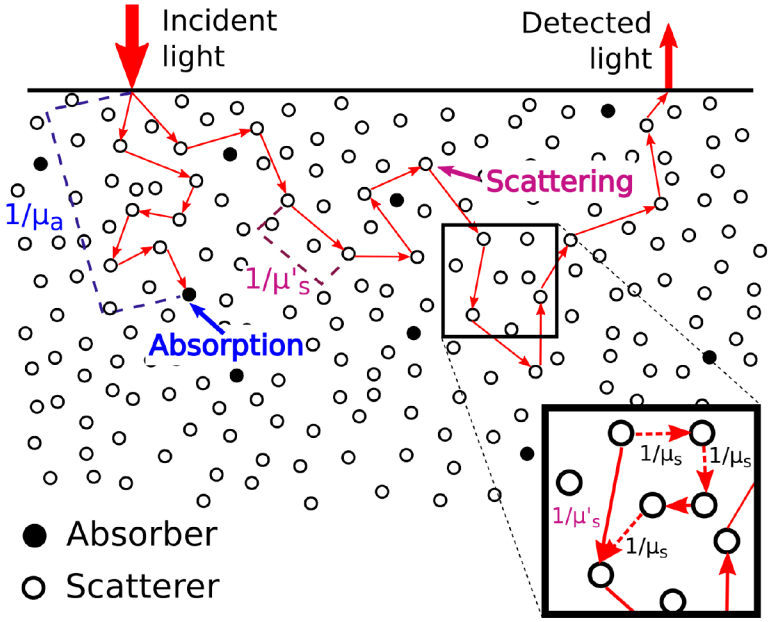

Figure 2.1: Schematic of the interaction processes of light with a turbid medium.

Depending on how far light has penetrated into the medium, we can define some scattering regimes as seen in Figure 2.2: the ballistic regime, in which photons travel in the direction of the incident beam and where single scattering events takes place; a transition regime in which the number of scattering events increases and a random walk regime, in which the initial propagation direction

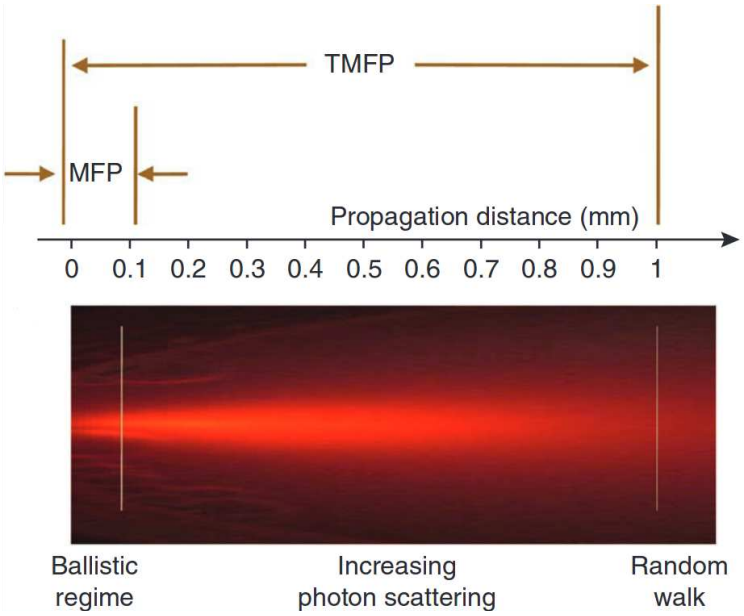

Figure 2.2: Simplified metrics of photon propagation in tissue. Schematic depiction of MFP and TMFP (top) and of photon propagation (bottom). The scale in physical dimensions is indicative of an average tissue with a reduced scattering coefficient of 10 cm^{-1}. This scale will vary depending on the tissue and the wavelength used. Reprinted by permission from Macmillan Publishers Ltd: Nature Methods [21], ©2010.

has been completely randomized and where multiple scattering events take place. The direction of propagation is described by the anisotropy factor, g, representing the amount of forward direction kept after each single scattering event. In the case of biological tissues this change in direction is predominantly in the forward direction and g takes values between 0.8 and 1.

In the ballistic regime, approximately within ~ 1 MFP distance travelled into the medium, it is considered that light only experiences scattering by one particle, that is, that the intensity scattered by M particles is M times the intensity scattered by one single particle. This relation is kept as long as each particle is receiving radiation only from the original light beam [22]. In this regime, when a photon is absorbed or scattered, after travelling a distance,

d, it can be thought as it has been removed from the collimated incident beam causing a decay of the initial light intensity, I_0. This attenuation in intensity, I_d, is represented by the *Beer-Lambert law*, which, within linear and single scattering regimes, states:

$$I(d) = (1 - R_F) I_0 \exp(-\mu_t d), \tag{2.2}$$

where R_F is the reflection Fresnel coefficient at the interface.

In the multiple scattering regime, the light received by each particle comes from scattered light from other particles located before (or even after) and sometimes far from the initial propagation direction. In order to take into account the scattering and the propagation direction, i. e., to relate the scattering coefficient of an isotropic particle to that of an isotropic particle [23], a *reduced scattering coefficient*, $\mu_s' = \mu_s(1 - g)$ [cm^{-1}], has been defined. The inverse of μ_s' corresponds to the transport mean free path (TMFP) which is the distance travelled into the medium for the light propagation to be completely randomized, which allows to describe the motion of photons as a random walk. This μ_s' describes the motion of the photons using many steps of size $1/\mu_s$. This is the principle used by diffuse optics which accepts that light propagation over long distances in tissues is well approximated as a diffusive process [24]. Collectively, these approaches allow the researchers to obtain information about blood oxygenation, blood volume as well as the blood flow [10].

2.1.1 *Model for light propagation in turbid media*

One of the models to describe the photon propagation in turbid media is the transport theory, in which it is possible to define a radiative transport equation for the radiance and hence for the intensity, being this the measurable parameter [25]. This linear integro-differential equation is based on the conservation of energy principle and represents the propagation of a collimated beam of radiance through an absorbing, scattering and emitting medium, without considering the effects of coherence and polarization.

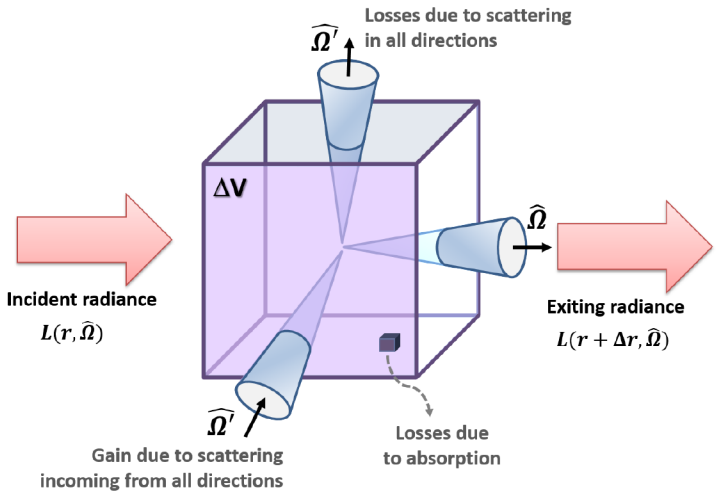

Figure 2.3: Illustration of the processes that affect a beam of light propagating in a volume, ΔV, and that are included in the RTE.

The simplest representation of light propagation consists on imagining a volume, ΔV, through which an initial incident radiance $L(\mathbf{r},\hat{\Omega})$ [W m^{-2} sr^{-1}], propagates a distance Δr in direction $\hat{\Omega}$, at a given time, t, as seen in Figure 2.3 an its mathematical representation is given by the linear transport equation for photons:

$$\begin{aligned}\frac{1}{v}\frac{\partial L(\mathbf{r},\hat{\Omega},t)}{\partial t}+\nabla\cdot L(\mathbf{r},\hat{\Omega},t)\hat{\Omega} = &-\mu_t L(\mathbf{r},\hat{\Omega},t)\\ &+\mu_s\int L(\mathbf{r},\hat{\Omega}',t)f(\hat{\Omega},\hat{\Omega}')d\hat{\Omega}'\\ &+S(\mathbf{r},\hat{\Omega},t)\end{aligned}\tag{2.3}$$

When the light propagates inside a medium with refractive index n, at a velocity $v = c/n$, its radiance might increase or decrease depending on the properties of the medium and the different light-matter interactions that might take place inside. The changes in radiance inside the volume are represented in Equation 2.3 by the terms on the left. The first one corresponds to the rate of change between the number of photons entering the volume and those leaving it and the second represents the flux of photons along direction $\hat{\Omega}$. In the right side, we find the representation of the different interactions within the volume. There

could be loss of photons due to absorption in the medium or due to scattering of the photons out of the beam and this is represented by the first term on the right side of Equation 2.3, where μ_t is the total attenuation coefficient as described previously. Also there could be an increase of photons due to photons scattered into the beam, which corresponds to the second term on the right, where $f(\hat{\Omega}, \hat{\Omega}')$ is the normalized phase function, representing the probability of scattering into direction $\hat{\Omega}$ from direction all directions $\hat{\Omega}'$. The third term, is related to photons added by a source inside the medium, where $S(\mathbf{r}, \hat{\Omega}, t)$ represents its spatial and angular distribution.

The photon fluence and the photon flux can be defined in terms of the irradiance by:

$$\Phi(\mathbf{r}, t) = \int L(\mathbf{r}, \hat{\Omega}, t) d\hat{\Omega} \tag{2.4}$$

and

$$\mathbf{J}(\mathbf{r}, t) = \int \hat{\Omega}\, L(\mathbf{r}, \hat{\Omega}, t) d\hat{\Omega} \tag{2.5}$$

respectively.

Getting solutions for the RTE (Equation 2.3) would help in obtaining information of the medium through which light has travelled but solving it is usually very complicated analytically and even numerically. Instead, an approximation called the *diffusion approximation* is adopted, as explained below.

2.1.2 *Diffusion approximation for photon propagation*

When a collimated beam enters a tissue, the photons have a well-defined propagation direction, but as they are scattered multiple times by the scatterers in the tissue, this directionality is lost and their movement can be described as a diffusive process. In other words, the diffusion assumes that the diffusing quantity, the radiant energy, does not have a preferential direction. This condition is only fulfilled once the photons have travelled one TMFP $= 1/\mu_s'$

in a highly scattering media, where the $\mu_s' >> \mu_a$, i. e., the number of scattering events is much higher that the absorption events.

One of the standard methods to approximate the RTE is the P_N approximation [26]. Here I will follow the way it has been presented by Boas [27]. In this method, the radiance, L, the phase function, f and the source, S, are expanded in spherical harmonics $Y_{l,m}$ up to the $l = N$ term. If it is assumed that $\mu_s >> \mu_a$, the phase function is not too anisotropic and the distance at which the photons are observed is larger than one TMFP, the P_1 approximation is appropriate to describe the propagation of the photons in the tissue. In this case the radiance and the source can be written as:

$$L(\mathbf{r}, \hat{\Omega}, t) = \frac{1}{4\pi}\Phi(\mathbf{r}, t) + \frac{3}{4\pi}\mathbf{J}(\mathbf{r}, t) \cdot \hat{\Omega} \tag{2.6}$$

$$S(\mathbf{r}, \hat{\Omega}, t) = \frac{1}{4\pi}S_0(\mathbf{r}, t) + \frac{3}{4\pi}\mathbf{S_1}(\mathbf{r}, t) \cdot \hat{\Omega}. \tag{2.7}$$

After some calculations that have been explained in detail before [27], the P_1 equation for the photon fluence, $\Phi(\mathbf{r}, t)$, is given by:

$$\begin{aligned} &- D\nabla^2\Phi(\mathbf{r}, t) + v\mu_a\Phi(\mathbf{r}, t) + \frac{\partial\Phi(\mathbf{r}, t)}{\partial t} \\ &+ \frac{3D}{v}\left[\mu_a\frac{\partial\Phi(\mathbf{r}, t)}{\partial t} + \frac{1}{v}\frac{\partial^2\Phi(\mathbf{r}, t)}{\partial t^2}\right] \\ &= vS_0(\mathbf{r}, t) + \frac{3D}{v}\frac{\partial S_0}{\partial t} - 3D\nabla \cdot \mathbf{S_1}(\mathbf{r}, t), \end{aligned} \tag{2.8}$$

where $D = v/3(\mu_s' + \mu_a)$ is the photon diffusion coefficient [28, 29], which for a highly scattering medium, in the conditions stated before, could be approximated by $D = v/3(\mu_s')$, dropping the absorption term [30]. Equation 2.8 can be simplified further by making the following assumptions. If an isotropic source is assumed, which is the approximated distribution of a source located at $1/\mu_s'$ inside the medium, i. e., when the propagation direction has been randomized, the dipole term $\mathbf{S_1}(\mathbf{r}, t)$ can be neglected. The second

and third term on the right side of Equation 2.8 can also be neglected based on the following reasoning made in the frequency-domain where the photon fluence has the form $\Phi(\mathbf{r})\exp(-i\omega t)$, when the intensity of the source is sinusoidally modulated. In this form the time derivatives take the value $-i\omega$, and if we assume $3D\omega/v^2 \ll 1$ the terms can be neglected. The physical meaning of this approximation makes more sense if it is seen as $v\mu_s'/\omega \gg 1$, which says the scattering frequency must be much larger than the modulation frequency.

After all this assumptions, Equation 2.8 takes the form:

$$-D\nabla^2\Phi(\mathbf{r},t) + v\mu_a\Phi(\mathbf{r},t) + \frac{\partial\Phi(\mathbf{r},t)}{\partial t} = vS_0(\mathbf{r},t), \tag{2.9}$$

which is the *photon diffusion equation* (DE) for the photon fluence, $\Phi(\mathbf{r},t)$.

2.2 OPTICAL INTRINSIC SIGNAL IMAGING

As described before in Section 2.1, it is possible to extract information from a turbid medium, such as tissue, using light. In particular, based on the selective absorption properties of the tissue, we can use low-coherent light with a narrow spectral band to obtain information about the concentration of the chromophores present in it. This is the principle of the Optical Intrinsic Signal Imaging technique (OIS), which gives information that allows tracking the changes in the chromophores concentration over time.

The *Beer-Lambert law* as expressed in Equation 2.2, is given in terms of changes in intensity, over a distance, d, and the total attenuation coefficient, μ_t. For a non-scattering, absorbing medium, $\mu_t = \mu_a$. This equation can be expressed in terms of absorption as $A = \varepsilon Cl$, where $A = \log_{10}(I_0/I)$, by rewriting the attenuation coefficient as a product of the absorptivity of the attenuator, ϵ, and the concentration, C, of attenuating species in the material, $\mu_a = \epsilon C$. Apart from that, the thickness d, can be generalized, even in a reflection geometry, to be the distance that light travels through the medium, l.

Nevertheless, as mentioned before, this equation only accounts for the attenuation of light as it travels through a non-scattering medium. Since this is not the case in tissues, where multiple scattering events occur, the Beer-Lambert law has to be modified to include the wavelength dependence of the optical tissue properties [31] and is known as the *modified Beer-Lambert equation*:

$$\Delta A(\lambda) = \sum_{k=1}^{chromoph.} \varepsilon_k(\lambda)\Delta C_k D_a(\lambda) \tag{2.10}$$

where $\Delta A(\lambda)$ is the measured change in absorption at a given wavelength, λ, being I_0 the reference reflected intensity, at $t = 0$, and I the reflected intensity at a given time. Also, $\varepsilon_k(\lambda)$ and ΔC_k are the molar extinction coefficient at a given λ and the change in concentration of the k^{th} chromophore. Finally, $D_a(\lambda)$ is the differential pathlength, DP, defined as $D_a(\lambda) = \partial A(\lambda)/\partial \mu_a(\lambda)$ [32]. This DP depends on the tissue optical properties (μ_a and μ_s'), thus it depends on the wavelength and depends on the geometry of the medium. In other words, this term scales with the mean optical pathlength travelled by the photons in the tissue. The DP is not known *a priori* and it is usually determined using the forward propagation model or Monte Carlo simulations [31].

Having into account our application of measuring changes in blood oxygenation, we consider two chromophores present in the blood: the oxygenated hemoglobin, HbO, and the deoxygenated hemoglobin, Hb. With these chromophores, Equation 2.10 for a given wavelength λ takes the form:

$$\Delta A(\lambda) = [\varepsilon_{Hb}(\lambda)\Delta Hb + \varepsilon_{HbO}(\lambda)\Delta HbO]\, DP(\lambda). \tag{2.11}$$

In order to obtain information of the changes in these two chromophores it is necessary to measure the intensity in at least two different wavelengths. This makes possible to solve the problem of two unknowns with a system of at least two linear equations. Having more measured wavelengths will make the retrieved information about the change in the chromophores more precise. Which wavelengths to use depend a lot on the chromophores that are under study, and are chosen conveniently to extract more information with the smaller number of measurements.

In the case of measurements done in three different wavelenghts, the system of equations could be represented in matrix form as follows:

$$\begin{bmatrix} \Delta A(\lambda_1) \\ \Delta A(\lambda_2) \\ \Delta A(\lambda_3) \end{bmatrix} = \begin{bmatrix} \varepsilon_{Hb}(\lambda_1)DP(\lambda_1) & \varepsilon_{HbO}(\lambda_1)DP(\lambda_1) \\ \varepsilon_{Hb}(\lambda_2)DP(\lambda_2) & \varepsilon_{HbO}(\lambda_2)DP(\lambda_2) \\ \varepsilon_{Hb}(\lambda_3)DP(\lambda_3) & \varepsilon_{HbO}(\lambda_3)DP(\lambda_3) \end{bmatrix} \begin{bmatrix} \Delta Hb \\ \Delta HbO \end{bmatrix} \tag{2.12}$$

2.3 LASER SPECKLES

Every time that an optical method uses coherent light to extract information from biological tissues, it will have speckles[33, 34, 35, 36]. Hence, it is important to define what is the actual optical information that needs to be retrieved. If the aim of the method is to obtain images, the speckles will introduce some noise that will decrease the resolution of the images and that needs to be eliminated [35, 37]. On the other hand, the speckle patterns will contain relevant information about the properties and the components of the medium, that in the biological tissues will correspond to the structure or motion of the tissue components. One relevant example of the information that could be attained using speckle measurements will be the non-invasive measurement of blood flow.

2.3.1 *What is a speckle?*

A couple of years after the invention of the laser in the 1960's, a set of bright and dark spots that appeared when illuminating objects with slightly rough surface with laser light caught the attention of the researchers in the field [38, 39, 40]. At the beginning this effect was termed granularity but after some years the term *speckle* was widely adopted. Rapidly people started trying to explain the origin of the phenomenon attributed to the coherent nature of the laser radiation and the characteristics of the surface that was illuminated [41].

This phenomenon has been considered problematic for some applications because it reduces the resolution of the images obtained

with coherent radiation. Trying to overcome these situation, there have been many studies focused on removing the speckles from images obtained under laser illumination [42, 43, 44, 45]. Nevertheless, several applications based on the analysis of speckles patterns were found, some of which have evolved in the current biomedical applications to measure blood flow[46].

When coherent radiation interacts with a rough surface, when in comparison to its wavelength, which is the case of a wall, the light scattered by inhomogeneities of the surface will create a random interference pattern known as *speckle pattern* (Figure 2.4). The same will happen when laser light travels through a diffuse medium composed of randomly distributed particles, like the biological tissues, since the particles will create random differences in the optical pathlengths that will create the interference patterns. As in any interference pattern, the bright spots correspond to positions in space in which the scattered waves from the surface or by some particles inside the medium arrive in phase. On the other hand, the dark spots correspond to positions where destructive interference takes place because the scattered waves arrive out of phase. This is illustrated in Figure 2.5 where point A represents a dark speckle and B represents a bright speckle.

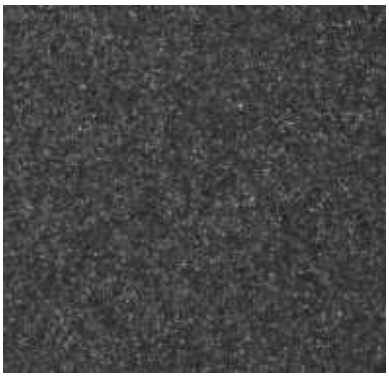

Figure 2.4: Typical speckle pattern from a surface under coherent illumination.

According to the geometry involved in the formation of the speckles, they can be divided in two groups. When the laser illuminates a sample and the speckle pattern resulting from the

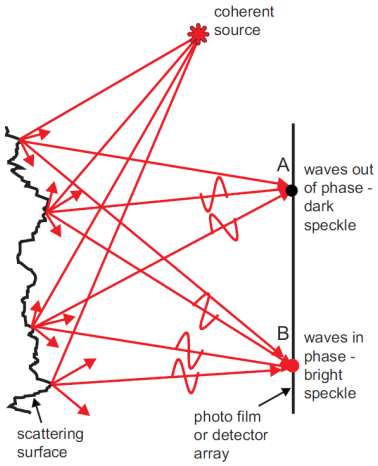

Figure 2.5: Objective speckles formation. © 2007, Society for Experimental Mechanics. Reproduced by permission from Gary Cloud [47]

back-scattered radiation is directly imaged using a screen or a sensor array, in the absence of a lens system (Figure 2.5), the speckles are known as **objective speckles**. In contrast, when the laser illuminated sample is imaged with a sensor through a lens system (Figure 2.5), the resulting speckles are known as **subjective speckles**. Here, according to the image formation principles, the lens provides that the waves that are being scattered at each point in the surface, are going to interfere at a corresponding point in the image, forming the speckle pattern in the sensor. Again, the resulting intensity at each point in the image depends on the phase of the waves arriving to it (Figure 2.5).

Due to the fact that the speckle measurements involved in this work are done using objective lenses, hereinafter, only **subjective speckles** will be considered. The study of this type of speckles includes interference as well as diffraction effects.

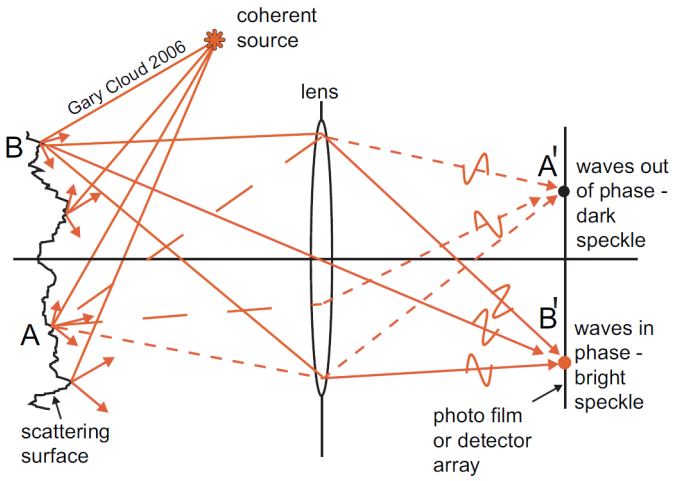

Figure 2.6: Subjective speckles formation. © 2007, Society for Experimental Mechanics. Reproduced by permission from Gary Cloud [48]

2.3.2 *Statistical properties of speckles*

The speckle patterns exhibit a spatial random intensity due to the random phases of the scattered waves interfering to form it. Hence, the proper approach to explain the speckle phenomena contemplates the use of statistics [44, 49]. A first-order statistics analysis describes the contrast of the speckle, while the size distribution of the speckles is described by a second-order statistics.

The first-order statistics refers to the statistical properties of a single point in space, and it is capable of describing the fluctuations of brightness in the speckle pattern. A complete explanation of a speckle pattern has to be done in terms of the electric field and the statistics of its real and complex parts. To do so, I will closely follow the approach by Goodman [50, 51]. Under the assumptions that the incident electric field at a point (x, y, z) and at time t, is perfectly polarized and perfectly monochromatic, it can be represented as $u(x, y, z; t) = A(x, y, z)\exp(i2\pi\nu t)$ being ν the optical frequency and $A(x, y, z)$ a complex phasor amplitude of the form $A(x, y, z) = |A(x, y, z)|\exp[i\theta(x, y, z)]$.

Also at the point (x, y, z) of the speckle pattern and at time t, the intensity is given by:

$$I(x, y, z) = \lim_{T \to \infty} \frac{1}{T} \int_{-T/2}^{T/2} |u(x, y, z)|^2 dt = |A(x, y, z)|^2$$

The complex amplitude can be considered as resulting from the superposition of the electric fields from the many elementary scattering areas conforming the scattering surface or the scattering particles inside a turbid medium, being represented as: $A(x, y, z) = \sum_{k=1}^{N} |a_k| \exp(i\phi_k)$, being $|a_k|$ and ϕ_k the amplitude and the phase from the kth scattering area, and N the total number of contributing elements.

This analysis is done in a manner that is comparable to the statistical description of the Brownian-motion, as a random-walk model, and as such, two assumptions have to be taken into account:

- The amplitude a_k and the phase ϕ_k of the kth elementary contribution are statistically independent of each other and are also not related to those of another contribution.
- The phases ϕ_k of the contributing elements are equally probable to have its value anywhere within the interval $(-\pi, \pi)$, given the roughness of the surface when compared to a wavelength.

The complex amplitude of the field at a given point of the speckle pattern can be separated in its real and imaginary parts as:

$$\begin{aligned} A^{(r)} &= \sum_{k=1}^{N} |a_k| \cos\theta, \\ A^{(i)} &= \sum_{k=1}^{N} |a_k| \sin\theta, \end{aligned} \tag{2.13}$$

from where it is possible to demonstrate that $A^{(r)}$ and $A^{(i)}$ have zero mean, identical variances and are uncorrelated [51]. Furthermore, if the number of elementary phasor contributions N, i. e.,

the number of surface scattering elements or scattering particles, is assumed to be very large, according to the *central limit theorem*, as $N \longrightarrow \infty$ the distribution of $A^{(r)}$ and $A^{(i)}$ are Gaussian.

With this consideration into account, the joint probability density function of the real and imaginary parts of the field takes the form:

$$p_{r,i}(A^{(r)}, A^{(i)}) = \frac{1}{2\pi\sigma^2} \exp\left\{-\frac{[A^{(r)}]^2 + [A^{(i)}]^2}{2\sigma^2}\right\} \tag{2.14}$$

where

$$\sigma^2 = \lim_{N\to\infty} \frac{1}{N} \sum_{k=1}^{N} \frac{\langle |a_k| \rangle^2}{2}.$$

and the $\langle\rangle$ denotes the ensemble average.
Given that the measurable properties of the electric field are the intensity and the phase, it is very useful to know its statistical properties, which share the same characteristics of the electric field. To do that a transformation of random variables is needed and will take into account that the intensity and the phase are related to the real and imaginary parts of the complex amplitude as $A^{(r)} = \sqrt{I}\cos\theta$ and $A^{(i)} = \sqrt{I}\sin\theta$.

The joint probability distribution for the intensity and the phase is defined as $p_{I,\theta} = p_{r,i}\left(\sqrt{I}\cos\theta, \sqrt{I}\sin\theta\right) \|J\|$, where

$$\|J\| = \left\| \begin{matrix} \frac{\partial A(r)}{\partial I} & \frac{\partial A(r)}{\partial \theta} \\ \frac{\partial A(i)}{\partial I} & \frac{\partial A(i)}{\partial \theta} \end{matrix} \right\| = \frac{1}{2}$$

corresponds to the Jacobian for the transformation (modulus of the determinant). After applying this transformation the joint probability distribution for I and θ is given by:

$$p_{I,\theta}(I,\theta) = \begin{cases} \frac{1}{4\pi\sigma^2} \exp\left(-\frac{I}{2\sigma^2}\right) & I \geqslant 0 \\ & -\pi \leqslant \theta \leqslant \pi \\ 0 & \text{otherwhise} \end{cases} \tag{2.15}$$

The probability density function for the intensity is the integral of the joint probability distribution over all the possible angles and is given by:

$$p_I(I) = \int_{-\pi}^{\pi} p_{I,\theta}(I,\theta)d\theta = \begin{cases} \frac{1}{2\pi\sigma^2}\exp\left(-\frac{I}{2\sigma^2}\right) & I \geqslant 0 \\ 0 & \text{otherwhise} \end{cases} \tag{2.16}$$

For the phase it would be the integral over all the possible intensities giving:

$$p_\theta(\theta) = \int_{-\pi}^{\pi} p_{I,\theta}(I,\theta)dI = \begin{cases} \frac{1}{2\pi} & -\pi \leqslant \theta \leqslant \pi \\ 0 & \text{otherwhise} \end{cases} \tag{2.17}$$

These results show that the probability of finding an intensity value at a given point in space in a polarized speckle pattern is given by a negative exponential distribution that is angle independent, and that the angles are described by a uniform statistics. Hence, the distributions for the phase and the intensity are statistically independent and the joint probability distribution can be written as $p_{I,\theta}(I,\theta) = p_I(I)p_\theta(\theta)$.

Other properties of the intensity in a polarized speckle pattern would be described by the moments. According to the exponential distribution of the intensities, the n^{th} moment $< I^n >$ would be given by:

$$\langle I^n \rangle = n!\frac{2}{\sigma^2}^n \tag{2.18}$$

In a distribution are of especial importance the mean and the variance. The first moment corresponds to the mean and the variance depends on the second moment. The first and second moments are given by:

$$\langle I \rangle = \frac{2}{\sigma^2} \tag{2.19}$$

$$\langle I^2 \rangle = 2\langle I \rangle \tag{2.20}$$

$$\tag{2.21}$$

The variance is defined as $\langle I^2 \rangle - \langle I \rangle^2$, giving:

$$\sigma_I^2 = 2 \langle I \rangle^2 - \langle I \rangle = \langle I \rangle \tag{2.22}$$

This means that the standard deviation, σ_I of a polarized speckle pattern is equal to its mean. The contrast of a speckle pattern is defined as:

$$\kappa = \frac{\sigma_I}{\langle I \rangle}, \tag{2.23}$$

Hence, for a polarized speckle pattern, or a fully developed speckle pattern, its contrast is equal to 1. If the speckle contrast is 1, in principle it is not possible to extract information from this statistical quantity. Nevertheless, the processes occurring inside a medium will change the probability distribution, changing the values of the speckle contrast, which as will be explained later is the basis of some optical imaging techniques.

2.3.3 *Speckle temporal autocorrelation*

As mentioned before, when a coherent light passes through a medium composed of identical scattering particles, the light scattered by each particle will interfere forming a speckle pattern. This pattern will fluctuate over time depending on the presence of moving particles. If the scattered light intensity is measured over time and in one point of the space, it is possible to extract information about the dynamics of the particles inside the medium. Hence it is important to understand light scattering and how it depends on the motion of the particles inside the medium. This is done by accounting how a signal at a time t is related to a signal measured at a time $t + \tau$ and it is represented by the *temporal autocorrelation function* of the intensity:

$$G_2(\tau) = \langle I(t) I(t + \tau) \rangle \tag{2.24}$$

The intensity is the quantity that is readily available from the measurements with detectors, but the complete description of the speckle pattern fluctuations, due to the random changes in the

phase, is contained in the electric field. Hence, it is better to calculate the temporal field autocorrelation function:

$$G_1(\tau) = \langle E(t)E^*(t+\tau)\rangle, \tag{2.25}$$

Nevertheless, it is useful to represent the temporal field autocorrelation in terms of the intensity at the detector, i. e., $I = E(t)E^*(t)$. In general, during an experiment, due to the fluctuations of the light intensity, we take the averaged fluctuations of the intensity at the detector $\langle I\rangle = \langle E(t)E^*(t)\rangle$. According to this, Equation 2.24 could be rewritten as:

$$G_2(\tau) = \langle E(t)E^*(t)E(t+\tau)E^*(t+\tau)\rangle \tag{2.26}$$

If the scattered electric field is a Gaussian variable with zero mean, Equation 2.26 is simplified to the sum over all the possible products of its second moments as [52]:

$$\begin{aligned} G_2(\tau) &= \langle E(t)E^*(t)\rangle\langle E(t+\tau)E^*(t+\tau)\rangle \\ &\quad + \langle E(t)E(t+\tau)\rangle\langle E^*(t)E^*(t+\tau)\rangle \\ &\quad + \langle E^*(t)E(t+\tau)\rangle\langle E(t)E^*(t+\tau)\rangle \\ &= \langle I\rangle^2 + |\langle E(t)E(t+\tau)\rangle|^2 + |\langle E(t)E^*(t+\tau)\rangle|^2 \end{aligned} \tag{2.27}$$

If the medium is considered to be ergodic, the ensemble average is equivalent to time averages. The time average $\langle E(t)E(t+\tau)\rangle$ and its conjugate can be neglected compared to the other two terms on the right hand side of Equation 2.27 [52], which results in the Siegert equation that relates the temporal field autocorrelation function to the temporal intensity autocorrelation function:

$$G_2(\tau) = \langle I\rangle^2 + |G_1(\tau)|^2 \tag{2.28}$$

where $\langle I\rangle$ is the ensemble average intensity. Experimentally, the detector is measuring more than one speckle, a correction factor, β that accounts for the number of speckles detected and the coherence of the laser is introduced in Equation 2.28, giving:

$$G_2(\tau) = \langle I\rangle^2 + \beta\,|G_1(\tau)|^2\,. \tag{2.29}$$

2.4 PHOTON PROPAGATION MODEL ACCOUNTING DYNAMICAL SCATTERERS

Previously in Section 2.3.3 it has been presented how the temporal autocorrelation functions of the intensity and the field will give information about the dynamic of the particles inside the medium. However, to calculate the field temporal autocorrelation, $G_1(\tau)$, the total scattered electric field at one point in space has to be known, and it will depend on the scattering process that occurs when light interacts with the particles in the medium. The first approach to study the scattering is to consider the light propagation in a dilute medium, with low concentration of scatterers, to ensure light has been scattered only once inside the medium before being transmitted or re-emitted. This is known as the *single scattering regime*. In the case of biological tissues, this single scattering regime does not hold and several scattering events must be considered. This is the *multiple scattering regime*. Since the scattered electric field depends on the positions of each scatterer over time and the number of times the photons are scattered inside the medium, the field autocorrelation functions are going to be calculated for each scattering regime. The relations derived in this section are presented following the approach presented in [27].

2.4.1 *Single-Scattering*

To study the scattering, it is generally considered a monochromatic beam (ω), propagating in a direction $\hat{k}_{in}$, that illuminates a sample with scattering particles, as seen in Figure 2.7. Due to the interaction with the particles, the light is scattered in all directions but if a sensor is positioned at an angle, θ from the propagation direction, the light detected will be the scattered in that particular direction, $\hat{k}_{sc}$.

The scattering vector $\vec{q}$, is defined by the difference between the incident and the scattered wavevectors: $\vec{q} = \vec{K}_{sc} - \vec{K}_{in}$, where $\vec{K}_{sc} = K_{sc}\hat{k}_{sc}$ and $\vec{K}_{in} = K_{in}\hat{k}_{in}$. For this model we are assuming elastic scattering, hence, the modulus of both vectors is the same, $k_0 = |\vec{K}_{in}| = |\vec{K}_{sc}|$, with value $k_0 = 2\pi n/\lambda$, where n is the refrac-

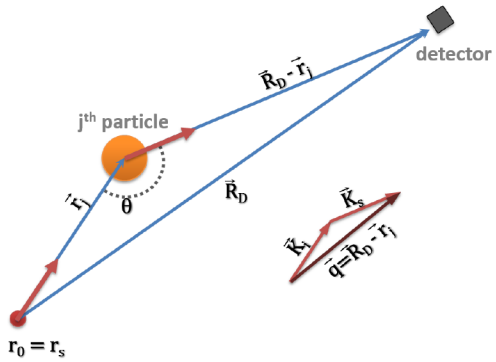

Figure 2.7: Single scattering schematic.

tive index of the medium and λ is the wavelength of the incident beam. Having this, the magnitude of the scattering vector is given by $q = 2k_0 \sin\theta/2$.

The electric field at the detector, located at position $\vec{R}_D$, is the superposition of all the scattered fields, or fields re-emitted by each particle in the medium, but to arrive to a definition of this electric field, it is easier to start with the description of the scattering by one single particle. The incident light that is illuminating one particle at a position $\vec{r}_j$, can be described by the electric field:

$$E^{(in)}(\vec{r}_j) = |E_0| \exp(i\vec{K}_{in} \cdot \vec{r}_j) \tag{2.30}$$

and, the scattered electric field at the detector could be considered a spherical wave with the form:

$$E^{(sc)}(\vec{R_D}) \propto \exp(i\vec{K}_{in} \cdot \vec{r}_j) \frac{\exp(ik_0|\vec{R}_D - \vec{r}_j|)}{|\vec{R}_D - \vec{r}_j|} \tag{2.31}$$

In the far field approximation $|\vec{R}_D| \gg |\vec{r}_j|$, that is when the detector is located very far from the scattering particle, $|\vec{R}_D - \vec{r}_j| \cong$

$|\vec{R}_D| - \vec{r}_j \cdot \vec{K}_{sc}/K_{sc} + ...$, the scattered field by one particle at the detector is:

$$\begin{aligned} E^{(sc)}(\vec{R_D}) &\propto \exp(i\vec{K}_{in} \cdot \vec{r}_j) \frac{\exp\left(i|\vec{K}_{in}|\left(|\vec{R}_D| - \vec{r}_j \cdot \frac{\vec{K}_{sc}}{|\vec{K}_{sc}|}\right)\right)}{|\vec{R}_D - \vec{r}_j|} \\ &= \exp(i\vec{K}_{in} \cdot \vec{r}_j) \frac{\exp\left(i|\vec{K}_{in}||\vec{R}_D|\right)}{|\vec{R}_D|} \exp\left(-i\frac{|\vec{K}_{in}|}{|\vec{K}_{sc}|}\vec{r}_j \cdot \vec{K}_{sc}\right) \\ &= \frac{\exp\left(i|\vec{K}_{in}||\vec{R}_D|\right)}{|\vec{R}_D|} \exp\left(i\left(\vec{K}_{in} - \vec{K}_{sc}\right) \cdot \vec{r}_j\right) \\ &= \frac{\exp\left(i|\vec{K}_{in}||\vec{R}_D|\right)}{|\vec{R}_D|} \exp\left(-i\vec{q} \cdot \vec{r}_j\right) \end{aligned} \tag{2.32}$$

where $\vec{r}_j$ is position of the j^{th} particle. In the single scattering regime it is assumed that the total scattered field from N particles is the superposition of the scattered field for each particle, hence, the total scattered field could be written as:

$$E^{(sc)}(\vec{R_D}) \propto \frac{\exp\left(i\vec{K}_{in} \cdot \vec{R}_D\right)}{|\vec{R}_D|} \sum_{j=1}^{N} \exp\left(-i\vec{q} \cdot \vec{r}_j\right) \tag{2.33}$$

where the total scattering spherical wave has been approximated to a planar wave, given the fact that the detector is very far from the scattering centers. It is important to note that the position of each particle will change over time, i. e., $\vec{r}_j(t)$ and these changes in the position are responsible for the changes in the phase of the electric field.

To study the fluctuations, the scattered field autocorrelation function (Equation 2.25) has to be calculated and for convenience it is preferable to work with the normalized field autocorrelation function:

$$g_1(\tau) = \frac{\langle E(t)E^*(t+\tau)\rangle}{\langle |E(t)|^2\rangle} \tag{2.34}$$

Then the total scattered field, Equation 2.33, is introduced in Equation 2.34 and considering that the particles are independent

from each other, the cross terms can be averaged to zero yielding to:

$$g_1(\tau) = \langle \exp(i\vec{q} \cdot \Delta\vec{r}(\tau)) \rangle = \exp(i\vec{q} \cdot \langle \Delta\vec{r}(\tau) \rangle) \tag{2.35}$$

where $\Delta\vec{r}(\tau) = \vec{r}(t+\tau) - \vec{r}(t)$ is the distance a particle has displaced in a time τ and to account for the displacement of all the particles, an average is done over $\Delta\vec{r}(\tau)$ weighing it by an appropriate probability distribution.

If it is considered that the scatterers are moving randomly, i. e., undergoing a Brownian motion, the probability that a particle has displaced a distance Δr in a time τ is Gaussian and is given by:

$$P(\Delta\vec{r}(\tau)) = \frac{1}{(\frac{2\pi}{3}\langle \Delta^2 r(\tau) \rangle)^{3/2}} \exp\left(-\frac{|\Delta\vec{r}(\tau)|^2}{\frac{2}{3}\langle \Delta^2 r(\tau) \rangle} \right). \tag{2.36}$$

By integrating the probability distribution over the 3 dimensions of space, in which the displacements of the particles could take place:

$$g_1(\tau) = \int_{-\infty}^{\infty} P(\Delta\vec{r}(\tau)) \exp(i\vec{q} \cdot \Delta\vec{r}(\tau)) d^3\vec{r}(\tau)$$

and after some calculations [53], it is found that the normalized field temporal autocorrelation function resulting from scatterers that are moving following a Brownian motion is given by:

$$g_1(\tau) = \exp\left(-\frac{1}{6} q^2 \langle \Delta^2 r(\tau) \rangle \right). \tag{2.37}$$

2.4.2 *Multiple Scattering*

When probing tissues deep, multiple scattering has to be considered. In this case, the fluctuations of the scattered intensity are given not only by the displacement of the particles, but also by the randomization of the propagation direction represented by the propagation vector $\vec{q}$, that is reached after light has experienced N scattering events. Hence, the field autocorrelation function should

include an ensemble average over all the possible propagation angles and particle displacements.

$$g_1^{(N)}(\tau) = \left\langle \exp\left(i \sum_{n=1}^{N} \vec{q}_n \cdot \Delta\vec{r}_n \right) \right\rangle_{q,\Delta r} \tag{2.38}$$

After assuming that the successive scattering events and the motion between neighbouring particles are independent, it takes the form:

$$g_1^{(N)}(\tau) = \langle \exp\left(i\vec{q}_n \cdot \Delta\vec{r}\right) \rangle_{q,\Delta r}^{N} \tag{2.39}$$

The ensemble average over the particle displacement uses the mean square displacement of the particles that has been calculated for the single scattering case obtaining:

$$g_1^{(N)}(\tau) = \left\langle \exp\left(-\frac{1}{6} q^2 \left\langle \Delta r^2(\tau) \right\rangle \right) \right\rangle_{q}^{N} \tag{2.40}$$

If it is assumed that $\frac{1}{6} q^2 \left\langle \Delta r^2(\tau) \right\rangle \ll 1$ the ensemble average of q can be put inside the exponential. Apart from that, the N scattering events could be approximated by the pathlength travelled by the photons within the medium divided by the scattering length, s/l, having:

$$g_1^{(N)}(\tau) = \exp\left(-\frac{1}{6} \left\langle q^2 \right\rangle \left\langle \Delta r^2(\tau) \right\rangle s/l \right) \tag{2.41}$$

The ensemble average over all the phase changes or momentum transfer is given by:

$$\left\langle q^2 \right\rangle = \int_0^{\pi} f(\cos\theta) q^2 d(\cos\theta) \tag{2.42}$$

where $f(\cos\theta)$ is the form factor of the particles and $q^2 = 4k_0^2 \sin^2(\theta/2)$ is the magnitude squared of the propagation vector. The ensemble average is over the angles, hence we have:

$$\left\langle q^2 \right\rangle = 4k_0^2 \left\langle \sin^2 \frac{\theta}{2} \right\rangle = 2k_0^2 \left[1 - \langle \cos\theta \rangle \right] \tag{2.43}$$

where $1 - \langle \cos\theta \rangle = l/l*$ is the step length in a random walk and $l* = 1/\mu_s'$. Finally we obtain:

$$\langle q^2 \rangle = 2k_0^2 \frac{l}{l^*} \tag{2.44}$$

and by replacing this expression in Equation 2.41, the field autocorrelation function for light that has travelled a pathlength, s, inside a biological tissue, is represented by:

$$g_1^{(N)}(\tau) = \exp\left(-\frac{1}{3}k_0^2 \langle \Delta r^2(\tau) \rangle \frac{s}{l*}\right) \tag{2.45}$$

For the case of illumination with a continuous wave (CW) laser, it is the full distribution of pathlengths that contributes to the decay of the correlation function, and to account for this, the previous equation has to be integrated over all the possible pathlengths by considering a probability distribution of pathlengths, $P(s)$.

$$g_1(\tau) = \int_0^\infty P(s) \exp\left(-\frac{1}{3}k_0^2 \langle \Delta r^2(\tau) \rangle \frac{s}{l*}\right) ds \tag{2.46}$$

This probability distribution will depend on the geometry of the medium under study and if we consider a point source and a point detector located at a distance r_{s-d} from the source, and probing an infinite medium it will take the form:

$$P(s) = \left(\frac{c}{4\pi s D}\right)^{3/2} \exp\left(-\frac{c r_{sd}^2}{4sD}\right) \exp(-\mu_a s) \tag{2.47}$$

After the integration the result of the field autocorrelation function will be given by:

$$g_1(\tau) = \exp\left(-\sqrt{k_0^2 \langle \Delta r^2(\tau) \rangle + 3\mu_a l*} \frac{r_{sd}}{l*}\right) \tag{2.48}$$

2.4.2.1 *Correlation diffusion equation*

As explained before, the propagation of light in multiple scattering media with static scatterers characterized by the optical absorption (μ_a) and scattering (μ_s) coefficients obeys the radiative transport equation (RTE)[10]. Under a set of well-defined and validated assumptions (Section 2.1.2), a diffusion equation model [10]

for photon propagation, which is a simplified form of RTE, can be obtained. Similarly, in order to study the photon propagation under dynamic scatterers, a correlation transport equation (CTE) [54, 55] is adopted, which is analogous to the RTE for static scatterers:

$$\begin{aligned}\nabla \cdot G_1^T(\vec{r},\hat{\Omega},\tau) + \mu_t G_1^T(\vec{r},\hat{\Omega},\tau) \\ = \mu_s \int G_1^T(\vec{r},\hat{\Omega}',\tau) g_1^s(\hat{\Omega},\hat{\Omega}',\tau) f(\hat{\Omega},\hat{\Omega}',\tau) d\hat{\Omega}' \\ + S(\vec{r},\hat{\Omega}) \end{aligned} \tag{2.49}$$

From the CTE, again using the diffusion approximation, the correlation diffusion equation (CDE) [27, 56, 57] is derived. This equation describes the propagation of the electric field autocorrelation $G_1(\mathbf{r},\tau) = \langle E^*(\mathbf{r},t)E(\mathbf{r},t+\tau)\rangle$ in the tissue, as given in Equation 2.50:

$$\begin{aligned}-\nabla \cdot D(\mathbf{r})\nabla G_1(\mathbf{r},\tau) + v\left(\mu_a(\mathbf{r}) + \frac{1}{3}\mu_s' k_0^2 < \Delta r^2(\tau) >\right) G_1(\mathbf{r},\tau) \\ = v S_0(\mathbf{r}-\mathbf{r}_0), \end{aligned} \tag{2.50}$$

where the reduced scattering coefficient $\mu_s' = (1-g)\mu_s$, g is the anisotropy factor of scattering, $D = \frac{v}{3(\mu_a+\mu_s')}$ is the optical diffusion coefficient, and $S_0(\mathbf{r}-\mathbf{r}_0)$ is the isotropic point source located at $\mathbf{r} = \mathbf{r}_0$. $k_0 = \frac{2\pi n_0}{\lambda}$ is the modulus of propagation vector of light where n_0 is the refractive index of the medium and λ is the wavelength of light. Here $\mathbf{r} = (x,y,z)$ is the spatial coordinate in three dimensional space and τ is the correlation time.

As presented in Section 2.4.1, the dynamics of the scattering medium is modeled by $< \Delta r^2(\tau) >$ which is the mean square displacement (MSD) of the scatterers [10]. When the motion of scatterers is modeled as Brownian motion then $< \Delta r^2(\tau) >= 6D_B\tau$, where D_B is the particle diffusion coefficient. Under a random flow motion assumption the MSD of the scatterers is given by $\langle \Delta r^2(\tau)\rangle = \langle V^2\rangle\tau^2$ where $\langle V^2\rangle$ is the square of the effective (average) velocity of the scattering particles. If both flows are considered, the MSD is given by $\langle \Delta r^2(\tau)\rangle = 6D_B\tau + \langle V^2\rangle\tau^2$. Other more general formulations are also possible to account for different types of motion and effects [10, 58].

2.4.2.2 *Green's solutions to CDE*

The electric field auto-correlation function, $G_1(\mathbf{r},\tau)$, varies depending on the geometry of the diffusive medium. For the purpose of this work, we have used the analytical solutions [56, 57] for the homogeneous parallel plane slab [59] and the semi-infinite medium [60] corresponding to the transmission and re-emission geometries respectively. These solutions consider a parallel plane tissue slab of thickness s, an isotropic light source at depth $z_0 = 1/\mu_s'$ inside the tissue and z as the light propagation direction. For this geometry and under the extrapolated boundary condition [60], the Green's function, G_1, at a distance $\mathbf{r}$ from the source is given by [10]:

$$\begin{aligned} &G_1([\mathbf{r},z],[\mathbf{r}_0=0,z_0=1/\mu_s'],\tau) \\ &= \frac{v}{4\pi D}\sum_{m=-\infty}^{\infty}\left(\frac{exp[-Kr_{+,m}]}{r_{+,m}} - \frac{exp[-Kr_{-,m}]}{r_{-,m}}\right), \end{aligned} \tag{2.51}$$

where

$$r_{\pm,m} = (\mathbf{r}^2 + (z - z_{\pm,m})^2)^{1/2}$$

and

$$K = \left((\mu_a + \alpha\mu_s' k_0^2 \frac{\langle \Delta r^2(\tau)\rangle}{3})\frac{v}{D}\right)^{1/2}.$$

The extrapolated boundary is at a distance $z_e = 2AD$ from the physical, parallel plate boundaries where D is the optical diffusion coefficient as defined before and $A = (1 + R_{eff})/(1 - R_{eff})$. $R_{eff} \approx -1.440n^{-2} + 0.710n^{-1} + 0.668 + 0.00636n$ is the effective reflection coefficient to account for the index mismatch between tissue and air where n is refractive index ratio between diffusing medium and the external medium, i. e., $n = n_{diff}/n_{ext}$. An infinite number of dipoles represent pairs of positive and negative sources placed at $z_{+,m} = 2m(s + 2z_e) + z_0$ for the positive sources and at $z_{-,m} = 2m(s + 2z_e) - 2z_e - z_0$ for the negatives with $m = (0, \pm1, \pm2...)$. The semi-infinite medium solution is a special case of the slab solution when only the $m = 0$ terms are considered, i. e., with only one planar boundary.

2.5 SPECKLE-BASED IMAGING METHODS

2.5.1 *Diffuse correlation spectroscopy*

In DCS, the measurement available is the intensity autocorrelation. $g_2(\mathbf{r},\tau) =< I(t)I(t+\tau) >$, instead of the field autocorrelation which is related to normalized field autocorrelation $g_1(\mathbf{r},\tau) = \frac{G_1(\mathbf{r},\tau)}{G_1(\mathbf{r},0)}$ through the Siegert relation [61]: $g_2(\tau) = 1 + \beta|g_1(\tau)|^2$. Here β is a constant, typically less than one, whose value depends on the detection optics as well as the different optical modes in the measurement. Together with the CDE in Equation 2.50 and the Siegert relation, DCS quantitatively measures the MSD.

We note that the reported quantity in DCS is an effective diffusion coefficient (D_B) obtained from fitting to correlation data and it is not the traditional thermal Brownian diffusion coefficient of red blood cells. It is, however, well validated that this model represents the absolute and relative blood flow in tissues [10, 62, 63].

2.5.2 *Laser speckle flowmetry*

In the photon correlation methods, the procedure to extract the dynamics of the particles inside the medium is to measure the intensity fluctuations of the scattered light at a single speckle and analizing them using the temporal autocorrelation function, $g_2(\tau)$. Conversely, in speckle contrast based methods, the measurement consists on imaging a fluctuating speckle pattern with a camera and integrating the speckle patterns over the exposure time of it. The analysis comprises the calculation of the speckle contrast, κ, which quantifies the blurring of the speckle pattern and is used for flow measurement. In laser speckle flowmetry (LSF), single scattering approximations and uniform illumination of the sample of interest is utilized relating κ to blood flow at superficial layers.

SPECKLE CONTRAST AND ITS RELATION TO FLOW As presented in Section 2.3.2, the intensity distribution of a speckle pattern can only be described statistically and it was shown that for a static speckle pattern with a spatial gaussian distribution of intensity, the standard deviation is equal to the mean and the ratio

of the standard deviation (σ_I) of measured intensity to its mean value ($\langle I \rangle$) in the spatial domain (Equation 2.23) was equal to 1. Therefore, if the speckle distribution is not gaussian, this ratio is reduced and will be a measure of the contrast of the speckle pattern called the *speckle contrast*.

In the case of moving scatterers inside the medium, the produced speckle pattern fluctuates over time, and, by integrating these patterns over the exposure time of the camera, T, the fluctuations will be averaged out, giving as a result a blurred image and the speckle contrast will be defined as

$$\kappa(\mathbf{r}, T) = \frac{\sigma_I(\mathbf{r}, T)}{\mu_I(\mathbf{r}, T)} \tag{2.52}$$

where T is the exposure time of the detection system, and the statistics calculations are done in the spatial domain, i.e. [64]. In this equation we have changed the notation from $\langle I \rangle$ to μ_I for simplicity, but the meaning of ensemble average is kept. The speckle contrast varies between zero and one, where high values indicate slower motion of the scatterers and low values represent higher velocities.

The speckle contrast measured over the space in a time integrated image could be related to the photon correlation methods and will be shown onwards. When imaging a speckle pattern with a camera, the integrated intensity measured at a given pixel during the exposure time is given by [65]:

$$S = \int_0^T I(t')dt' \tag{2.53}$$

where $I(t')$ is the instantaneous intensity at a given pixel. In order to arrive to the speckle contrast, the mean and the standard deviation should be calculated.

The mean of the integrated intensity is calculated by:

$$< S >= \left\langle \int_0^T I(t')dt' \right\rangle = \int_0^T \left\langle I(t') \right\rangle dt' =< I > T \tag{2.54}$$

Recalling that the standard deviation is the square root of the variance, and the variance is defined as $\sigma^2 =< S^2 > - < S >^2$, the second moment of the integrated intensity has to be calculated:

$$< S^2 >= \left\langle \int_0^T \int_0^T I(t')I(t'')dt'dt'' \right\rangle = \int_0^T \int_0^T \langle I(t')I(t'')\rangle \, dt'dt'' \tag{2.55}$$

where $\langle I(t')I(t'')\rangle$ could be recognized as the intensity correlation function, that is known to be related to the field autocorrelation function by the Siegert's relation and we can get $\langle I(t')I(t'')\rangle =< I >^2 \left\{1 + \beta \left|g_1(t' - t'')\right|^2\right\}$. Replacing this in Equation 2.55, we obtain:

$$\begin{aligned} < S^2 > &=< I >^2 \int_0^T \int_0^T \left\{1 + \beta \left|g_1(t' - t'')\right|^2\right\} dt'dt'' \\ &=< I >^2 T^2 + < I >^2 \int_0^T \int_0^T \beta \left|g_1(t' - t'')\right|^2 dt'dt'' \end{aligned} \tag{2.56}$$

Hence the variance is:

$$\begin{aligned} < S^2 > - < S >^2 = & < I >^2 T^2 \\ & + < I >^2 \int_0^T \int_0^T \beta \left|g_1(t' - t'')\right|^2 dt'dt'' \\ & - < I >^2 T^2 \end{aligned} \tag{2.57}$$

and the speckle contrast would be defined as:

$$\kappa = \sqrt{\frac{\beta}{T^2} \int_0^T \int_0^T |g_1(t' - t'')|^2 \, dt'dt''} \tag{2.58}$$

After some coordinates transformations, the double integral can be converted into a single integral and, given the normalized field autocorrelation function is even, Equation 2.58 can be reduced to:

$$\kappa^2(\mathbf{r}, T) = \frac{2\beta}{T} \int_0^T |g_1(\mathbf{r}, \tau)|^2 \left(1 - \frac{\tau}{T}\right) d\tau \tag{2.59}$$

which represents the relation between the speckle contrast and the normalized field autocorrelation, $g_1(\mathbf{r}, \tau)$ [66, 67], as defined previously in section (number), at time t and position $\mathbf{r}$. The brackets $\langle\ \rangle$

in the previous calculations denote ensemble averages for theoretical calculations, whereas for experimental measurements denote time averages, assuming the process is ergodic and stationary. β is an instrumental constant accounting for the optical system that is related to the number of pixels per speckle, and also to the polarization nature of the incident light [52, 66]. τ is the correlation time and T is the exposure time of the detection system.

The function describing the speckle contrast in Equation 2.59 depends strongly on the form of the normalized field autocorrelation function, which is related to the optical spectrum through a Fourier transform. When a laser light interacts with scatterers in motion, each scattered photon will experiment a frequency shift and if the scatterers are moving with a given velocity distribution, the resulting optical spectrum at the detector will vary its shape according to the velocity distribution. In general, in LSF, it is assumed that the velocity distribution of the scatterers is Lorentzian. Hence, the normalized field autocorrelation function, is a negative exponential function [68], which has the same form as the normalized field autocorrelation obtained when deriving the scattered field in the single scattering regime for particles moving randomly (Equation 2.37):

$$g_1(\mathbf{r},\tau) = \exp(-\tau/\tau_c) \tag{2.60}$$

where τ is the delay time and τ_c is the decorrelation time of the intensity fluctuations [69], that would be inversely proportional to the mean velocity of the scatterers. Replacing Equation 2.60 in Equation 2.59 the speckle contrast would be given by:

$$\kappa^2(\mathbf{r},T) = \beta \left\{ \frac{\exp\left(-2T/\tau_c\right) - 1 + 2T/\tau_c}{2\left(T/\tau_c\right)^2} \right\} \tag{2.61}$$

2.6 TOMOGRAPHICAL IMAGING WITH DIFFUSE OPTICS

In the diffuse optics techniques described before, it is assumed that the tissue is homogeneous in its optical and dynamic properties and that it has a simple geometry, but in reality this might not be true. There are medical conditions, e. g., a breast cancerous tumour, in which the optical properties of the affected region

of the tissue will differ from the optical properties of the healthy tissue. In such case, it would be desirable to obtain three dimensional images to find the location of the tumour, which will be considered an inhomogeneity inside the tissue. The idea behind this consist on measuring at the surface the light scattered by the tissue and from those measurements reconstruct the optical/physiological properties for every point inside the tissue, i. e., its spatial distribution. One non-invasive technique, based on the diffusion model, that is capable of reconstructing an image of such tumour is the diffuse optical tomography (DOT). On the other hand, if the heterogeneity is due to changes in the dynamic properties of the tissue, e. g., changes in blood flow due to an ischemic stroke, the image reconstruction could be done using the temporal correlation functions measured at the surface by using the diffuse correlation tomography (DCT). The interest of this work is the reconstruction of blood flow in tissues, hence, the principles for DCT will be presented, although the approaches are general for 3D imaging with diffuse light.

As discussed above, we present an algorithm/method to recover the dynamic property, specifically, the mean-square displacement (MSD), $\langle \Delta r^2(\tau) \rangle$, from the scattering intensity measurements made at the surface of the object to be probed. The imaging algorithm is often called inverse model (or inverse problem)[70, 71] which constitutes a forward model, representing the propagation of field autocorrelation in the media which is the CDE (2.50), and a sensitivity relation connecting the sensitivity of the measurements to any perturbations in the MSD [72, 73]. The forward model can be represented as a function $F(< \Delta r^2(\tau) >) = G_1(\mathbf{m}, \tau)$ where $G_1(\mathbf{m}, \tau)$ is the field autocorrelation measured at a location $\mathbf{m}$ on the boundary of the object. Note that the function F is the representation of the CDE by posing it as a function mapping the MSD to the field auto correlation at the boundary. Since the MSD is a coefficient of the CDE, $G_1(\mathbf{m}, \tau)$ depends non linearly on the MSD, and hence F is a non linear function. We proceed to define the forward problem and the inverse problem as follows: Given the MSD of the scatterers, solving the CDE (2.50) to find the the field auto correlation function everywhere in the object (including the boundary) is called the forward problem. The inverse problem

seeks the MSD of the scatterers everywhere in the object using the measured field autocorrelation function only at the boundary. In other words, inverse problem requires the inversion of the nonlinear map F such that $< \Delta r^2(\tau) >= F^{-1}(G_1(\mathbf{m}, \tau))$. The nonlinear inverse problems are difficult to solve which often necessitates to adopt linearisation method [70, 71].

Let $< \Delta r^2(\tau) >^{\delta}$ be a perturbation in MSD from its baseline value $< \Delta r^2(\tau) >^{0}$. The function F can be expanded in terms of Taylor's series around the baseline value as

$$F(< \Delta r^2(\tau) >^{0} + < \Delta r^2(\tau) >^{\delta}) = F(< \Delta r^2(\tau) >^{0}) + hF'(< \Delta r^2(\tau) >^{0}) \tag{2.62}$$

where $h =< \Delta r^2(\tau) >^{\delta}$. Here F' is called the Frechet derivative [74] which represents the derivative of the function with respect to MSD evaluated at the baseline value of MSD. This is a linear function of MSD as we intended and hence invertible. Corresponding changes in the boundary measurement is the $G_1(\mathbf{m}, \tau)^{\delta}$ such that $F(< \Delta r^2(\tau) >^{0} + < \Delta r^2(\tau) >^{\delta}) = G_1(\mathbf{m}, \tau)^{\delta} + G_1(\mathbf{m}, \tau)^{0}$ which gives

$$G_1(\mathbf{m}, \tau)^{\delta} = hF'(< \Delta r^2(\tau) >^{0}). \tag{2.63}$$

The above equation relates the perturbations in MSD to perturbations in measurement via the Frechet derivative of the function F and hence is called the sensitivity relation. Similar to the fact that F represents the CDE, we can derive the equation for F' by substituting for MSD $< \Delta r^2(\tau) >^{0} + < \Delta r^2(\tau) >^{\delta}$ and the corresponding field autocorrelation $G_1(\mathbf{r}, \tau)^{\delta} + G_1(\mathbf{r}, \tau)^{0}$ in the CDE (Equation 2.50) which gives:

$$\begin{aligned} &- \nabla \cdot D(\mathbf{r}) \nabla \left(G_1(\mathbf{r}, \tau)^{\delta} + G_1(\mathbf{r}, \tau)^{0} \right) \\ &+ \left(\mu_a(\mathbf{r}) + \frac{1}{3} \mu_s' k_0^2 (< \Delta r^2(\tau) >^{0} + < \Delta r^2(\tau) >^{\delta}) \right) \\ &\left(G_1(\mathbf{r}, \tau)^{\delta} + G_1(\mathbf{r}, \tau)^{0} \right) = S_0(\mathbf{r} - \mathbf{r}_0), \end{aligned} \tag{2.64}$$

Subtracting above equation from CDE in Equation 2.50 we have

$$-\nabla \cdot D(\mathbf{r})\nabla G_1(\mathbf{r},\tau)^{\delta} + \left(\mu_a(\mathbf{r}) + \frac{1}{3}\mu_s' k_0^2 < \Delta r^2(\tau) >^{\delta}\right)$$
$$G_1(\mathbf{r},\tau)^{\delta} = -\frac{1}{3}\mu_s' k_0^2 < \Delta r^2(\tau) >^{\delta} (G_1(\mathbf{r},\tau)^{\delta} + G_1(\mathbf{r},\tau)^{0}) \tag{2.65}$$

The above equation clearly shows a nonlinear dependence between $< \Delta r^2(\tau) >^{\delta}$ and $G_1(\mathbf{r},\tau)^{\delta}$ and hence to linearize we neglect the term $\frac{1}{3}\mu_s' k_0^2 < \Delta r^2(\tau) >^{\delta} G_1(\mathbf{r},\tau)^{\delta}$ which results in the linearized equation

$$-\nabla \cdot D(\mathbf{r})\nabla G_1(\mathbf{r},\tau)^{\delta} + \left(\mu_a(\mathbf{r}) + \frac{1}{3}\mu_s' k_0^2 < \Delta r^2(\tau) >^{\delta}\right) \tag{2.66}$$
$$G_1(\mathbf{r},\tau)^{\delta} = -\frac{1}{3}\mu_s' k_0^2 < \Delta r^2(\tau) >^{\delta} (G_1(\mathbf{r},\tau)^{0})$$

This linearization procedure is called *First Born approximation* [74, 75] where we have made use of the fact that $G_1(\mathbf{r},\tau)^{\delta} << G_1(\mathbf{r},\tau)^{0}$, i. e., the perturbations in field autocorrelation are very small compared to its baseline value. The function F' represents above equation which relates the perturbations in field autocorrelation to perturbations in MSD as a linear function. The inversion model can be now explained based on the above equations as follows: Obtain the baseline measurement $G_1(\mathbf{m},\tau)^{0}$ and subsequently the measurement induced by the perturbation (in MSD) which is $G_1(\mathbf{m},\tau)^{\delta} + G_1(\mathbf{m},\tau)^{0}$. Subtracting these two measurements results in perturbation in measurement $G_1(\mathbf{m},\tau)^{\delta}$. The perturbations in MSD $\langle \Delta r^2(\tau) \rangle^{\delta}$ can be obtained by solving the minimization problem [76]

$$\underset{h}{\text{minimize}} \| hF'(< \Delta r^2(\tau) >^{0}) - G_1(\mathbf{m},\tau)^{\delta} \|_2^2 \tag{2.67}$$

where $\|x\|_2 = \sqrt{(x'x)}$ ($'$ denotes transpose) is the euclidean norm in case of finite dimensional spaces. The above minimization problem can be solved in finite dimensional space using analytic Greens function solution to the CDE, the details of which in the context of speckle contrast imaging is explained in the Section 4.2.

Before concluding the chapter we briefly touch upon the linearized inverse problem as a minimization problem in a finite dimensional space. We introduce a small notational change in order to avoid cumbersome expressions. As explained above, most of the tomographic reconstruction problems are categorized as non linear optimization problems for which we formulate a corresponding linearized inverse problem which can be expressed as a system of linear equations:

$$y = Ax \tag{2.68}$$

Here y is the measurement vector of size $m \times 1$ and x is the solution vector of size $n \times 1$. A is the matrix,of size $m \times n$, for the linear transformation, which is called the Jacobian (sensitivity matrix). Where m is the number of detectors and n is the number of grid points where the solution x is sought. Note that y, A and x represents $G_1(\mathbf{m}, \tau)^\delta$, F' and $h(=< \Delta r^2(\tau) >^\delta)$ respectively. The solution to the above inverse problem can be recasted as a minimization problem:

$$\min_x \|Ax - y\|_2^2 \tag{2.69}$$

where the Euclidean norm is defined as : $\|x\|_2 = \sqrt{x^T x}$, x^T being the transpose of x^T. The above minimization problem can be solved by solving the Normal equations:

$$A^T A\hat{x} = A^T y \tag{2.70}$$

where $\hat{x}$ is the solution we seek. Due to ill-posedness of the problem, its often necessary to regularize [77, 78] the above minimization problem where we try to minimize the following modified problem:

$$\min_x \|Ax - y\|_2^2 + \lambda \|Lx\|_2^2 \tag{2.71}$$

where λ is the regularization parameter and L is the regularization operator which we take as an identity matrix. The corresponding normal equation to be solved is given as:

$$(A^T A + \lambda I)\hat{x} = A^T y. \tag{2.72}$$

We will be adopting a spatial regularization scheme to solve the above regularized problem which is explained in detail in Section 4.2.

3

MULTIMODAL OPTICAL SYSTEM FOR LONGITUDINAL IMAGING OF THE RODENT BRAIN

Laser speckle imaging in combination with optical intrinsic imaging (OIS) have been demonstrated to be a great tool to measure quantitatively superficial blood flow, total hemoglobin concentration and oxygen saturation simultaneously. These have been used together particularly in brain animal experiments as it is capable of mapping several biologically significant parameters over a large field of view to with ~ 25µm resolution. [15, 79]. These characteristics have been employed to study brain hemodynamics under cortical spreading depression and functional activation [79], focal cerebral ischemia [15], the effect of electrical forepaw stimulation after a focal cerebral ischemia [80], outcome from global cerebral ischemia[81], investigating the effects of substances in the brain hemodynamics [82], all of them in rats. Besides brain studies, the LSF-OIS technique has been used to study the hemodynamic response of the rat lumbar spinal cord [83].

An LSF-OIS combined imaging device was constructed in the Medical Optics group of the Institute of Photonics Sciences. As part of my project, I assisted in the completion and testing of the system, using both microfluidic phantoms and *in vivo* experiments in mice. The completed LSF- OIS device allows surface imaging of CBF, oxygenation and volume in rodents with ~ 30µm axial resolution. This setup allowed us to perform a multidisciplinary study of the effect of the Mannose-binding Lectin protein in the recovery following transient ischemic stroke in mice with the Department

of Brain Ischemia and Neurodegeneration from the Institute for Biomedical Research in Barcelona (IIBB).

Longitudinal studies investigate dynamic parameters that change over the course of hours, days and even weeks. These types of studies are particularly challenging in spectroscopic and quantitative studies, as they require the animal to be moved between measurements, which in general introduces systematic errors [84, 85]. In the following protocol that will be presented, the animal is moved from the device at least 4 times over the course of eight hours (Figure 3.14). To avoid systematic errors we developed some solutions including real-time alignment, calibration procedures and post-processing algorithms that are described after.

This chapter describes the LSF-OIS device and includes all the experimental methods that were developed during this work. At the end we present the results from the animal study which represents the application of our device and developed methods; and its validation in comparison with the findings made with other techniques.

3.1 EXPERIMENTAL SETUP

3.1.1 *Laser Speckle Flowmetry instrument*

In general, the standard elements of a laser speckle flowmetry device are a laser to illuminate homogeneously the tissue and an imaging system to acquire the speckle patterns formed at the tissue surface over time. The wavelength of the laser should be chosen according to the application which in our case is usually in the near infrared range. The imaging system consists of a camera and an objective lens with a variable aperture that allows adjusting the field of view and, at the same time, the speckle to pixel size ratio.

For this device we employed a laser diode (DL7140-201S, 785 nm, 70 mW, Thorlabs, USA), mounted in a temperature- controlled laser diode mount (LDM21, Thorlabs, USA). The laser diode was driven the constant current mode (LDC205C, Thorlabs, USA) and

temperature-controlled for intensity stability (TED200C, Thorlabs, USA). In order to obtain a homogeneous illumination of the surface under study, the laser was set apart from the surface allowing the beam to diverge until it covered the surface homogeneously as confirmed by images of the illuminated field.

The first element of the imaging system was a monochrome CCD camera (Basler scout scA640-74fm, Basler, Germany), with a 659x494 resolution, a pixel size of 9.9 µm x 9.9 µm and 12 bit depth. To complete the imaging system we chose an objective with focal length of 50 mm, variable aperture with f/# from 2.8 to 16 in a click-stop format (Rodagon, Rodenstock Photo Optics, Germany). To adjust the magnification of the system, the focal length has to be adjusted. For fine adjustment, and to to avoid the lens to rotate while changing the focus, a Modular-Focus (Rodenstock Photo Optics, Germany) was included. For coarse adjustment extension tubes with a length of 24.5 mm or 45 mm could be included. This imaging system was set on a x-y- z translational stage to give some freedom when setting the field-of-view and to select the imaging plane to the surface of the sample without changing the focus of the camera (and therefore changing the speckle size). In order to make the calibration of the system we used a multi-function high magnification calibration target 20X-40X (Edmund Optics, USA) which was put in a platform with a height coinciding with the mouse brain surface height.

3.1.2 *Optical Intrinsic Signal imaging instrument*

As mentioned before, OIS works by using different wavelengths for illumination. Previously, the common method to obtain those wavelengths involved the use of white lamps together with different wavelength bandpass filters [15, 79, 80]. With the availability of light emitting diodes (LEDs) at different wavelengths, these started being included in the OIS systems replacing the bandpass filters [81, 83, 86]. For our OIS system we preferred the latter approach and opted for an objective-mounted LED source [86]. In this source, several LEDs are mounted on a ring that could be attached to the camera objective without obstructing it, as observed

in Figure 3.1a. This provides a fairly spatially homogeneous light and allows illuminating the sample perpendicularly.

We built this system to have 4 different wavelengths, 525 nm (green), 590 nm (orange), 635 nm (red) and 780 nm (NIR) (Table 3.1, Thorlabs, USA). The mounting ring was able to hold 12 LEDs in one row, 3 for each wavelength, and were positioned alternating the colors, 4 times, as seen in Figure 3.1c, to have a homogeneous angular distribution of the illumination for each wavelength. Each LED color group was controlled with a variable intensity driver (T-Cube high power LED driver, LEDD1B, Thorlabs, USA). In order to improve the homogeneous illumination, we included a non-coloured diffusive plastic all around the LEDs.

Reference	center λ [nm]	power* [mW]	FWHM** [nm]
LED525E	525 ± 15	2.6	32
LED591E	590 ± 10	2.0	20
LED631E	635 ± 10	4.0	10
LED780E	780 ± 10	18	30

Table 3.1: Specifications for the LEDs included in the OIS device. Extracted from Thorlabs. *Total optical power. **Full width at half maximum.

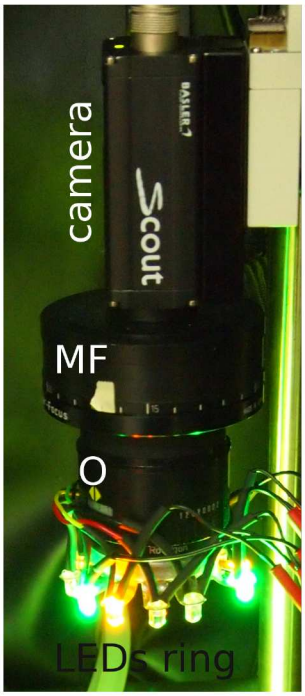

(a) Objective-mounted LED source. MF: modular focus; O: objective.

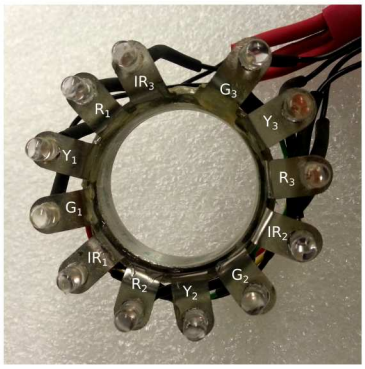

(b) Detail of the LED positions in the ring. Bottom view. IR:780 nm, R: 635 nm, Y:590 nm, G:525 nm.

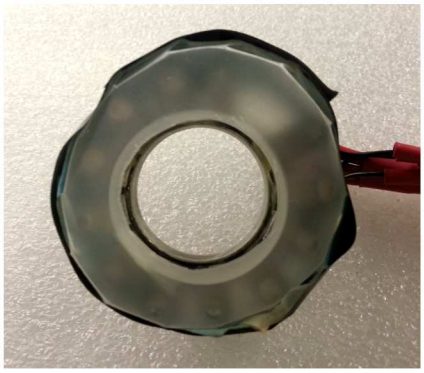

(c) Bottom view of the ring with the non-coloured diffuse plastic cover on.

Figure 3.1: Details of the OIS illumination ring.

3.1.3 *Hybrid imaging instrument*

The two systems described before were set together in order to have a multimodal imaging device capable of measuring superficial blood flow, as well as total hemoglobine concentration and oxygen saturation. The challenging part on hybridizing this two systems corresponded to the design of the electronic chain to properly synchronize the camera acquisition with the illumination time of the laser from the LSF and the LEDs from the OIS, including the order of entrance of each light source, as schematized in Figure 3.3. Synchronization was possible by including into the system the custom-made I/O device (I/O module TE2011.188, ICFO) presented in Figure 3.2a. This I/O device provides 8 analogical input (AIN), 4 analogical output (AOUT), 12 digital input (DIN) and 20 digital output (DOUT) ports, as observed in Figure 3.2b, but for this application only the digital ports were used. In particular, this I/O device has some virtual channels (Marking channels) that allow triggering a signal in a digital output from a signal in a digital input (DIN), and which play a key role in this timing sequence of the sources.

(a) Front view.

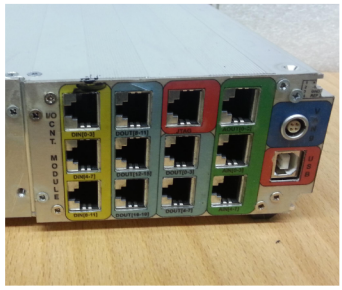

(b) Detail of the input/output ports in the back.

Figure 3.2: Custom-made I/O device to control the LSF-OIS illumination and acquisition timings.

The image acquisition sequence, or illumination cycle, was set to have one dark frame, one red frame, one orange frame, one green frame, one NIR frame, followed by 9 laser speckle images and repeating the whole cycle until the acquisition time was completed. The dark frame at the beginning of each cycle helps in the

post processing as a reference when separating the frames for each wavelength. To achieve this sequence a control procedure for the I/O device was designed and is explained here after.

The software (Section 3.1.4) sends a start signal to the I/O device and the DOUT0 triggers simultaneously the camera and the DIN0. The camera follows a cyclic signal with period $T1 + T2$ equal to the frame duration, i. e., 1/framerate (framerate=31.6 fps), where $T1 = 5$ ms and $T2 = 25$ ms. The exposure time for this system could go from 1 ms to a maximum of 20 ms, and as seen from the camera timeline in Figure 3.3, the maximum exposure time is not equal to T2. The DIN0 will trigger, through a marking channel, a signal in the DOUT1, that will make the I/O device to start an illumination cycle with a total duration of 420 ms. This signal from DOUT1 will trigger the simultaneous start of the LEDs cycles and as seen in Figure 3.3, each LED color group has a defined delay time from the trigger signal reception to the time of the emission and it is well defined in terms of T1 and T2. The emission time for every LED color group was set to 28 ms and the delay time between one color turns off and the next turns on is 2 ms. The LED color groups receive the signal from the DOUT $2-5$. The DOUT5 apart from giving the signal to the last LED group, triggers by its falling edge the DOUT6 that drives the laser. Again there is a delay of 2 ms between the LEDs and the laser illumination and it is kept on untill the 9 speckle frames are acquired. Once the cycle is completed, the master signal from the DOUT1 starts again.

The LSF-OIS system was completed with a custom-made dark cage to ensure that any external light could affect the measurements, given that this system had to be working in a fully illuminated Biology laboratory. The dark cage was completed with dark curtains at the front to allow easy access to the setup or to check the animal during the animal measurements. An image of the finished device is presented in Figure 3.4.

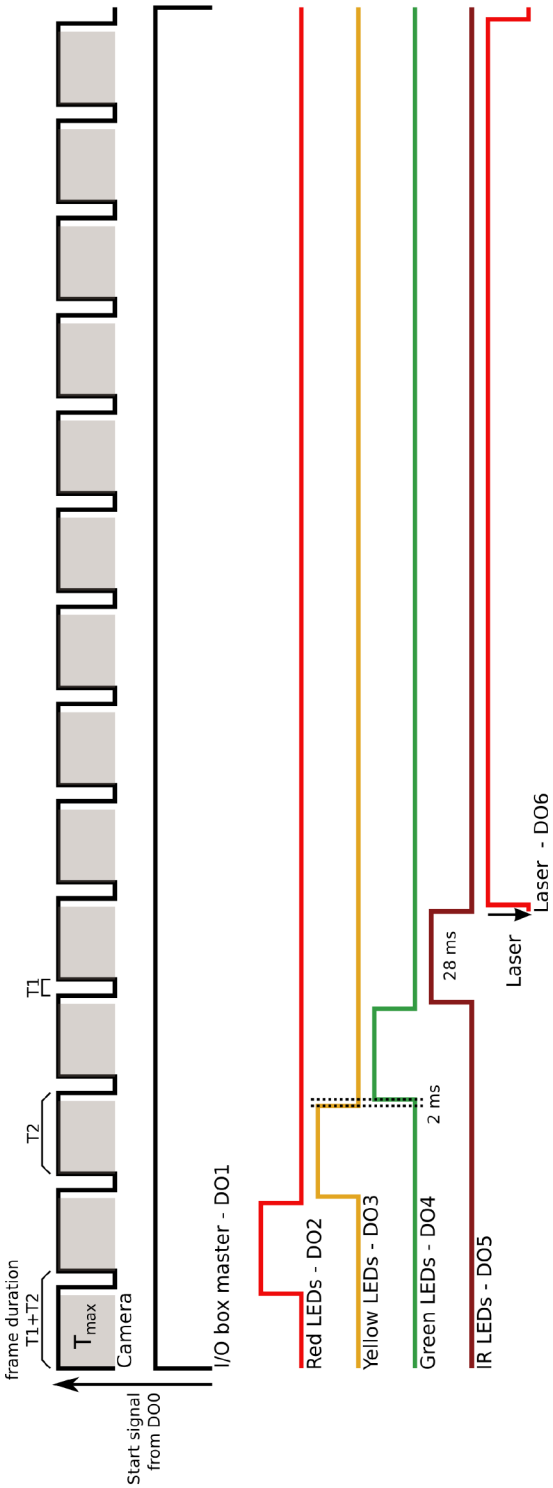

Figure 3.3: Schematic of one acquisition cycle for the LSF-OIS device, showing the synchronization between the illumination and the frame acquisition. The light source ordering and timing are also presented.

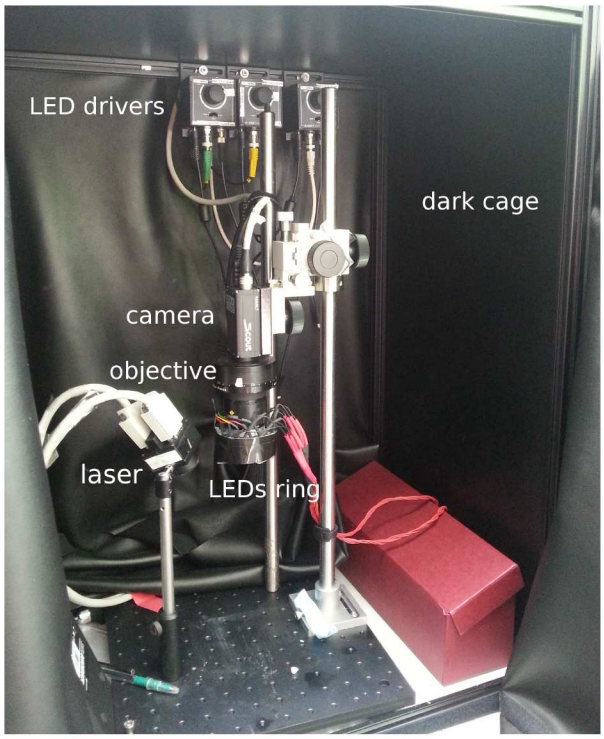

Figure 3.4: LSF-OIS completed setup inside the dark cage. The box to the right of the optical breadboard kept the connecting cables for the LEDs.

3.1.4 *Control Sotware*

The LSF-OIS system uses a software to code the instrument controls that is based on the SPLASSH (SPectral Light Acquisition Software for Signaling and Hemodynamics) software [87] from the Laboratory for Functional Optical Imaging at Columbia University in New York[1].

The SPLASSH was developed as a control tool for multispectral imaging and includes the libraries to work with a variety of cameras with IEEE 1394 FireWire connections as the Basler scout we used in our device and appeared as a good starting point to develop our control software. SPLASSH code and graphical user

1 We specially thank Prof. Ellizabeth Hillman for providing us with the software.

interface (GUI) was programmed in C and written within the National Instruments LabWindows/CVI environment. It includes the commands to interact with NI hardware interface drivers and with an Arduino microcontroller to program the LED sequences.

Using the same programming environment, the SPLASSH code and GUI were significantly modified to integrate the I/O device control commands that made possible the synchronization scheme described before, and to include the LSF measurements in the software. Furthermore, an interesting tool that enable making a real-time registration (Section 3.2.2) of the images at one time point during an experiment with an image from a previous time point was included.

3.2 IMAGE REGISTRATION AND LED INTENSITY CORRECTIONS

As described before, there are some longitudinal studies in which the animal has to be moved in and out of the imaging system and awaken between measurements. This may cause errors given that the calculation of the relative cerebral blood flow (rCBF) and the changes in absorption, from the OIS, are done for each time point with respect to the baseline. Then it is necessary to guarantee that the position of the animal in one time point is as close as possible to the position during the baseline. To do so, some fiducial markers were attached to the animal skull and were kept for the duration of the protocol and some mechanical elements where introduced in the setup. Apart from this, a real-time registration procedure was included in the SPLASSH software, that allows moving the animal during the measurement to achieve the desired position. If the real-time registration is not good enough due to time constraints of the experiments, a post-processing registration is performed in the images. From the OIS point of view, one difficulty that could appear in long-time protocols is the variability of the light sources intensity over time. To correct this problem a white reflectance surface is included in the FOV.

3.2.1 *Fiducial markers and mechanical additions*

Two types of fiducial markers were placed in the skull to help the registration process after each re-position of the animal into the device. The first type of references consisted in marking the skull in three places with the drill, without penetrating the skull, and then marking the holes with permanent ink to keep the marks during the whole experiment. As seen in Figure 3.5a two of the wholes are positioned in the anterior part of the brain before the bregma and the last one is set in the posterior part adjacent to the cerebellum and in the center of the hemispheres.

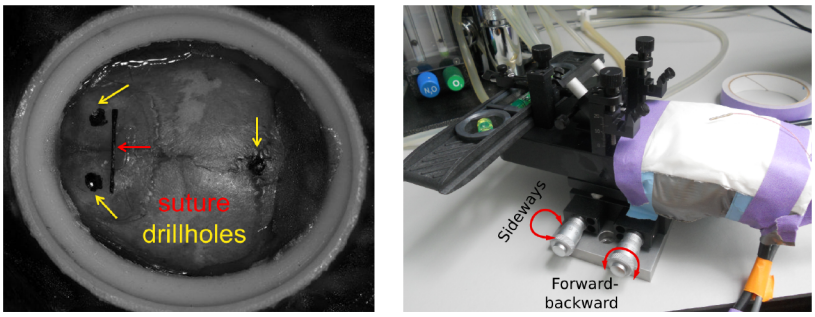

(a) Reference markers (drillholes and suture) and renormalization element (teflon ring) on a mouse brain.

(b) Stereotaxic frame with mouse electrical blanket attached to a two axes tip-tilt stage.

Figure 3.5: Implemented experimental methods to improve the real-time image registration.

The second type of fiducial marker consisted on a piece of suture which was glued to the skull between the anterior drillholes and the bregma. It is important to note that none of these markers interfered with the regions of the animal brain under study.

Normally, for this type of studies the animals are fixed in a stereotaxic frame. For our study, the stereotaxic frame was modified to be attached to the setup breadboard and to improve the real-time positioning time a two axes Tip-Tilt Stage (Edmund Optics, USA) was set under the stereotaxic frame. This tip-tilt stage has two micrometric screws that allow tilting the animal smoothly

in a forward-backward direction as well as in a sideways direction as seen in Figure 3.5b.

3.2.2 *Real-time registration*

In the longitudinal study we performed on mice using this LSF-OIS device, the animal had to be moved in and out from the imaging device between measurement points. During the initial tests of the device, the animal re-positioning after a measurement relied on the person ability and criterion to decide if the position of the animal was close enough to the baseline position and was completed by post-processing registration methods. Nevertheless, this was found to be very imprecise and most of the times even the post-processing co- registration of the images from one point to the baseline images was not enough to correct the position. To overcome this, inside the SPLASSH we included a procedure in which it is possible to realign the animal position to the baseline position.

The firs step in the real-time registration procedure is to acquire some 8-bit images of the brain before starting the baseline measurements with all color LEDs on. One image is taken focusing on the suture, another focusing on the back drill hole and the last one focusing on the vessels after the mineral oil cleared the skull. After the animal has been repositioned for another time point measurement, is where the real-time registration is needed.

The principle under it relies in comparing the baseline image with the real-time FOV preview. The comparison is done using the absolute difference NI IMAQ image processing function that subtracts one image from another and returns the absolute value of the difference. The resulting image is shown on screen while the registration is performed. Figure 3.6a show an example image of the resulting difference image when the initial placement does not correspond to the baseline position. The largest differences in the image appear in white and coinciding regions in black. Here is where the fiducial markers play an important role because the non-coincident drillholes show a higher contrast. Then, the goal during

the real-time registration would be to make the fiducial markers coincide with the white spots using the tip-tilt stage and try to get a result like the one in Figure 3.6b. At each measurement time point, the real-time registration starts with respect to the baseline image focusing on the suture. Once this fiducial marker is registered, the process is repeated for the drillhole and the same vessels chosen during the baseline.

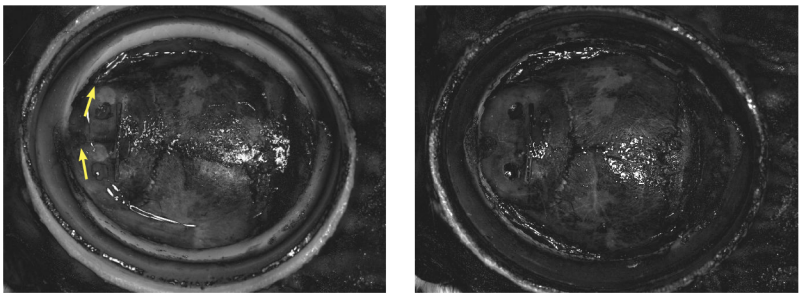

(a) Real-time view of the initial placement of an animal.

(b) Good alignment reached during the procedure.

Figure 3.6: Real-time image registration. The goal is to match the drill holes in the skull with the white spots presented in Figure 3.6a as attained in Figure 3.6b.

3.2.3 *Post-processing registration*

When an experiment is subject to a rigid schedule in favour of the animal well-being or to accomplish protocol demands, the time for a real-time registration is limited and sometimes it is necessary to proceed with the experiment without having attained a perfect re-positioning of the animal. This situation is presented in Figure 3.7a, where an image of the baseline position, in red (false color), is overlapped with an image of another time point, in blue (false color). The mismatch of the images is clearly seen in almost all the vessels where the two colors are distinguishable; the regions in which the images are matching, appear in violet. To overcome this potential situation, we implemented some procedures that are applied onto the images during the post-processing, entirely performed in fiji[88], and that will give as a result the co-registration of the images (Figure 3.7b).

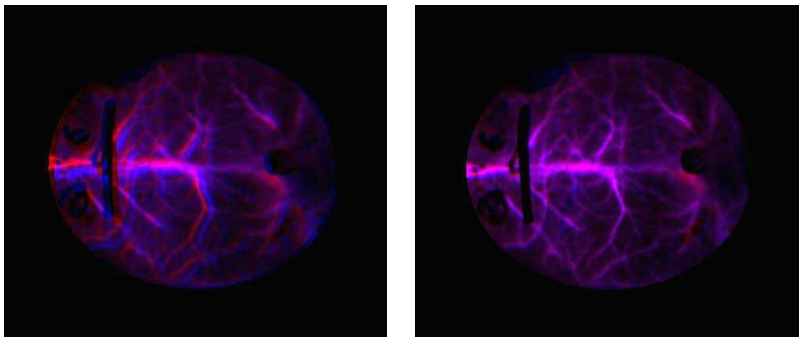

(a) Misaligned images after a poor real-time registration.

(b) Alignment of the images after post- processing registration.

Figure 3.7: Post-processing image registration. The images show "red" and "blue" as mismatched sections and "violet" as overlaps.

The procedures differ a bit for the LSF and OIS images and are described here:

LSF IMAGE PROCESSING The post-processing described here is applied to the whole stack of images available for a given measurement time point in the protocol.

- Rotation of the images, using a bicubic rotation, to put the middle cerebral line horizontally.
- Set noisy frames to NaN values to exclude them from the measurements: Motion artifacts, e. g., mouse breathing or vibrations, contribute to additional blurring of the speckles, reducing the speckle contrast that will result in overestimation of the flow at a given time. To determine those frames, we used the teflon ring as a standard. Being a solid, the standard deviation of the speckle contrast should not change over time. We took the average speckle contrast on a ROI defined on the ring and compare it frame by frame; if it deviates by more than 15% then that frame is considered to have too much artificial motion and the frame is blanked out.
- Calculate one reference image as the temporal average of the raw images over all the stack, usually 5 minutes.

- The reference image is sharpened twice to get well- defined vessels and to ease the alignment process.
- This reference image is put as the first image of the stack, and the stack's colourmap is changed to blue. Then, the baseline sharpened image with red colourmap is put as an overlay at 60% opacity Figure 3.7a.
- An interactive rigid rotation or an interactive affine rotation was applied to align the major visible vessels. This alignment is carried over to the whole stack.

After this procedure, the stack is ready for the speckle contrast calculations.

OIS IMAGE PROCESSING For OIS, the procedure is very similar but we skip some of the points. We skipped the noisy frames exclusion procedure because OIS is not as sensitive to motion artifacts as LSF: the distance moved by the mouse is small, and we are averaging over time and over a very large ROI.In our calculations For the reference image, used in the registration, we chose the green LED images since those have higher contrast to distinguish the vessels. The images from all colors are processed together by creating a green/red /orange stack. An extra procedure that is done to the OIS stacks is to invert the images so the vessels are bright instead of black. The registration is done by overlaying the inverse of the baseline image.

3.2.4 *Intensity Renormalization*

In reflectance measurements, it is important to have a reflectance calibration standard that returns always a known amount of the incident light back into the measuring device. For this study we designed a teflon ring that served as a white reference for the OIS reflectance measurements and attached it to the mouse skull as seen in Figure 3.5a.

The reflectance measurements for each wavelength at every time point of the protocol where renormalized considering the teflon

ring reflectance as constant along the whole protocol. This compensation for I_0 changes using the teflon ring was done using the folowing relation:

$$\Delta A = \log(\frac{1}{I_0 c}) \tag{3.1}$$

where $c = I(t)/I(t_0)_{ring}$ is a correction factor for the intensity. The quantity $I(t_0)_{ring}$ is calculated as a spatial average over the flat portion of the ring (excluding bright spots and hairs) followed by the time averaged over the frames acquired during baseline. The effect of the intensity renormalization is observed in **??**, where it can be seen that before any correction (dashed line) the teflon presented changes in absorption. This shows the need for the renormalization correction since in a reflectance standard, there should not be any change in absorption. After applying the renormalization correction (solid line), there are not changes in absorption in the teflon ring, confirming the effect of the correction over the reflected intensities.

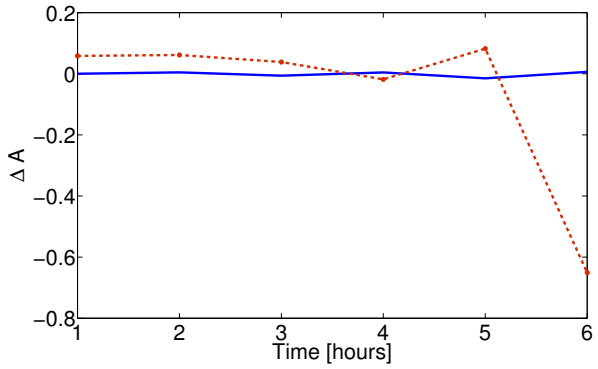

Figure 3.8: Changes in absorption in the teflon ring at different time points of a longitudinal study. The dashed line shows ΔA without any correction while the solid line shows the renormalized change in absorption.

Apart from this renormalization role, the teflon ring was used as a speckle contrast standard, as described in the post-processing procedure for LSF images. Furthermore, the ring was designed to retain the mineral oil that helps clearing the skull and keeping the skull from drying without causing shadows inside the imaged regions of the brain.

3.3 VALIDATION TESTS

In order to test the actual capabilities of the LSF-OIS device, some preliminary tests were performed. This tests included some phantom measurements (omitted here) and some *in vivo* measurements in mice.

Prior to start any measurement some general procedures were completed. After starting the software, the laser and the LEDs were allowed to warm up for at least 5 minutes. Afterwards the LEDs' input voltages (measured at the cube driver output) and the laser current were checked and adjusted to some determined values to ensure a constant illumination intensity throughout all the different measurements done, e. g., all the animals measured in a study. Finally, in the case of an animal study, the tip-tilting stage that held the stereotaxic frame and attached it to the setup was levelled before the animal was fixed to the frame.

3.3.1 *In vivo tests in mice*

Before moving to a complete animal study, it was necessary to check the performance of the LSF-OIS system and its ability to measure changes in flow in an animal model. To do that, some tests that induce changes in cerebral blood flow over time were performed in mice. In particular the results for a temporal middle cerebral artery occlusion (tMCAO) are presented after the general procedures for the animal preparation are explained. A diagram of the setup used for mice brain imaging studies is presented in Figure 3.9.

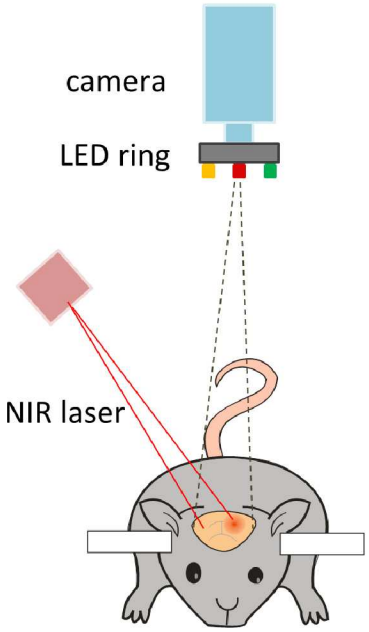

Figure 3.9: Schematic of the laser speckle flowmetry and optical intrinsic signal imaging (LSF-OIS) multimodal device.

3.3.2 *Animal preparation*

The animal was anesthetized in a glass box by isoflurane inhalation and then, it was put in a lab standard stereotaxic frame with mouse adaptor (Stoelting Co., USA), where a gas anesthesia mask (Stoelting Co., USA), continued providing the anesthesia during the measurements. The temperature of the animal was monitored continuously using a rectal probe and mantained at a constant temperature of 37° with an in-house feedback controlled electrical blanket. The mouse scalp was opened and the periosteum removed. To help the registration of the images, the fiducial markers (drillholes and suture) were included as explained in Section 3.2.1. Afterwards, the teflon ring was attached to the skull using dental cement. The animal was put into the imaging device and the camera focused on the skull surface. A verification test for hair strays in the FOV and for motions of the skull that could interfere with the speckle measurements was performed. An image of the animal inside the LSF-OIS device is presented in Figure 3.10.

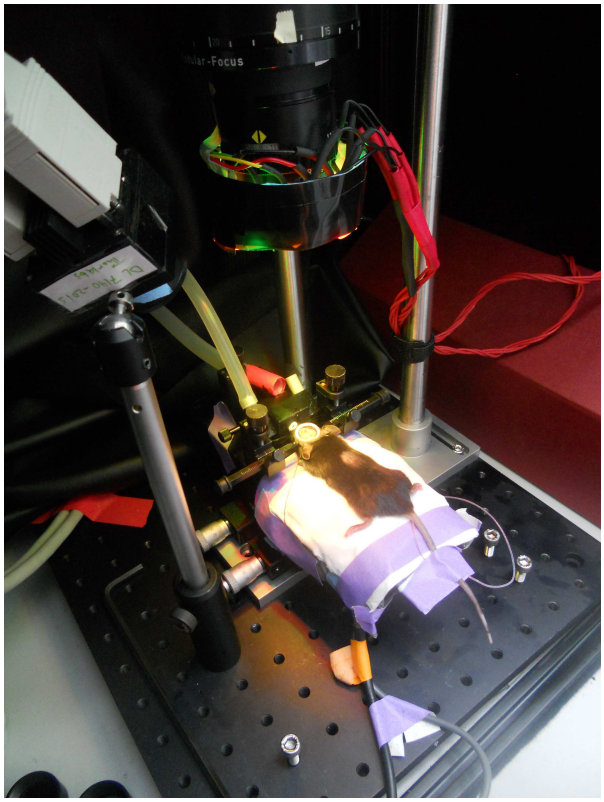

Figure 3.10: Image from the animal after preparation and inside the LSF-OIS device.

3.3.2.1 *Temporal middle cerebral artery occlusion (tMCAO)*

A very useful way of understanding the ischemic stroke in humans is through experimental ischemic stroke models, usually carried out in rodents [6]. In humans, the ischemic stroke occurs mostly in the territory of the middle cerebral artery (MCA), hence, the majority of ischemic stroke studies in mice and rats involve the occlusion of the MCA. Due to the reduced variability of the resulting ischemic lesions one of the most used methods is the temporal middle cerebral artery occlusion (tMCAO). This method consists on occluding the MCA during ninety minutes by introducing an intraluminal suture through the external carotid artery (ECA) [6, 13]. With this in mind, a determinant test for the LSF-

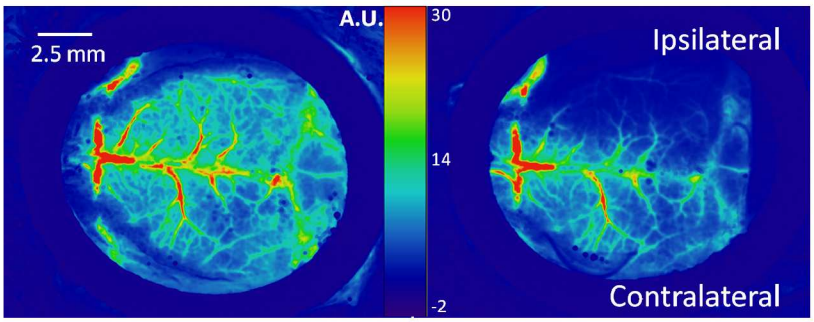

Figure 3.11: Flow images of a mouse brain before ischemia (left) and during occlusion(right). Red regions represent high flow while blue represents low flow.

OIS capability to measure the changes in cerebral blood flow was a tMCAO in a mouse.

A wild type mouse with a C57BL/6J genetic background was prepared as described in Section 3.3.2. Speckle measurements were taken during 15 minutes in 5 minutes sets for the baseline with an exposure time of 5 ms. Afterwards, the animal was removed from the imaging system for the occlusion surgery. The animal was occluded using an intraluminal suture and the occlusion was confirmed by laser doppler flowmetry measurements. After 45 minutes of occlusion, the animal was moved back into the system and again speckle measurements were performed following the same scheme used in the baseline acquisition.

The images were corrected during post-processing and the speckle contrast was calculated in each image using a 5x5 pixel size window. For each time point, the baseline and the occlusion, we calculated one speckle contrast image by averaging all the images in the stack. Afterwards, the flow was calculated for each of the stages and the 2D maps of flow for baseline (left) and occlusion (right) are presented in Figure 3.11. In this images, the red regions represent high flow, whereas the blue regions represent low flow. The values of flow showed in this graph are given in arbitrary units. In the baseline image, both hemispheres are showing similar flows and the major vessels show higher flows. At the time of the occlusion, the ipsilateral hemisphere, where the occlusion was

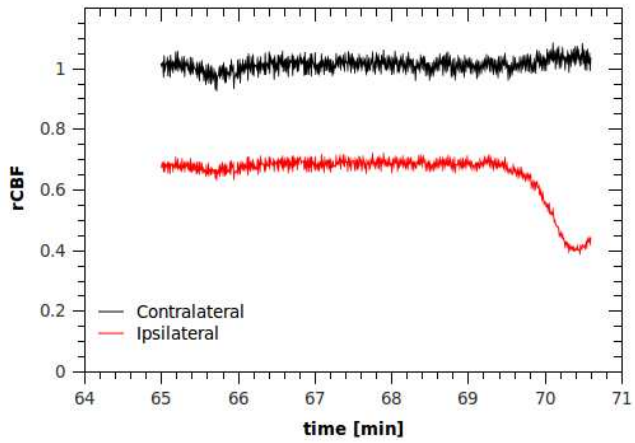

Figure 3.12: Change in CBF during the occlusion for both hemispheres relative to the flow in the contralateral side at the beginning of the occlusion. The spontaneous reduction of CBF towards the end of the study in the ipsilateral side is due to a PID. Many PIDs are observed in stroked animals and their frequency and amplitude is relevant to the extent of damage.

performed, shows a clear reduction in flow in comparison to the basal flow and in comparison to the healthy hemisphere.

In order to extract the quantitative information from these images rCBF is calculated. If the rCBF during occlusion is calculated in the ischemic hemisphere with respect to the flow of the same hemisphere during the baseline, it is found that the reduction in the flow is $\approx 80\%$, i. e., , only 20% of the healthy CBF is circulating in the ischemic state.

It is known that during occlusion, there is activity in the penumbra (region that surrounds the ischemic core) and that is viable at the beginning of the occlusion but could become damaged tissue with time. In order to observe such activity, we defined an ROI over the penumbra in the ipsilateral hemisphere and compared the rCBF with respect to the flow in a mirrored ROI localized in the healthy hemisphere during the time course of the occlusion. The results are presented in Figure 3.12. In black it is presented the flow in the contralateral side which is very constant and in red the flow in the ipsilateral side. It is seen that the flow in the

penumbra of the ischemic side is 30% less than the flow in the healthy side and stays constant during the first 4,5 minutes of observation. After this time the flow is reduced an extra 30%, which shows evidence of Peri-Infarct Depolarizations (PID), which are spontaneous waves of depolarization (cell membrane) spreading from the core of the infarct that are believed to increase the size of the infarction [15].

These results show that the LSF device was able to follow a process of flow, in this case, monitoring the flow changes during a tMCAO and demonstrated that is was ready to perform a study in animal models.

3.4 MANNOSE BINDING LECTIN PATHWAY STUDY

The LSF-OIS device was applied in a longitudinal study in collaboration with the Department of Brain Ischemia and Neurodegeneration at the Institute of Biomedical Research of Barcelona (IIBB). In a previous work [89], they showed that genetically modified mice (Mannose binding lectin (MBL) gene-knockout (KO) mice) with a deficiency of the MBL protein present protection after an experimental ischemic stroke, in other words, they have a better outcome (Figure 3.13a). This finding is based on the fact that the size of the infarction in MBL-KO mice is smaller at 48 hours following ischemia compared to wild type (WT) mice (Figure 3.13b), despite having similar reduction in cerebral blood flow (CBF) at the time of the occlusion, as measured by Laser Doppler. Figure 3.13c, represents an example of this finding where the "milky" white areas denote the infarct –i.e. damaged tissue– area in a brain slice. Interestingly, in recent clinical studies, stroke patients with MBL-low genotypes exhibited eleven times better outcome than MBL-sufficient genotypes [89] and the infarct volume difference observation was also confirmed in humans [90].

Motivated with this finding, they started a new study to understand the mechanism of this protection and the role of the MBL after the stroke using different techniques to measure different physiological parameters. Regarding the CBF, the initial hypothesis of the study was that the Lectin pathway activation affects the evolution of CBF in the first few hours after reperfusion following

middle-cerebral artery occlusion. In order to confirm or negate this hypothesis, the logical interest was to follow the evolution of the cerebral blood flow in the hours following the reperfusion and the LSF-OIS device appeared to be the idoneous tool for this task.

3.4.1 *Mannose-Binding Lectin (MBL) and Stroke*

Mannose-binding lectin (MBL) is a protein involved in the activation of the complement system through the *lectin pathway activation*. The complement system is a set of proteins present in the blood, body fluids and cell surfaces and is involved in immune and inflammatory reactions, apart from its bacteria killer function [91]. During a *ischemic* process, the blood supply that arrives to the tissue is temporally suppressed causing cell death and tissue injury which leads to inflammation. Intuitively, the restoration of the blood supply or *reperfusion* would improve the tissue condition, but contrary to this, it causes more tissue damage that triggers an intense inflammatory response [92, 93]. Such process is called an ischemia-reperfusion injury (I/R injury) and is commonly observed in cases of shock, tissue transplantation, myocardial infarction, stroke, certain infections, and arterial disease and trauma [92]. As inflammation and complement system are related, understanding the role of the complement system and its effects in I/R injuries in different organs has been the subject of numerous studies [92, 93].

In cerebral I/R injury the complement cascade is quite complex [94]. Many studies suggest that the MBL pathway aggravates stroke brain damage [95] by activating the thrombin which stimulates the formation of thrombus that will increase the brain damage after reperfusion following an ischemic process.

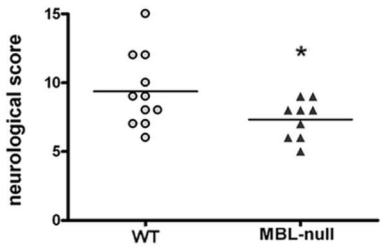

(a) The neurological score, as an indicator of the outcome, is better (lower) in MBL-null mice than in WT [89].

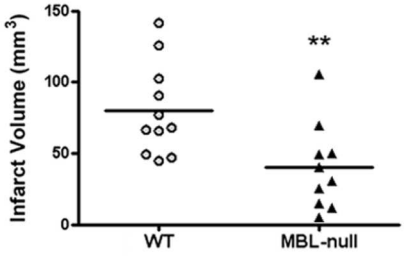

(b) Infarct volume was lesser in the MBL-null group (n = 11) than in WT (n = 10) [89].

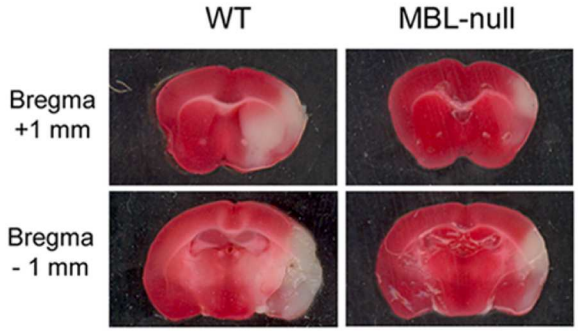

(c) Representative images of infarcted brain tissue in wildtype (WT) and MBL-null mice at 48 h post-ischemia showing that the knock-out (MBL-null) mice have significantly smaller infarct volumes. The approximate level of the brain sections is indicated in the left by the distance from Bregma [89]. The affected regions of the brain are distinguished by their "milky" white coloration.

Figure 3.13: Previous evidence showing that MBL-deficiency provides protection after experimental ischemic stroke in mice.Reproduced with permission of ©2010 Cervera et al. Genetically-Defined Deficiency of Mannose-Binding Lectin Is Associated with Protection after Experimental Stroke in Mice and Outcome in Human Stroke. PLoS ONE 5(2): e8433. doi:10.1371/journal.pone.0008433

3.4.2 *Measurement protocol*

With the objective of studying the evolution of the cerebral blood flow after reperfusion following a tMCAO, and the possible differences between two animal groups, we designed and agreed on a protocol with our collaborators from IDIBAPS-IIBB. All the animal preparation included in this protocol was performed by Dr. Xavier De La Rosa [96]. The animal work was undertaken with approval of the Ethical Committee of the University of Barcelona and in compliance with the Spanish law.

For this study, we used adult male mice (3-4 month-old), between 26-34 g, from two groups in the C57BL/6J background [89]: wild-type (WT) and Mannose-binding lectin knocked-out (MBL-KO or MBL-null) mice [97]. From each group, the number of animals included in the study was 5 (n=5).

The designed protocol is presented in Figure 3.14, where it can be seen the timeline of the animal during the experiment and the time at which the rCBF measurements took place. Animals in both groups were measured following exactly the same protocol.

The protocol started by preparing the animal following the methods described in Section 3.3.2 and performing baseline measurements of the CBF (basal CBF) during 15 minutes in sets of 5 minutes. Following this, the animal was removed from the imaging device and was subjected to a transient ischemia produced by intraluminal occlusion of the right middle cerebral artery (MCAO) during 90 minutes. To confirm the success of the occlusive procedure, the cerebral perfusion was assessed with laser Doppler flowmetry (Perimed AB, Järfälla, Sweden) during the first 30 minutes of the MCAO with a probe located in the territory of the MCA. An occlusion was considered successful if a 70% decrease in CBF from the baseline was registered. The animal was positioned again into the stereotaxic frame to monitor the CBF during the last 30 minutes of the occlusion using the LSF-OIS device. The animal was removed again out from the device to be reperfused exactly at 90 minutes from the occlusion, by removing the intraluminal filament. As soon as the reperfusion procedure finished, the animal went back to the imaging device to measure the CBF. For this time point rCBF was measured after $\approx$ 20 minutes from reperfusion and at 1 hour from reperfusion. Up to this point the animal

had been under anesthesia since the initial preparation. After the reperfusion measurement the animal was removed from the setup and allowed to recover from anesthesia. The CBF was measured again at 4 and 6 hours from reperfusion using the LSF-OIS device allowing the animal recovery between measurements. Every time the animal was moved out of the setup and put back for a measurement, an alignment was performed using the real-time registration (Section 3.2.2) procedure allowing a maximum time of 15 minutes after which the measurement had to start, to limit stress on the animal. After the 6 hour measurement, and without removing the animal from the device, it was sacrificed to determine the residual flow value after cardiac arrest [14]. Furthermore, the brain vascular anatomy was examined *ex vivo* after intravascular perfusion of carbon black ink in control WT and MBL-KO mice.

Due to the long time of exposure of the animal to anesthesia, and to check for possible effects of anesthesia during the measurements, a group of control mice were prepared under the same conditions and subjected to the same surgical procedures of the animals with tMCAO with the exception of the intraluminal occlusion (WT (n=3) and MBL KO (n=3)). The protocol timing was also respected. These animals are denominated here onwards *sham animals*.

For this study, the system was set to capture the whole mouse brain within the field of view and the exposure time was decided to be 5 ms, being this the optimal exposure time for mice brain studies [98].

Before performing any analysis into the images, every image was post-processed for co-registration with the baseline images.

During the measurements described before, the LSF-OIS device was operated in the multimodal option, in which it is possible to acquire images to measure the CBF as well as the hemoglobin concentration through OIS. With this in mind, results for both, LSF and OIS are presented in this section.

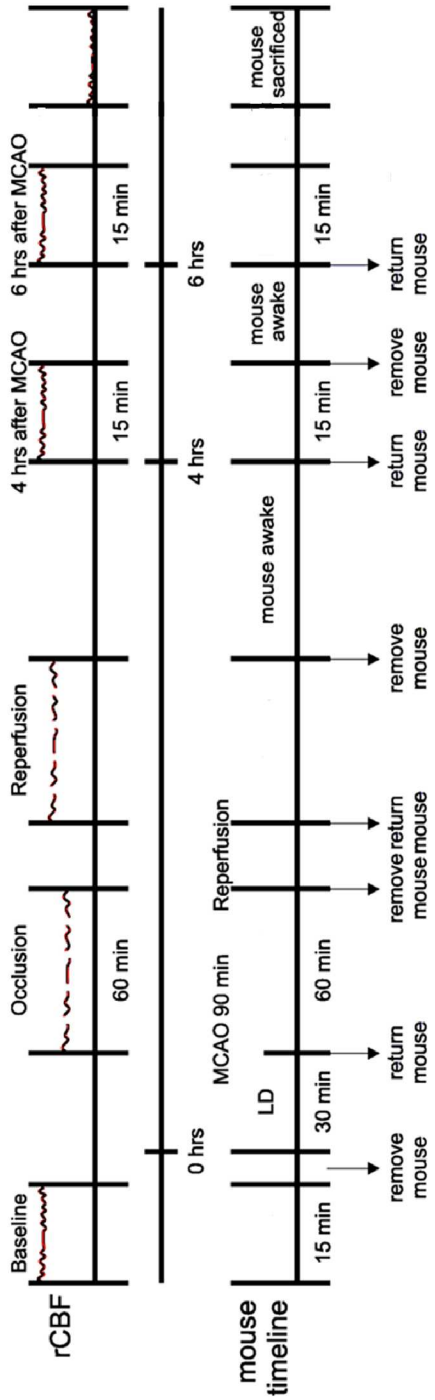

Figure 3.14: Timeline of the protocol followed with each animal included in the study.

3.4.3 *Laser Speckle Flowmetry*

In order to do the analysis of the CBF during the study, we defined four regions-of-interest (ROIs) as seen in Figure 3.15: Two in the hemisphere where the occlusion was performed, *ipsilateral*, and two in the opposite hemisphere, *contralateral*. In the ipsilateral hemisphere, we defined an ROI corresponding to the ischemic core, that coincided with the middle cerebral artery region in the mouse brain, according to a mouse atlas (MCA ROI), and another that included the surrounding region of the MCA (outside ROI). The ROIs in the contralateral side were defined by mirroring the ipsilateral ROIs into the contralateral side to ensure equal size areas for the comparisons between hemispheres. These ROIs were anatomically chosen for one mouse, and then related to all other animals in the study using the bregma as reference point.

For the calculation of the cerebral blood flow at a given time point and a given ROI, the calculation procedure contemplated:

- Calculating the speckle contrast using a 5x5 window on every image from the 9 taken every 0.5 seconds.
- Averaging pixel to pixel the 9 speckle contrast images to obtain one speckle contrast image every 0.5 s.
- Averaging all the speckle contrast images corresponding to a given time point of the experiment. Usually 5 minutes.
- Converting the speckle contrast images into flow images.
- Spatial averaging over the pixels within a ROI to obtain one flow value for that ROI.

In a longitudinal study, LSF does not provide absolute values of the CBF at each time point. To overcome this, the parameter that is calculated is the relative Cerebral Blood Flow (rCBF) which compares the flow at each time point to a previous reference flow: the basal flow. Hence, at each time point of the experiment, the cerebral blood flow relative to the baseline ($rCBF_{base}$) at a given ROI, was calculated according to the following relation:

$$rCBF_{base} = \left\langle \frac{\langle CBF(t)\rangle_t - \langle BZ\rangle_{t,x}}{\langle CBF(t)_{baseline}\rangle_t - \langle BZ\rangle_{t,x}} \right\rangle_x \tag{3.2}$$

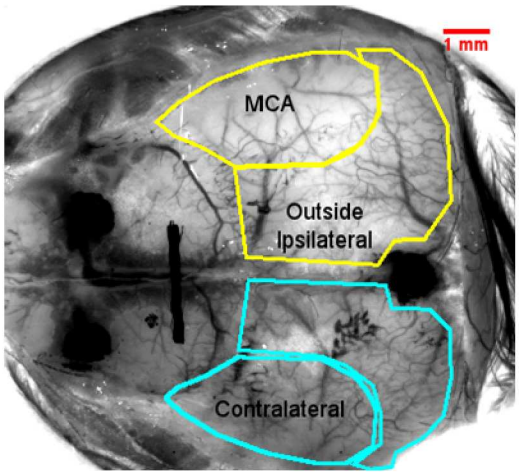

Figure 3.15: Defined ROIs in the mouse brain for the analysis of the data. The scale bar corresponds to 1 mm.

where the subscript x represents pixel averaging in the ROI, CBF(t) is the blood flow of a given ROI at a given time point of the experiment and BZ corresponds to the *biological zero* flow measured for each animal immediately after it was sacrificed. This BZ is a correction that has to be included to every blood flow measurement since by cardiac arrest, when there is no blood flow, there is a residual flow that corresponds to the random motion of scatterers in the tissue, as it has been previously observed in laser speckle [14, 99] and laser doppler measurements of blood flow [100].

Figure 3.16 shows typical images of the rCBF obtained during the study at each time point of the protocol, for one animal from each of the two groups under study. This maps allow to have a general overview about what happens with the flow during the time course of the experiment. During occlusion it is possible to see a deep decrease in flow in the ipsilateral hemisphere of both animals. After reperfusion it is possible to see how the CBF flow in that hemisphere is recovered in the MBL-KO animal while in the WT mouse the hemisphere continued with a lower flow with respect to the baseline.

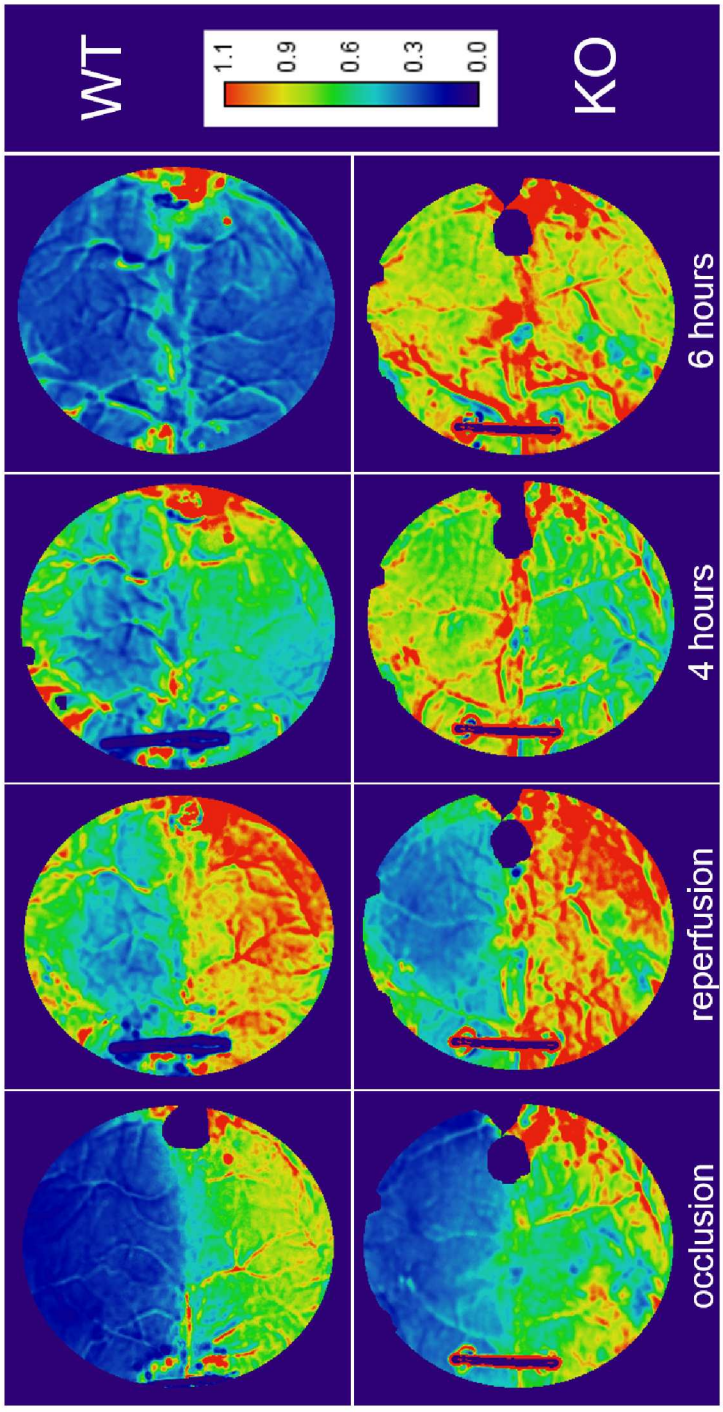

Figure 3.16: The rCBF maps at occlusion and at 1, 4, and 6 hours from reperfusion with respect to the baseline for one WT and one MBL-KO mouse. A rCBF=1 indicates no change of blood flow with respect to the basal flow. Images in false color.

For a more quantitative analysis of the results and to establish if there is a real difference in the CBF after reperfusion related to the MBL protein, the ROI calculation was performed for each animal (ischemic: n=5 per genotype and sham: n=3 per genotype) and a statistical analysis was performed. This analysis consisted on a two-way ANOVA for comparisons of genotype, brain hemisphere or time. The results for each of the defined ROIs in the ischemic animals are summarized in Figure 3.17. In each graph, the $rCBF_{base}$ is presented over time. The x-axis corresponds to hours of the experiment. The time 0 for the experiment is considered to be the reperfusion time. Hence, negative hours correspond to baseline and occlusion (-2, -1 hours) and the positive hours correspond to the hours after the reperfusion.

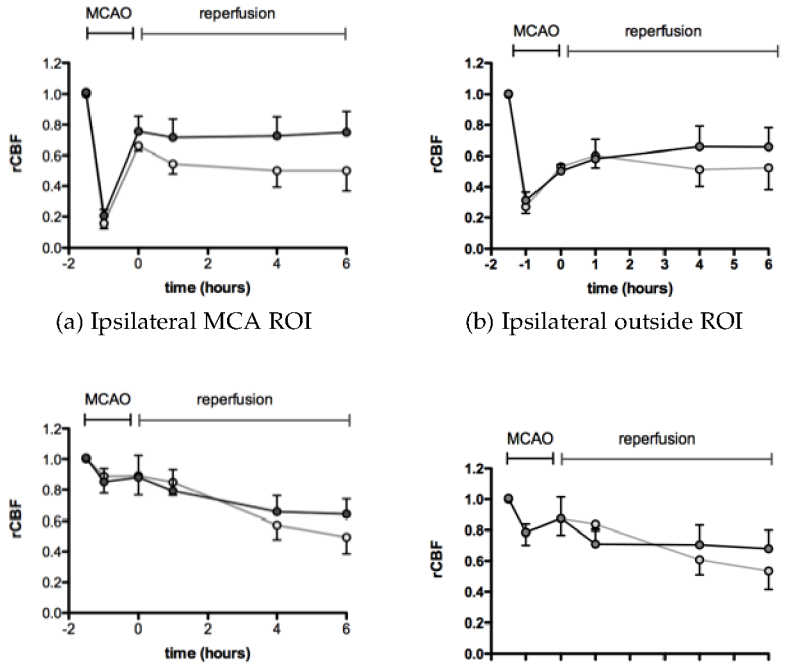

(a) Ipsilateral MCA ROI

(b) Ipsilateral outside ROI

(c) Contralateral MCA ROI

(d) Contralateral outside ROI

Figure 3.17: rCBF over time for the two animal groups. Reproduced with permission from Stroke: 27 March 2014 - volume 45 - number 5 - p 1453-1459, Wolters Kluwer Health Lippincott Williams & Wilkins©

According to the laser doppler measurements of CBF measured during the first 30 minutes after the occlusion, the rCBF was $15.0 \pm 6.1\%$ in the WT group and $16.4 \pm 6.3\%$ in the MBL-KO group. Here the two-way ANOVA resulted in a P value of 0.73, meaning that the decrease of flow during the occlusion can be considered equal for both groups. From the LSF results at the occlusion in the ipsilateral MCA ROI (Figure 3.17a), the obtained values of rCBF compared to baseline were $10.8 \pm 4.7\%$ in the WT group and $17.0 \pm 10.5.3\%$ in the MBL-KO group. In this case, P=0.27, which gives the same conclusion. At the time of reperfusion, it is seen that the rCBF from the two animal groups was recovered to a very similar value, but as the time from reperfusion progressed, the rCBF decreased in the WT group but not in the MBL-KO group (Figure 3.17a). To analyse this effect, a two-way ANOVA by genotype and time was performed showing a significant genotype effect, $P < 0.05$, meaning that in fact there is a difference in rCBF after reperfusion coming from differences in the animal groups. In contrast to this finding in the ipsilateral MCA ROI, for the ipsilateral ouside ROI and both ROIs in the contralateral hemisphere, the rCBF was similar for both animal groups. However, the results in the contralateral hemisphere showed a reduction of CBF after ischemia for the WT animals (Figure 3.17c and 3.17d), which is in accordance with previous findings [101] and might be caused by a decrease in contralateral activity due to depressed transcallosal neural connections[95].

The results for the sham operated animals is presented in Figure 3.18 an in general, for all, the ROIs, there was not an appreciable difference in rCBF regarding the animals genotype and the rCBF was very stable over time. The latter suggests that there is not a visible effect of the anesthesia over the course of the experiment despite the long-time exposure of the animals to it and that is not the cause of the differences between genotypes observed in the ischemic animals.

Also, in order to discard differences in the cerebral anatomy between animal groups, that could be the cause of the differences observed in the ischemic mice, carbon black ink was perfused in control mice of both genotypes (n=3). The results from visual inspection of the *ex vivo* brains and quantification of the anastomoses (connections) between the MCA and the ACA (anterior carothid

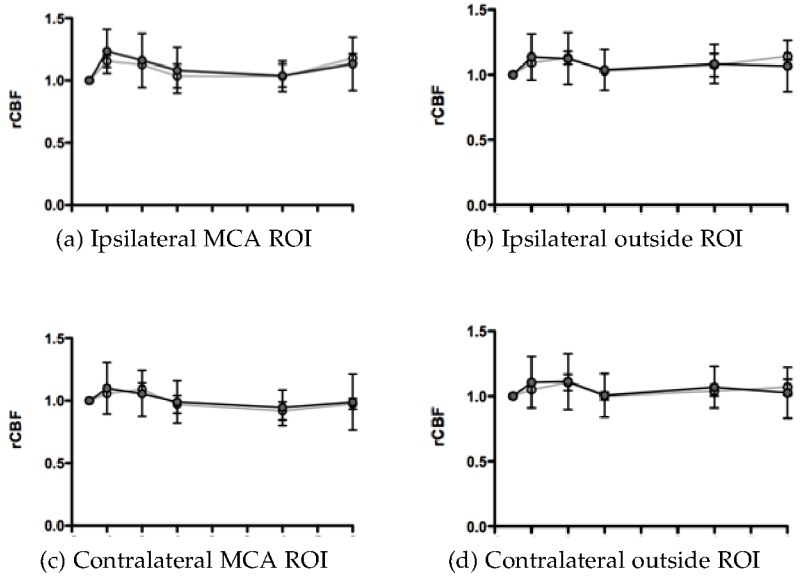

(a) Ipsilateral MCA ROI (b) Ipsilateral outside ROI

(c) Contralateral MCA ROI (d) Contralateral outside ROI

Figure 3.18: rCBF over time for the two animal groups. Reproduced with permission fromStroke: 27 March 2014 - volume 45 - number 5 - p 1453-1459, Wolters Kluwer Health Lippincott Williams & Wilkins©.

arthery) showed that in fact there is not genotype dependent differences [95].

3.4.4 *Optical Intrinsic Signal Imaging*

The analysis for the OIS data was performed using the same ROI's defined for the analysis of the LSF data (Figure 3.15). The molar extinction coefficients, ϵ, where obtained from Scott Prahl's webpage[2]. The differential pathlengths, obtained by Monte Carlo calculations, were kindly supplied by Wesley Baker from the University of Pennsylvania.

In order to calculate the changes in concentration of the blood chromophores, i. e., oxygenated hemoglobin and deoxygenated hemoglobin, we used three of the wavelengths available in the device: 525 nm, 590 nm and 635 nm and solved the matrix system in Equation 2.12. We corrected the changes in absorption by weighing them by the contribution of each wavelength available in the optical spectrum of the corresponding LED.

For the calculation of the total hemoglobin concentration, we assumed an initial concentration of oxygenated hemoglobin and deoxygenated hemoglobin of 60 µM and 40 µM respectively [81].
Figure 3.19 summarizes the results from the OIS measurements for the four ROIs defined for the analysis. Each region presents the evolution over time for the ischemic as well as the sham operated animals in both groups included in the study. It is possible to observe that the results obtained for the total hemoblobin concentration along the hours following the reperfusion, resemble the results obtained for the CBF, in particular for the ipsilateral MCA region (Figure 3.17) where the WT ischemic animals show a reduced total hemoglobin concentration at 6 hours from the occlusion in comparison to the MBL-KO animals.

2 Tabulated Molar Extinction Coefficient for Hemoglobin in Water, http://omlc.ogi.edu/spectra/hemoglobin/summary.html [Accessed 27 October 2014]

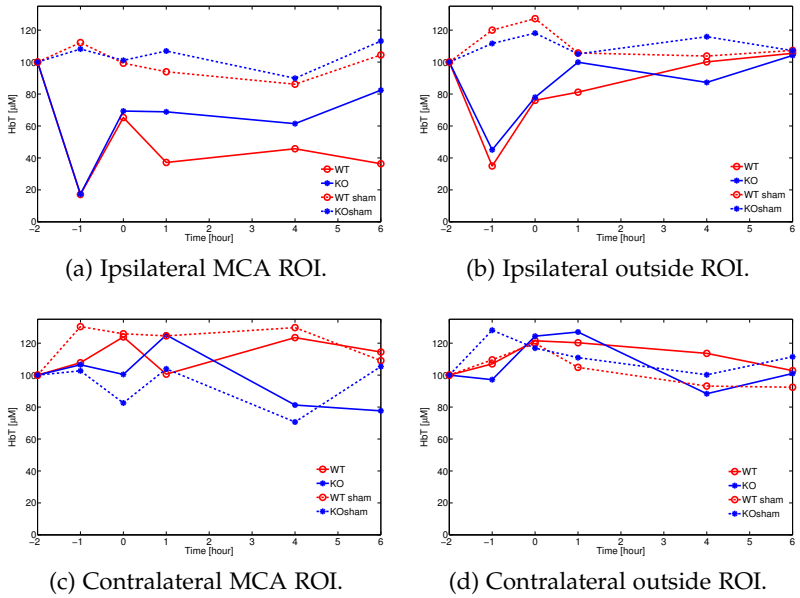

(a) Ipsilateral MCA ROI.

(b) Ipsilateral outside ROI.

(c) Contralateral MCA ROI.

(d) Contralateral outside ROI.

Figure 3.19: Total hemoglobin changes over time for ischemic (solid line) and sham animals (dashed lines) from the groups under study.

3.4.5 *Conclusions*

In this chapter it has been presented the instrumentation, validation and application of a LSF-OIS multimodal device for studies in small animal models. It has been shown that the developed LSF-OIS system is capable of monitoring cerebral blood flow changes and blood oxygenation in mice. Its feasibility in longitudinal studies in which the animal has to be repositioned several timed during the measurement protocol was also presented. This was possible due to the experimental methods developed to enhance the co-registration and intensity renormalization of the images from different time points, i. e., the fiducial markers, the teflon ring, the real-time registration and the post-processing methods.

This device was utilized in a collaborative study with the department of Brain Ischemia and Neurodegeneration at the Institute for Biomedical Research in Barcelona (IIBB), in which the role of the

Mannose-binding lectin (MBL) protein after the reperfusion following a temporal middle cerebral artery occlusion (tMCAO) was examinated. The results obtained with the LSF device contributed to the validation of the hypothesis in which the animals lacking of MBL protein where less affected by reperfusion after an ischemic stroke, due to the fact that coagulation, and hence, reduction in flow was not promoted by MBL activated thrombin.

The results obtained with this device were satisfactory as explained above. Nevertheless, it only gives surface information and it would be desirable to have an optical method capable of imaging deeper inside the brain. This is one of the aims of the new method for measuring deep tissue blood flow that will be presented in the following chapter.

4

SPECKLE CONTRAST OPTICAL SPECTROSCOPY AND TOMOGRAPHY (SCOS/SCOT)

Non-invasive, optical imaging of blood flow has many applications in bio-medicine [10, 62, 102, 103]. Several optical approaches for non-invasive, *in vivo* blood flow measurements rely on the statistics of the laser speckles [64]; laser Doppler flowmetry (LDF) uses the frequency broadening [104, 105], diffuse correlation spectroscopy (DCS) [10, 56, 57] uses the light intensity auto-correlation and laser speckle flowmetry (LSF) [106] uses the spatio-temporal blurring of the speckles [1] . A key difference between the methods is their penetration depth. LDF and LSF generally utilize single or few scattering events and therefore probe superficial (<1 mm) tissues whereas DCS uses photon diffusion theory and probes deep tissues up to several centimeters. Here, we present speckle contrast optical spectroscopy (SCOS) which, in a similar fashion to LSF, uses the speckle contrast but with point sources placed at a distance as in DCS, i. e., detecting photons that have undergone multiple scattering. This provides detection of many speckles in parallel but with extended path lengths for deep tissue sampling.

Recently [107], it has been demonstrated in a flow phantom as well as in a human arm that it is possible to measure changes in blood flow by considering it as the inverse of the speckle contrast using one point source illumination and defining detectors at different distances in a CCD camera. This study was further extended [108] to multi-channel deep tissue flowmetry by fiber coupling

1 For completeness, this Chapter re-iterates some of the concepts discussed in previous Chapters.

the camera to the probed sample. However, unlike DCS, this study did not utilize a model based fitting to decouple the effects of absorption and scattering from the dynamics, and, therefore, did not extract a quantitative estimate of blood flow.

The method, SCOS, presented here, merges the advantages of relatively inexpensive detectors with high frame rates that LSF uses and the quantitative deep tissue flow measurement capabilities of DCS. By using an array of two-dimensional (2D) detectors, SCOS has a broad field-of-view in a single-shot. The signal-to-noise ratio (SNR) can be greatly improved by averaging signals from many detectors, in case of a CCD/sCMOS camera up to an order of a million speckles simultaneously. SCOS measurements can be performed in two different ways with equivalent results: one fixing an exposure time and measuring the speckle contrast at different distances from the source and the other measuring at multiple exposure times [109] with a fixed source-detector distance. One can also utilize both methods simultaneously for an even more complete data-set.

Furthermore, we have introduced a three dimensional tomographic imaging method, speckle contrast optical tomography (SCOT), for quantitative three-dimensional reconstruction of deep tissue blood flow heterogeneities. Based on SCOS results, we have developed and tested a physical model (forward model) for the homogeneous blood flow which was then used to construct the Jacobian for tomography by deriving a perturbation equation based on first Born approximation. We have developed the inversion algorithm and demonstrated the feasibility of the technique in tissue simulating liquid phantoms in transmission geometry.

However, when moving SCOS to realistic scenarios, including *in vivo* measurements, the effects of noises from the CCD to the speckle contrast at large distances from the source become critical and need a correction. To solve this, we have developed an approach to account for the noise sources. Such corrections allowed us to increase the distance ranges for which speckle contrast measurements are useful for the spectroscopic as well as for the tomographic approaches.

In section 1, we present the theoretical development of SCOS and the corrections done to the speckle contrast measurements to account for the shot noise and the noises introduced by the detector. In section 2, the derivation of the sensitivity relation for the SCOT based on Born approximation is presented. The inversion algorithm for SCOT based on the derived sensitivity relation is also presented. Following the theoretical background for SCOS and SCOT, the general experimental methods and procedures to perform measurements with SCOS and SCOT are described. In Section 4.3.3, a series of experiments in liquid tissue simulating phantoms are shown to illustrate the feasibility of SCOS. The first experiment in transmission geometry used the speckle contrast dependence on distance from a point source and allowed the first demonstration of SCOT when a flow heterogeneity was included and reconstructed. We present another SCOS experiment in re-emission geometry, with the dependence on exposure time at a fixed source-detector separation. We further present the extension of the re-emission geometry to an *in vivo* experiment in the human forearm muscle, showing the feasibility of both multiple source-detector separation and multiple exposure measurements from a single source-detector separation. Finally, in section 5, we discuss the results, compare SCOS to LSF, LDF and DCS, and SCOT to DCT and outline the advantages and disadvantages of the methods and suggest future improvements.

The following sections closely follow our published work [75, 110] while expanding on methodological points.

4.1 SPECKLE CONTRAST OPTICAL SPECTROSCOPY(SCOS)

SCOS uses the speckle contrast (κ) measurement, defined as the ratio of the standard deviation (σ_I) of the measured intensity in a given exposure time to its mean (μ_I) value over different speckles in space or time (Equation 2.52), i. e.,

$$\kappa = \sigma_I/\mu_I. \tag{4.1}$$

In LSF, single scattering approximations and uniform illumination of the sample of interest are utilized relating κ to blood flow at

superficial layers [69, 106, 111]. As presented previously, in Section 2.5.2 (Equation 2.59), the speckle contrast (κ) can be expressed in terms of the normalized field autocorrelation $g_1(\mathbf{r},\tau)$ as [66]:

$$\kappa^2(\mathbf{r},T) = \frac{2\beta}{T}\int_0^T |g_1(\mathbf{r},\tau)|^2 \left(1-\frac{\tau}{T}\right) d\tau \tag{4.2}$$

Nevertheless, in the case of LSF measurements, the normalized field autocorrelation function (g_1) is a negative exponential function (Equation 2.60), representing the scattered field in the single scattering regime for a uniform illumination.

From DCS, it is well known that $G_1(\mathbf{r},\tau)$ obeys the correlation diffusion equation (CDE) [10, 56, 57] (Equation 2.50):

$$\left[\nabla\cdot D(\mathbf{r})\nabla - \nu\mu_a(\mathbf{r}) - \frac{\alpha}{3}\nu\mu_s' k_o^2 \left\langle \Delta r^2(\tau)\right\rangle\right] G_1(\mathbf{r},\tau) = -\nu S_0(\mathbf{r}-\mathbf{r}_0), \tag{4.3}$$

where k_0 is the modulus of propagation vector of light, μ_s' is the reduced scattering coefficient, $D \approx \nu/3\mu_s'$ is the optical diffusion coefficient, μ_a is the absorption coefficient, $S_0(\mathbf{r}-\mathbf{r}_0)$ is an isotropic source (point source) located at $\mathbf{r}_0$ and ν is the velocity of light in the turbid medium. $\left\langle \Delta r^2(\tau)\right\rangle$ is the mean-square displacement (MSD) of the moving scatterers, i.e. red blood cells in case of tissues, in delay time τ. α is the ratio of moving scatterers to the total number of scatterers in the sample which estimates the fraction of photon scattering events from moving scatterers.

In most work on living tissues and on liquid phantoms, the mean square displacement, $\langle \Delta r^2(\tau)\rangle$, is assumed to be equal to $6D_B\tau$, where D_B is the particle diffusion coefficient. This has been tested extensively in DCS experiments on living tissues [10] and was found to follow a Brownian diffusion model where an "effective" αD_B corresponds to a blood flow index (BFI). Typical normalized field autocorrelation functions as a function of correlation time (τ) for three different source detector separations ($\mathbf{r}$) are plotted in Figure 4.1(a) using the analytical Green's function formula given in Equation 2.51. The corresponding speckle contrast as function of source-detector separation and exposure time are computed using Equation 4.2 and are plotted in Figure 4.1(b) and Fig-

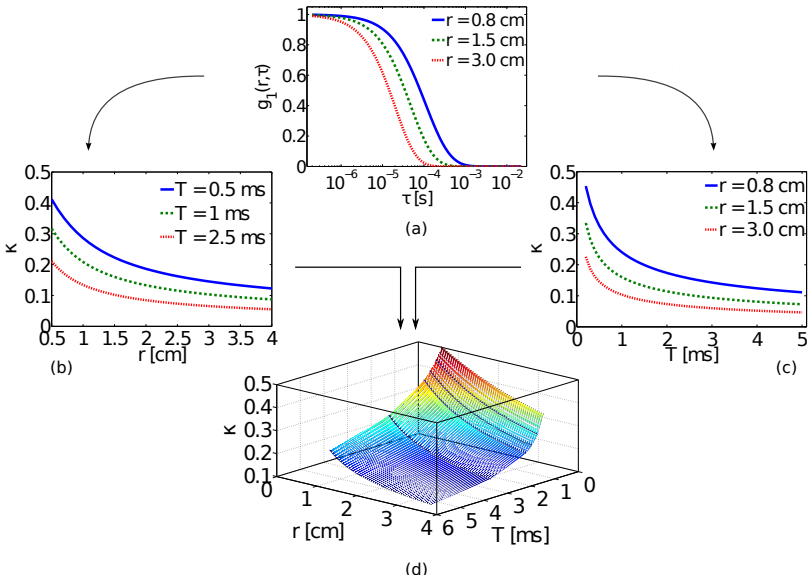

Figure 4.1: Normalized field auto-correlation function for three different source-detector separations is calculated using Equation 2.51 in panel (a). The dependence of the speckle contrast derived from Equation 4.2 on (b) source-detector separation and (c) exposure time for a point source are also shown. The combined result can be viewed (d) as a surface plot of the speckle contrast dependence on both distance and exposure time. Here $\mu_s' = 10\ \mathrm{cm}^{-1}$, $\mu_a = 0.1\ \mathrm{cm}^{-1}$, $D_B = 1 \times 10^{-8}\ \mathrm{cm}^2/\mathrm{s}$. Figure reproduced from [110].

ure 4.1(c) respectively. The surface plot of speckle contrast as function of both $\mathbf{r}$ and T is shown in Figure 4.1(d) which depicts the complete set of theoretical data that is available in SCOS for measuring the blood flow. In the following section we will describe the extent to which the above-said plots deviates from their theoretical values due to presence of shot noise and detector/sensor specific noise, i.e. CCD or scientific complementary metal-oxide-semiconductor (sCMOS), and the necessary steps to be taken to overcome it.

4.1.1 *Noise corrections*

In practice, it is critical that the calculations of speckle contrast derived from experimental measurements take into account the contributions to κ due to shot noise and different types of noise due to the specific detection system. Since κ depends on the variance of the observed signal, unless these systematic effects are accounted for, the speckle contrast will deviate from its theoretical behaviour. This is specially visible in regions where SNR is lower, as will be presented in detail for the *in vivo* experiments presented in Section 4.4.2.

The raw intensity images are initially corrected for the dark counts before computing the speckle contrast. A mean dark image, μ_{I_D}, is obtained by taking the mean of several dark frames, I_D. From each raw intensity image, I, the μ_{I_D} is subtracted which gives the dark subtracted images denoted as:

$$I_c = I - \mu_{I_D}. \tag{4.4}$$

The speckle contrast is then defined as the ratio of the standard-deviation over different speckles separated in space or time, $\sigma(I_c)$, to their mean, $\mu(I_c)$. Here the dark subtraction will, in fact, remove the contribution of the mean dark counts from the $\mu(I_c)$ because $\mu(I_c) = \mu(I) - \mu_{I_D}$ but the variance of the mean dark counts will be added to the variance of the raw intensity images due to the fact that $\sigma^2(I_c) = \sigma^2(I) + \sigma^2(\mu_{I_D})$. This observation leads us to conclude that subtracting the mean dark image from the raw image does not help to remove the noise (variance) associated with the dark image. Hence, we use a dark variance correction (σ_d^2) to remove the dark noise variance from the variance of raw intensity images. This parameter contains different sources of noise including the readout noise. The mean dark variance, $\sigma_d^2 = \mu(\sigma^2(I_D))$, is the mean of variances computed from several dark frames (see Section 4.3.1.4 for details). Note that the above observations are applicable to intensity images expressed in both electrons and digital counts.

Another, often more significant, noise source is the inherent shot-noise which obeys the Poisson statistics with a variance equal

to the mean, i.e., $\sigma_s^2 = \mu(I_c)$ in electrons $[e^-]$. The speckle contrast purely due to shot-noise can be written as $\kappa_s = 1/\sqrt{\gamma I_c}$ [112], where γ is the ratio of full well capacity of a CCD/sCMOS camera to its analog-to-digital conversion bits. In other words, we convert the counts into electrons $[e^-]$. The shot-noise corrected speckle contrast is then defined as [112]:

$$\kappa_{sc} = (\kappa^2 - \kappa_s^2)^{1/2} \, . \tag{4.5}$$

Finally, combining the dark correction and shot noise correction we have the corrected speckle contrast (κ_c) as

$$\kappa_c = \sqrt{\frac{(\sigma(I_c)^2 - \sigma_s^2 - \sigma_d^2)}{\mu(I_c)^2}} \, . \tag{4.6}$$

Here all the variances and the mean are computed from the intensity images in electrons units which are obtained by multiplying the intensity images in digital units with γ. The effect of the corrections explained here is illustrated in Figure 4.27 using the data from a SCOS *in vivo* experiment. There, the variances involved in each correction are plotted with respect to the S-D and the intensity that the camera detects at that distance from the source.

4.1.2 *Fitting Procedure*

In all experiments, a non-linear least squares fit is carried out assuming known, independently measured, optical properties of the probed medium to obtain a D_B value corresponding to a blood flow index in tissues. The fit uses the appropriate Green's function (Equation 2.51) as the solution of the correlation diffusion equation (Equation 4.3) and relates the model to the speckle contrast versus source-detector separation (S-D separation) and/or exposure time using Equation 4.2. Since the instrumental/optical constant, β, was not measured accurately, we normalize both the measured and calculated speckle contrast by its mean.

4.2 SPECKLE CONTRAST OPTICAL TOMOGRAPHY (SCOT)

4.2.1 *Born approximation for SCOT.*

In order to be able to carry out tomography, we should first develop the inverse imaging problem where the 3D distribution of MSD, $\Delta r^2(\tau)$, inside the volume of interest is recovered from the measurement of the two dimensional distribution of intensity speckle contrast, κ, at the surface using the CDE in Equation 4.3.

We derived the linear Born approximation [70, 71, 113] to reconstruct $\Delta r^2(\tau)$ from κ as explained below. In the future, this could readily be extended to other perturbation methods and non-linear approaches[70, 71, 72].

For simplicity, we adopt the following notations: $C_0 = \frac{1}{3}\mu_s' k_0^2$, $C_b = 2\mu_s' k_0^2 \tau$ and $C_v = \frac{1}{3}\mu_s' k_0^2 \tau^2$. We first consider the homogeneous solution $G_1^0(\mathbf{r}, \tau)$ which solves Equation 4.3 with $\Delta r^2(\tau) = \Delta r^2(\tau)^0$ where $\Delta r^2(\tau)^0 = 6D_B^0\tau + (V^2)^0\tau^2$ is the baseline MSD. Due to the presence of a perturbation in MSD by an amount $\Delta r^2(\tau)^\delta = 6D_B^\delta\tau + (V^2)^\delta\tau^2$ the $G_1^0(\mathbf{r}, \tau)$ will get perturbed by an amount G_{sc}, resulting in perturbed field correlation $G_1(\mathbf{r}, \tau) = G_1^0(\mathbf{r}, \tau) + G_{sc}(\mathbf{r}, \tau)$. Here $G_1(\mathbf{r}, \tau)$ can be obtained by solving Equation 4.3 with MSD $\Delta r^2(\tau) = \Delta r^2(\tau)^0 + \Delta r^2(\tau)^\delta$.

Substituting the above expression for G_1 in Equation 4.3, and subtracting Equation 4.3 from the resulting equation, an expression for G_{sc} can be written as,

$$\begin{aligned} &G_{sc}(\mathbf{r}_d, \mathbf{r}_s, \tau) \\ &= -C_0 \int_\Omega G(\mathbf{r}', \mathbf{r}_d, \tau) \left(G_1^0(\mathbf{r}', \mathbf{r}_s, \tau) + G_{sc}(\mathbf{r}', \mathbf{r}_s, \tau) \right) \Delta r^2(\tau)^\delta d\mathbf{r}'. \end{aligned} \tag{4.7}$$

Here $G(\mathbf{r}', \mathbf{r}_d, \tau)$ is the Green's function for the operator given by Equation 4.3 with $\Delta r^2(\tau)^\delta = 0$.

The first Born approximation states that scattered field G_{sc} is negligibly small compared to the background (homogeneous) field G_1^0, i.e., $G_{sc} << G_1^0$, and hence the above nonlinear integral equation reduces to a linear integral equation in G_{sc} given by

$$G_{sc}(\mathbf{r}_d, \mathbf{r}_s, \tau) = -\left(C_b \int_\Omega G(\mathbf{r}', \mathbf{r}_d, \tau) G_1^0(\mathbf{r}', \mathbf{r}_s, \tau) D_B^\delta \, d\mathbf{r}' + C_v \int_\Omega G(\mathbf{r}', \mathbf{r}_d, \tau) G_1^0(\mathbf{r}', \mathbf{r}_s, \tau) (V^2)^\delta \, d\mathbf{r}' \right). \tag{4.8}$$

Since κ depends on the normalized field autocorrelation $g_1(\tau)$, in order to compute the perturbations in measurement due to flow term V_b, we divide the expression $G_1(\mathbf{r}, \tau) = G_1^0(\mathbf{r}, \tau) + G_{sc}(\mathbf{r}, \tau)$ by $G_1(\mathbf{r}, 0)$ on both sides resulting in

$$\frac{G_1(\mathbf{r}, \tau)}{G_1(\mathbf{r}, 0)} = \frac{G_1^0(\mathbf{r}, \tau)}{G_1(\mathbf{r}, 0)} + \frac{G_{sc}(\mathbf{r}, \tau)}{G_1(\mathbf{r}, 0)}, \tag{4.9}$$

which gives

$$\frac{G_1(\mathbf{r}, \tau)}{G_1(\mathbf{r}, 0)} = \frac{G_1^0(\mathbf{r}, \tau)}{G_1^0(\mathbf{r}, 0)} \frac{G_1^0(\mathbf{r}, 0)}{G_1(\mathbf{r}, 0)} + \frac{G_{sc}(\mathbf{r}, \tau)}{G_1(\mathbf{r}, 0)}. \tag{4.10}$$

When $\tau = 0$, $G_{sc} = 0$ and hence $G_1^0(\mathbf{r}, 0) = G_1(\mathbf{r}, 0)$ which implies

$$g_1(\mathbf{r}, \tau) = g_1^0(\mathbf{r}, \tau) + \frac{G_{sc}(\mathbf{r}, \tau)}{G_1(\mathbf{r}, 0)}. \tag{4.11}$$

Hence, the measurement κ corresponding to the inhomogeneous normalized field autocorrelation g_1 under perturbations due to flow is given by

$$\kappa^2(\mathbf{r}, T) = \frac{2\beta}{T} \int_0^T \left[g_1^0(\mathbf{r}, \tau) + \frac{G_{sc}(\mathbf{r}, \tau)}{G_1(\mathbf{r}, 0)} \right]^2 \left(1 - \frac{\tau}{T} \right) d\tau$$

$$= \frac{2\beta}{T} \int_0^T \left[(g_1^0(\mathbf{r}, \tau)^2 + 2 g_1^0(\mathbf{r}, \tau) \frac{G_{sc}(\mathbf{r}, \tau)}{G_1(\mathbf{r}, 0)} + \left(\frac{G_{sc}(\mathbf{r}, \tau)}{G_1(\mathbf{r}, 0)} \right)^2 \right] \left(1 - \frac{\tau}{T} \right) d\tau.$$

In order to simplify the above expression, the condition for first Born approximation ($G_{sc} << G_1^0$) is again invoked resulting in

$$
\begin{aligned}
g_1^0(\mathbf{r},\tau)^2 + \left(\frac{G_{sc}(\mathbf{r},\tau)}{G_1(\mathbf{r},0)}\right)^2 &= \left[\frac{G_1^0(\mathbf{r},\tau)}{G_1^0(\mathbf{r},0)}\right]^2 + \left[\frac{G_{sc}(\mathbf{r},\tau)}{G_1(\mathbf{r},0)}\right]^2 \\
&= \frac{G_1^0(\mathbf{r},\tau)^2 + G_{sc}(\mathbf{r},\tau)^2}{G_1^0(\mathbf{r},0)^2} \\
&\approx \frac{G_1^0(\mathbf{r},\tau)^2}{G_1^0(\mathbf{r},0)^2} \\
&= g_1^0(\mathbf{r},\tau)^2.
\end{aligned} \tag{4.12}
$$

Therefore, the expression for κ reduces to

$$
\begin{aligned}
\kappa^2(\mathbf{r},T) = \frac{2\beta}{T}\int_0^T g_1^0(\mathbf{r},\tau)^2\left(1-\frac{\tau}{T}\right) + \\
\frac{4\beta}{T}\int_0^T \left(1-\frac{\tau}{T}\right) g_1^0(\mathbf{r},\tau)\frac{G_{sc}(\mathbf{r},\tau)}{G_1(\mathbf{r},0)}.
\end{aligned} \tag{4.13}
$$

By defining the baseline speckle contrast as $\kappa_0^2 \equiv \frac{2\beta}{T}\int_0^T g_1^0(\mathbf{r},\tau)^2(1-\frac{\tau}{T})$ and $\Delta\kappa^2 \equiv \kappa^2 - \kappa_0^2$, we proceed to write the change in speckle contrast due the perturbation in MSD $\Delta r^2(\tau)^\delta$ as

$$
\begin{aligned}
&\Delta\kappa^2 = \\
&-\frac{4\beta}{T}\int_0^T \left(1-\frac{\tau}{T}\right)\frac{g_1^0(\mathbf{r},\tau)}{G_1(\mathbf{r},0)}\left[C_b\int_\Omega G(\mathbf{r}',\mathbf{r}_d,\tau)G_1^0(\mathbf{r}',\mathbf{r}_s,\tau)D_B^\delta\, d\mathbf{r}'\right. \\
&\left.+C_v\int_\Omega G(\mathbf{r}',\mathbf{r}_d,\tau)G_1^0(\mathbf{r}',\mathbf{r}_s,\tau)(V^2)^\delta\, d\mathbf{r}'\right] d\tau.
\end{aligned} \tag{4.14}
$$

Here κ_0 is the baseline speckle contrast measured without any perturbation in MSD i.e., when $\Delta r^2(\tau)^\delta = 0$. We consider a special case of the above sensitivity relation with $D_B^\delta = 0$ and $(V^2)^0 = 0$ i.e., there is no perturbation in Brownian motion and the perturbation to the system is introduced as a deterministic flow represented by V^2. We note that the impression of the blood flow in living tissues on the measured quantity is better modelled as $\Delta r^2(\tau) = D_B\tau$. Here we have adopted a flow imaging experiment which uses $\Delta r^2(\tau) = V^2\tau^2$. The sensitivity relation in Equation 4.14 can be employed for living tissue by setting $V = 0$ and

$(V^2)^\delta = 0$ and considering D_B^0 as the baseline flow with D_B^δ as the perturbation in flow from the baseline value. The estimation of errors associated with the Born's approximation in the context of DOT is addressed in [114] which can be used to estimate the errors for the results presented here, but it is beyond the scope of this work.

4.2.2 *Inversion Algorithm*

The computation of the sensitivity relation (Equation 4.14) is done in a discretized slab geometry which corresponds to the size of the object to be imaged in the experiment as well as the scanning pattern of the source relative to detector positions. The computational domain is a rectangular slab of size $N_x \times N_y \times N_z$ as shown in Figure 4.2.

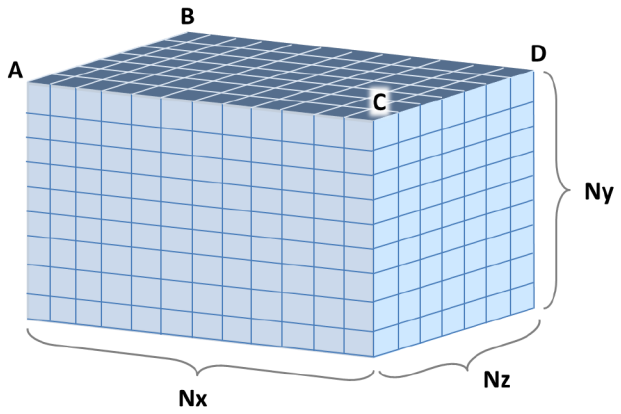

Figure 4.2: Three dimensional geometry depicting the computation domain of the SCOT reconstruction.

The first part of the computational algorithm involves the calculation of the speckle contrast from experimentally measured raw intensity images and the determination of the X-Y coordinates of sources from the same images by the calculation of its centre of mass and the help of a Canny edge detecting algorithm (please refer to Section 4.3.1.2. For each of the N_s sources, we have used N_d detectors localized in the detector plane ABCD.

The coordinates (X,Y,Z) were discretized into v_x, v_y and v_z points respectively, which gives a total of $v_x \times v_y \times v_z$ voxels for the three dimensional slab geometry. The baseline speckle contrast (κ_0) corresponding to the D_B^0, is computed using the semi-infinite Green's function solution of CDE in Equation 2.50. The term in left hand side of the Equation 4.14, which is the perturbation in speckle contrast due to the flow relative to its baseline value ($E = \Delta\kappa^2$), is computed by subtracting the baseline speckle contrast from the speckle contrast computed from intensity images measured in the presence of flow. The right hand side term in Equation 4.14 is computed using the rectangular geometry with $N_V = v_x \times v_y \times v_z$ voxels and for $N_s \times N_d$ source-detector pairs which gives the Jacobian matrix (J) of size $(N_s \times N_d) \times N_V$.

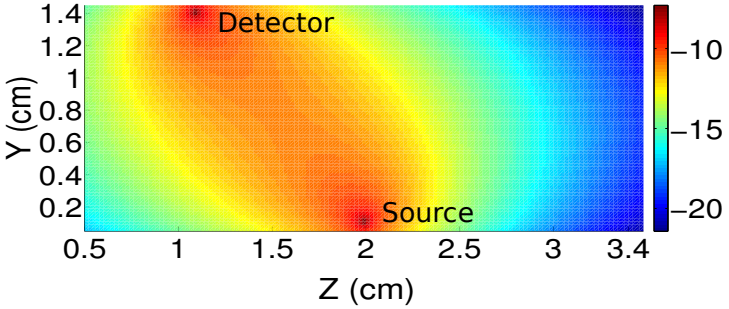

Figure 4.3: The Jacobian (in logarithmic scale) given in Equation 4.14 computed for a given source detector pair in a three dimensional grid. Figure reproduced from [75].

In order to demonstrate that the so-called banana path of photon propagation is still preserved for the derived Jacobian, in the special case that is considered, we computed the right hand side of the sensitivity relation in Equation 4.14 in the three dimensional discretized grid (Figure 4.2). Here analytic Green's function for semi-infinite geometry with homogeneous distribution of tissue properties is used to compute the Jacobian. But the expression for the Jacobian as given in Equation 4.14 is derived without any assumption on the form of the solution and hence this formalism permits the use of other forward solvers for CDE in Equation 4.3. For a better observation of the Jacobian, in Figure 4.3, the logarithmic of the Jacobian in the YZ plane for X coor-

dinate=1.8 cm for a source and a detector positioned in transmission at $(x, y, z) = (1.8, 0, 2.0)$ cm and $(x, y, z) = (1.8, 1.5, 1.08)$ cm respectively, is presented.

Finally, the Jacobian is normalized to get $\tilde{J} = J \circ B$ where '$\circ$' denotes Hadamard product defined as $(J \circ B)_{i,j} = (J)_{i,j}(B)_{i,j}$ (point wise multiplication). Here B is a matrix of size $(N_s \times N_d) \times N_V$ whose rows are the vector b such that $b_i = \frac{1}{a_i}$ $i = 1...N_v$ and $a = \sqrt{(c^T + \lambda_2 max(c^T))}$ [115, 116]. Here indices in suffix position is used to denote the elements of the matrix, the vector c, of size $N_V \times 1$, is the sum of rows of the Jacobian and 'T' notates the transpose of the matrix.

In the discretized domain, Equation 4.14 can be re-casted in terms of the normalized Jacobian $\tilde{J}$ which gives

$$(V^2)^{\delta} = B^T \circ \tilde{J}^T(\tilde{J}^T\tilde{J} + \lambda I)^{-1}\Delta\kappa^2 \tag{4.15}$$

where, due to the ill-posedness of the system of equation, we have used $\lambda = \lambda_1 max(diag(S))$. Here S is the diagonal matrix obtained using the singular value decomposition of the matrix $\tilde{J}$. The flow velocity is computed by solving the linear system of regularized discrete sensitivity equations given in Equation 4.15. The same treatment would be valid for the reconstruction of D_B by replacing V^2 by D_B in Equation 4.15.

4.3 EXPERIMENTAL METHODS

Optical spectroscopy is performed using different geometries depending on the configuration of the light source and detector with respect to the sample. The two basic configurations are the *transmission* and the *re-emission* geometries. In the transmission geometry, the sample is illuminated from one side and the detector is located on the other side to collect the light that has traveled through the sample, as shown in Figure 4.4a for the source and the solid colored detector. In the re-emission geometry, the light sources and detectors are positioned along the same surface of the sample so that the collected light is the one that has been re-emitted or back-scattered from the sample, as shown in Figure 4.4b.

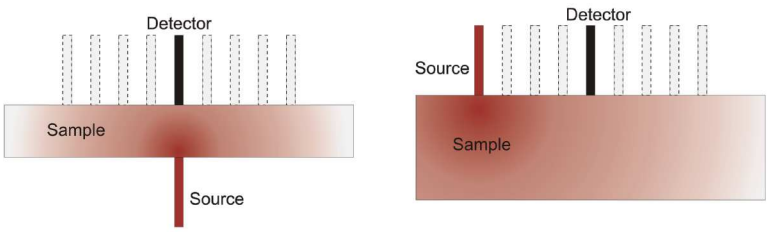

(a) Transmission geometry. (b) Re-emission geometry.

Figure 4.4: Conventional geometries of data acquisition for optical characterization of a medium.

In order to probe the dynamic properties of a sample, it is possible to use the diffuse correlation spectroscopy (DCS) which relies on the diffusion of light by a highly scattering medium. This method consists in illuminating the sample with a laser point source, usually obtained by guiding the light through an optical fiber and measuring the field autocorrelation function at different positions from the source using individual detectors with high temporal resolution. The position of the source and detectors with respect to the medium depends on the application, but, as seen from Figure 4.4a the source is fixed to one position, and the detector is moved to different positions, represented by the dashed lines, to complete the measurements.

With the aim of getting three-dimensional information about the dynamic properties of a medium, a tomographic imaging method, based on the DCS principle, called Diffuse Correlation Tomography DCT could be used. Similar to usual tomographic methods, sample is illuminated at different positions, and for each of these positions represented by red dashed lines in Figure 4.5a, the field autocorrelation function has to be measured at all the different detector positions represented by black dashed lines. In this case, a large number of sources and detectors is needed with the objective of reconstructing inhomogenous variations in dynamics of the medium, represented by the blue circle in the sample.

Based on the laser speckle flowmetry (LSF) experimental array, in which the sample is uniformly illuminated and the speckle pat-

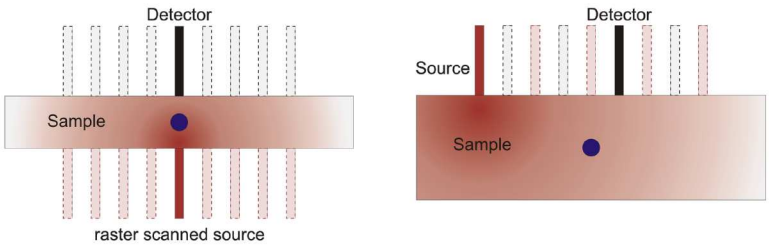

(a) Transmission mode. (b) Re-emission mode.

Figure 4.5: Diffuse correlation tomography illumination- detection schematic.

tern is imaged using a CCD/sCMOS camera, here we propose a speckle contrast optical spectroscopy (SCOS) method and a speckle contrast optical tomography SCOT methods. While SCOS is employed to characterize the probing medium for its dynamic properties (like the Brownian motion represented by D_B), SCOT is used to reconstruct three dimensional distribution of the flow in a highly scattering medium comparable to those resulting from measurements involving the previously explained methods.

The main differences between DCS/T and SCOS/T methods are based on the type of light sources and detectors used, and the way to achieve the multiple source-detector separations.

Regarding the *sources*, for both methods, it is mandatory to use a focused laser source or a fiber guided laser source that could be modeled as a point source. Also, one essential requirement about laser source is that its coherence length is larger than total mean free path of the photon in the object to be probed.

With respect to the *detectors*, the method takes advantage of those which can be arranged in the shape of a two dimensional array. Each of these individual detectors in the array are the so-called *pixels*. In this group of detectors could be considered charged coupled device (CCD) cameras, scientific complementary metal-oxide-semiconductor (sCMOS) cameras, arrays of photon counting detectors or single photon avalanche diode (SPAD) arrays.

The advantage of employing such 2-D arrays is that they allow simultaneous acquisition of intensity at all the detectors (pixels).

This gives the possibility to detect the intensity fluctuations simultaneously at different positions with the advantage of low cost and high density sampling with respect to the detectors used in the DCS/T techniques and also at rates comparable to the decorrelation time of the medium. This is represented in Figure 4.6, where it is shown how a 2D detector array in SCOS covers all the positions where the individual photon detectors should be located for DCS technique in transmission or reflection geometries. This acquired intensity information allows to calculate speckle contrast values at different distances from the source, which is the measurement that is going to be used to obtain the dynamic properties of the medium. The speckle contrast measured with respect to multiple source-detector separations and exposure times, equips us with two independent sets of datas for SCOS and SCOT, which in turn, enable to determine the D_B separately to check for consistency.

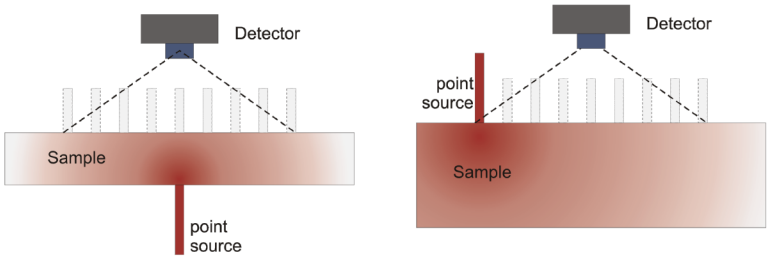

(a) Transmission geometry. (b) Re-emission mode.

Figure 4.6: Schematic of the experimental arrays for the different geometries for SCOS/T.

The design of the SCOT system is based on a laser speckle flowmetry system with an extension to deep tissue tomographic capabilities, using the diffuse correlation tomography (DCT) principles. A focused beam is raster- scanned across the sample from the bottom and the speckle patterns produced by the transmitted light are imaged by a camera at the other side. Each position of the beam is taken as a source and several detectors are defined in the corresponding image for this source. In the end, this provides the sampling needed to do a tomographic reconstruction of the

flow. The SCOT method could be used in both, transmission and reflection geometries as shown in Figure 4.7.

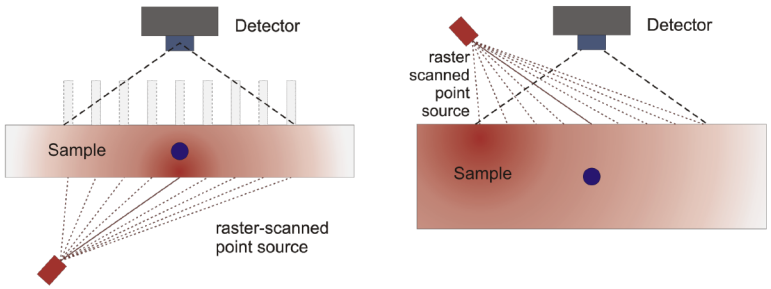

(a) Transmission mode. (b) Re-emission mode.

Figure 4.7: Illumination-detection schematic for the proposed SCOT system in (a) transmission and (b) reflection geometries.

4.3.1 *General Experimental Methods*

In this section we describe the methods that are common to every SCOS/SCOT measurement and that need to be completed, regardless of the particular experimental conditions, e. g., , laser power, exposure time, number of acquired images, frame rate, etc.

4.3.1.1 *Field-of-view Calibration*

Once the SCOS setup has been prepared to image a determined FOV and to have a proper pixel to speckle size ratio, it is necessary to take some reference images that will allow setting distances in the images and localizing the source position.

In every image based method, like the one presented in this work, the size of the object in the image usually differs from its true size. In other words, and particularly here, the distances measured over an image differs from the true distances. This effect depends, on the magnification of the imaging system, which is determined by the objective focal length and the distance to the sample.

With the aim of recovering the true size of an object or to guarantee that the distance measurements performed over the image

corresponds to the reality, a spatial calibration of the images is needed. This process is also known as setting the scale of the image and is performed by putting a reference or a known scale at the same plane of the object and taking an image of it. Each time the FOV is changed, a new *calibration image* has to be taken.

In the SCOS setup the calibration is done by positioning a millimetric ruler coinciding with the plane where the speckles are being imaged, i. e., on top of the sample's surface. A typical calibration image for SCOS, acquired under white light illumination is presented in Figure 4.8a. Once this image is taken, the magnification should be kept constant during the whole measurement.

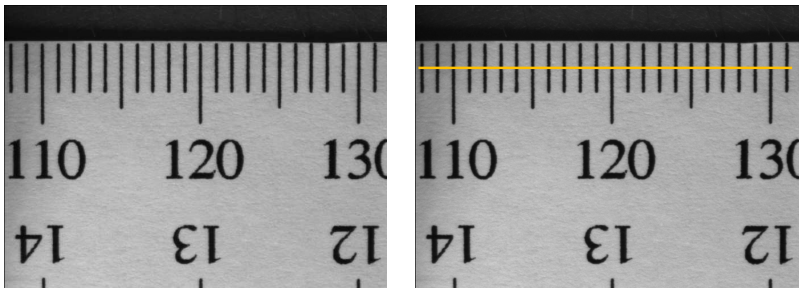

(a) Typical image of a paper scale on the sample's surface to calibrate the FOV.

(b) Line traced to extract the intensity changes on top of the ruler

Figure 4.8: Calibration procedure. Part I.

In an image, the default unit for distances is the pixel (*picture element*), but from the scale in the image it is possible to know how many pixels are within a given distance. This ratio is the *calibration factor* that will allow converting pixels into distance units. The usual procedure to get this factor could be done using a tool available in *fiji* image processing software [88], and consists in tracing a line between two marks of the ruler and counting the pixels in between. This procedure relies on the user's ability to pick the pixels right at the center of the marks and could introduce an error in the calibration of the FOV and the posterior calculation of distances within the image. With the aim of getting a more precise image calibration factor, we used a method, which considers every ruler mark under the drawn line in Figure 4.8b, and not only the start and end point [117]. Then, the intensity of all the pixels included

in that line is plotted as a function of pixel position, as it is shown in Figure 4.9a. In this intensity line profile it is really easy to distinguish the marks of the ruler which appear as intensity minima. The paper ruler we have used here has one mark every 1 mm, and from the image, the pixel position for each mark is known. Then, by plotting the intensity minima position in pixel units, against their position in millimeters, as presented in Figure 4.9b and calculating the slope of the curve we obtain directly the calibration factor for the image in units of pixmm.

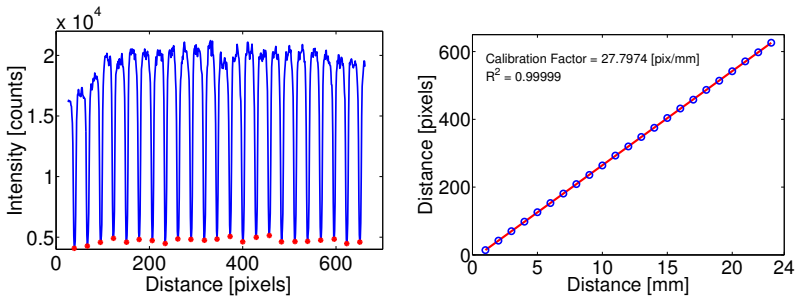

(a) Line profile on the ruler with minima intensity indicated.

(b) Minima from figure (a) plotted against the mm marks of the ruler to get a calibration factor from the slope.

Figure 4.9: Calibration procedure. Part II.

This method has been completely automatized in Matlab. The routine calls the image and the line profile is traced interactively by the user by clicking in two points along the ruler. Afterwards, graphs in Figure 4.9 are generated and saved, the linear fit is done to obtain the calibration factor and it is also saved.

SPECKLE TO PIXEL SIZE RATIO Experimentally, the speckle size in the object plane is calculated dividing the FOV horizontal dimension by the number of horizontal pixels, in the sensor, used to capture an image. In particular, for all the experiments presented here, the speckle size has been calculated to match the pixel size of the detector. This is done by means of the aperture in the objective lens of the system, according to $\rho_{speckle} = 2.44 * \lambda * (1 + M) * f/\#$. Here M is the magnification of the lens and is defined as *image*

size/object size, where the image size corresponds to the detector size.

4.3.1.2 *Source Position Determination and Calculation of S-D Separations*

Due to the fact that SCOS is a method that is completely based on the S-D separations, where the detectors are represented by each pixel in the image, the second compulsory step is to determine the position of the point source with respect to every pixel in the FOV. This procedure varies depending on the geometry in which the measurement is performed, that is, using a transmission or a re-emission geometry, and also will vary if the source is located inside or outside of the FOV.

RE-EMISSION GEOMETRY In a SCOS measurement, the intensity from the point source decays with distance but we are interested on measuring the speckle contrast at large distances from the source while maintaining a high SNR. This could be achieved by increasing the power of the source but, in re-emission geometry, it often causes saturation of the detector at the source location. This saturation may influence the intensity counts in the surrounding pixels causing an error in the overall measurement. To avoid this, the point source was usually localized out of the FOV and the determination of its position involves the procedure described here.

Once the surface of the sample that is being measured is in focus, a paper scale is placed on top of it. This scale should be long enough to cover the source location and the whole *measurement FOV*, that is the FOV imaged for the speckle contrast measurement. First, the camera has to be set to image a FOV that contains the source, which is denoted here as *source FOV*. This *source FOV* has to contain a reference mark that also will be contained in the *measurement FOV*. At this location two images are a acquired. The first will be taken with the laser on and reducing the exposure time as much as possible to get a small source spot that will help determine its coordinates in pixel units from the image. Typically, the exposure time of the camera was set to 50 µs resulting in an image like the one in Figure 4.10a. For the second image, the laser

is blocked and the same FOV is imaged using white light illumination and an exposure time high enough to obtain a good quality image. The resulting image is presented in Figure 4.10b which also points out the reference mark. Afterwards, the camera is moved to image the *measurement FOV* with white light illumination obtaining an image like the one shown in Figure 4.10c that contains the same reference mark.

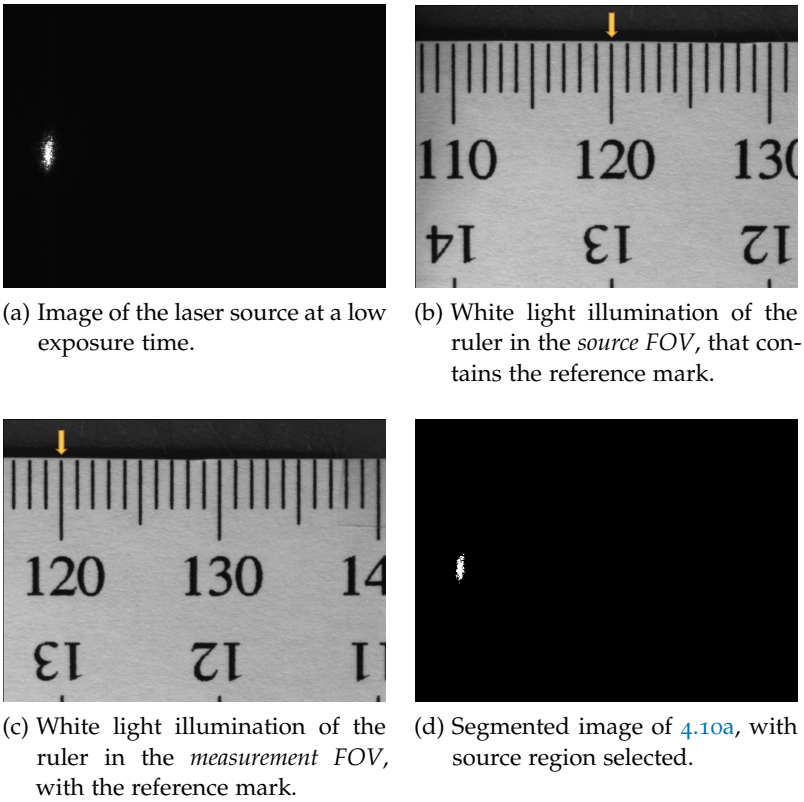

(a) Image of the laser source at a low exposure time.

(b) White light illumination of the ruler in the *source FOV*, that contains the reference mark.

(c) White light illumination of the ruler in the *measurement FOV*, with the reference mark.

(d) Segmented image of 4.10a, with source region selected.

Figure 4.10: Source position determination.

To get the coordinates of the laser source from the image in Figure 4.10a, we used *fiji* software [88]. The first step consisted on segmenting the image to clearly get the region of the image that corresponds to the source. To do this, the image is converted to 8-bits, then we ran a Robust Automatic Threshold Selection (*Plugins> Segmentation>Robust Automatic Threshold Selection*), with the following parameters: noise threshold=25, lambda factor=3, min-

imum leaf size (pixel)=99[2]. This returns an image in black and white like the one in Figure 4.10d, where we used the *Wand (tracing) tool* to select automatically the white region corresponding to the source. Afterwards, we ran a measurement (*Analyze> Measure*) to get the center of mass of the selected region, which in fact gives the coordinates of the source (x_s, y_s) in pixel units after rounding the result.

In order to calculate the S-D separations, in other words, the distances from the source to every pixel in the sensor imaging the *measurement FOV*, the source position is designated as the origin of the coordinate system. This distance calculation involves the use of the Euclidean distance between two points (x_1, y_1) and (x_2, y_2) in the same plane:

$$r = \sqrt{(x_2 - x_1)^2 + (y_2 - y_1)^2} \tag{4.16}$$

Due to the fact that the source is not within the *measurement FOV*, we have to correct the pixel coordinates of this FOV to follow the coordinate system established in the *source FOV*. The first correction is in the horizontal direction and it is done using the reference mark indicated in Figures 4.10b and 4.10c. Again in *fiji*[88], both images are opened and in one of them the reference mark is selected using the Rectangle tool, as seen in Figure 4.11. The center of mass of the selection is calculated retrieving its position in X. Now, the same has to be done in the other FOV but keeping the same size of the selection, which is an action readily available in *fiji*. After copying the selection, it is moved to match the position of the reference mark and the center of mass is calculated. With this procedure, we have the coordinates (x_{FOVs}, y_{FOVs}) and (x_{FOVm}, y_{FOVm}) of the reference mark in the *source FOV* and the *measurement FOV* respectively.

In addition to the translation in X, there could be an unintentional vertical displacement, Δy, of one FOV with respect to the other when the camera is moved to image one field or the other. To have a correction of this vertical displacement, the two FOV

2 These parameters are just indicative for this example and could be changed according to the source picture in each particular experiment.

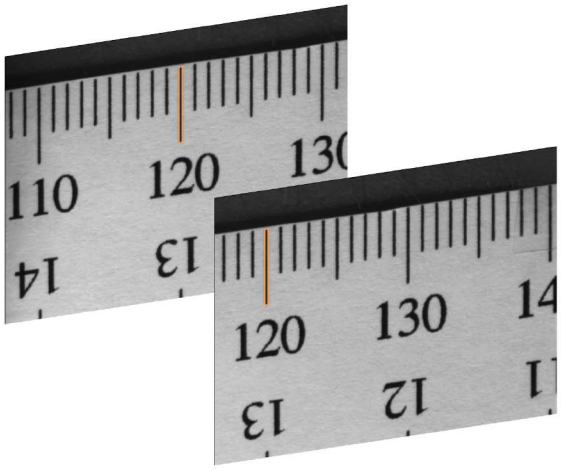

Figure 4.11: Determination of the reference mark position on both the source and the measurement FOVs to obtain the horizontal translation between them.

images are stitched together using the 2D stitching plugin from *fiji*[88] (*Plugins >Stitching>2D Stitching*). The input for this plugin are the images of the two FOVs. Keeping the default parameters in the plugin, the resulting image is presented in Figure 4.12a. Looking closer into the image corners, there is a black region, that is more visible in the detail of the image. The height of the black region corresponds to the pixels that one image is vertical translated with respect to the other, that is the Δy. In Figure 4.12b there is a drawing of how the FOVs are located one with respect to the other in this particular example.

After obtaining the source coordinates, the reference mark x-coordinates in both FOVs and the vertical displacement, it is possible to generalize the calculation of the distances for all the pixels in the *measurement FOV*. Then, for a pixel with coordinates (X, Y), its distance from the source, in pixel units, will be given by:

$$r = \sqrt{(X \pm (x_{FOVs} - x_{FOVm} - x_s))^2 + (Y - (y_s \pm \Delta y))^2} \quad (4.17)$$

In Equation 4.17 there are two $\pm$ signs. The first one accounts for the position of the *source FOV* with respect to the *measurement FOV*. A $+$ is used when the source is located to the left side of the *measurement FOV*, as it is in the images presented here. A $-$

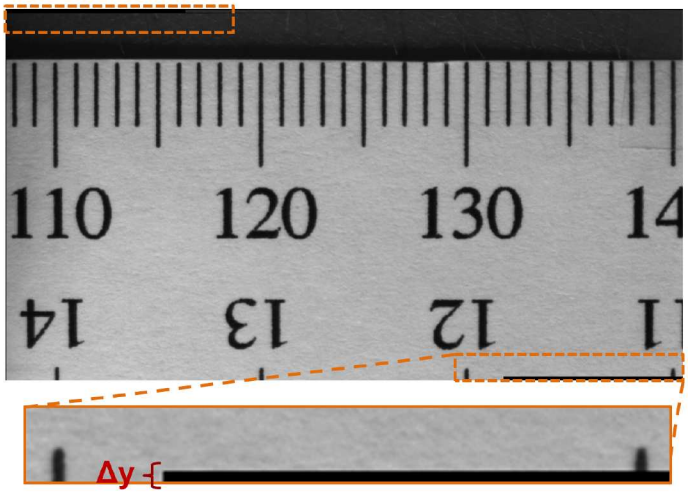

(a) Stitched image from images in Figures 4.10b and 4.10c. The detail shows the vertical translation between the FOVs.

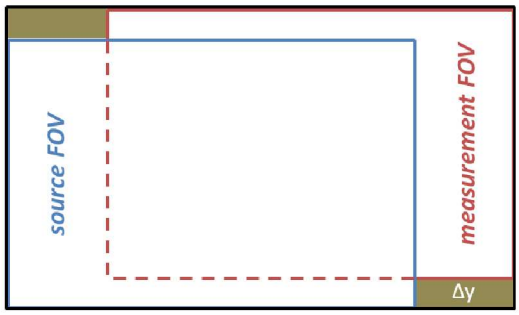

(b) Diagram of the stitched image in 4.12a.

Figure 4.12: Vertical translation correction procedure.

should be use if the source is at the right side. The second $\pm$ sign accounts for the direction of the Δy. The sign should be positive when the *source FOV* appears lower than the *measurement FOV* in the stitched image, the same way it is in the images presented in Figure 4.12. If it is the opposite, being the source FOV higher, a negative sign should be used.

As mentioned before, the s-d distances calculated in Equation 4.17 are given in pixel units. With the aim of converting them to a system of units, it is necessary to divide these distances by the calibration factor obtained before.

When the *source FOV* coincides with the *measurement FOV*, that is, the source appears in the acquired images, the calculation of the distances from the source to a pixel with coordinates (X,Y) is straightforward using Equation 4.16. For this case if the source is saturated, only the pixels at a certain distance from the source are considered. This situation will be present in tomographic measurements in re-emission geometry where the source needs to be scanned along the whole field of view and it might be difficult to avoid the source within the *measurement FOV*.

TRANSMISSION GEOMETRY In the case of measurements done in transmission geometry, usually the source is inside the *measurement FOV* and has no problems with saturation of the sensor because its light intensity has already been reduced after propagating through the medium. For SCOS measurements, the methods to determine the source position have already been described before.

For tomographic measurements in transmission, the source was scanned and the determination of the source positions was automatized. For every image in a full scan, the intensity was thresholded by putting to zero all the pixels with intensity values less than a percent of the maximum intensity in the image, usually 50% to 80%. Afterwards, the center of mass of the image was calculated, being this the position of the source. Figure 4.13 presents an example of the X and Y coordinates of the source position retrieved at every frame in a full scan.

In order to separate the frames corresponding to each source position, we applied a Canny edge detector algorithm[3] [118] to the X coordinates from Figure 4.13. This algorithm calculates the scaled derivatives of the data and finds local maxima or minima that indicate sharp edges in the data. Hence, this algorithm provides the frame number in which the source has moved from one position to the next allowing to calculate an average position for each source in the scanning.

3 Center for Computer Integrated Systems for Microscopy and Manipulation, The University of North Carolina at Chapel Hill, *Edge Detector 1D*, http://www.cs.unc.edu/ nanowork/cismm/download/edgedetector/ [Accessed 2 October 2014]

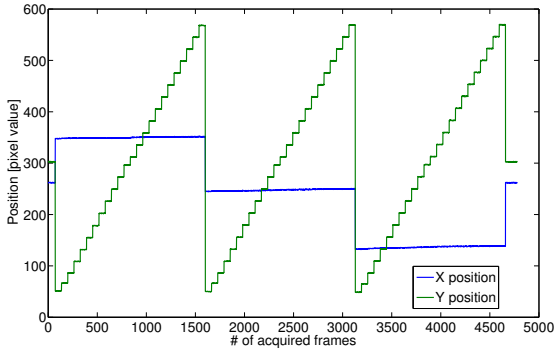

Figure 4.13: Source position retrieved for every frame in a complete source scan. The two graphs represent the position in the X and Y coordinates, showing there are three scans lines with 25 positions in each.

4.3.1.3 *Definition of the Detectors in the Images*

In principle, due to the fact that SCOS/SCOT utilize 2D arrays of detectors, every single pixel could be used as an individual detector, but in order to increase the SNR in the measurements, sometimes it is practical to group some pixels to define larger detector areas.

It has been mentioned before, that a SCOS measurement could be performed by analyzing the dependence of κ with the distance from the source (s-d separation) or with the exposure time, T.

For the first approach, the easiest way to get these dependence would be tracing a line profile, as seen in Figure 4.14a, to have the value of the speckle contrast at every pixel in the line, for which the distance from the source is already known. A second option is to define a detector with a given area, at a given distance from the source, and group all the pixels that fall within the defined area in one detector. This would be the binned detector option presented in Figure 4.14b. Another option is to define rings or arcs depending on whether the source is inside or outside the measurement FOV, as shown in Figure 4.14c. This is interesting because it groups all the pixels that are equidistant to the source in all directions, considering the medium homogeneous.

For the second approach, using the dependence with the exposure time, defining the detectors is done based on the binning

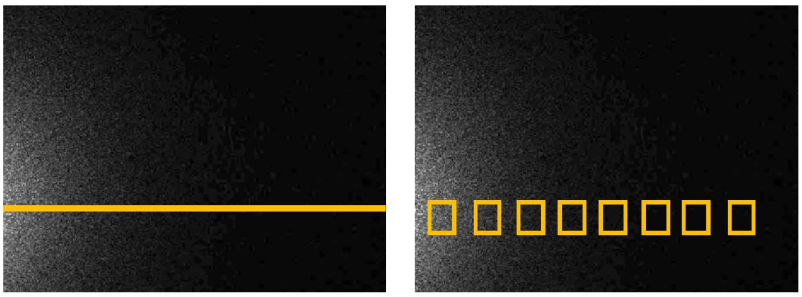

(a) Detectors along a line starting from the source.

(b) Detectors defined by binning pixels within a distance range.

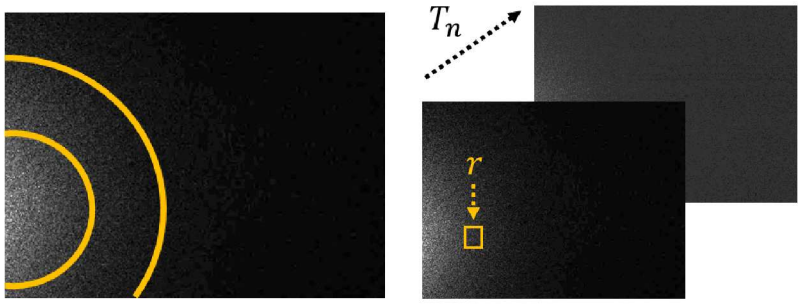

(c) Detectors equidistant from the source.

(d) One detector is fixed at a given distance, r, for every image taken at different exposure times, T.

Figure 4.14: Examples of different geometries to define the detectors for SCOS. (a)- (c) represent options to use the dependence of κ with the distance while (d) represents the procedure to work with the dependence on the exposure time.

method. The key part here is that for one detector at a distance r from the source, there should be various images taken at different exposure times, as represented in Figure 4.14d. Of course, if the sensor is big enough, it is possible to have more than one detector, allowing a simultaneous measurement at more than one s-d separation for the same set of images.

For SCOT, the detectors were defined by binning some pixels and its position was conceived to match the positions of the scanned sources but in the detection plane. However, extradetectors could be added taking advantage of the high number of pixels in the camera sensor.

4.3.1.4 *Speckle Contrast Calculation*

Being SCOS and SCOT speckle contrast based techniques, here we describe the procedures that were applied to the raw intensity images for their conversion into a speckle contrast image.

DARK-FRAME SUBTRACTION When performing a measurement with a camera, it is usual to subtract a dark-frame to every acquired image. This is a well-known procedure typically used in Astronomy to help reducing the background noise from the images e. g., fixed pattern noise from the sensor. Usually, a dark-frame is an image taken with the minimum available exposure time of the camera. For this work, a *mean dark-frame* was obtained from 500 to 1000 dark-frames acquired at the same exposure time used during the measurement. This was done to subtract possible effects induced by any background light, different from the scattered light from the sample. The mean dark-frame was produced by pixel-wise averaging of the intensity over all the dark-frames. This mean dark-frame was subtracted from every intensity acquired image before calculating the speckle contrast as represented in Equation 4.4.

DARK-VARIANCE CALCULATION As mentioned in Section 4.1.1, it is necessary to calculate the variance of the dark in the speckle images. This is done starting from the same set of dark-frames, acquired at the same exposure time that was used to obtain the raw intensity images. The computation of the variance can be done in a pixel basis for all the images to get one variance image. The second method consists on using a sliding window filter, with the size of the window used in the speckle contrast calculation, to calculate the variance on every frame and finally, to get one image representing the dark variance, a mean is done for every pixel over all the dark-frames. This procedure was performed for CCD cameras.

SPECKLE CONTRAST TYPES During this work, three types of speckle contrast calculation are mentioned:

- *Non-corrected speckle contrast*, κ: This makes reference to the calculation of the speckle contrast using the typical speckle

contrast calculation used in LSF (Equation 4.1), without any noise correction. It has been found that the non-corrected speckle contrast will raise to values much higher than one for large distances from the source in which SNR is low.

- *Shot noise corrected speckle contrast*, κ_s: This refers to the speckle contrast calculation including the shot noise correction given by Equation 4.5. This correction was applied for both CCD and sCMOS and extended the usable distance range of the speckle contrast. However, for the data obtained with a CCD camera, it was noted that the shot noise correction was not enough since a systematic increase persisted, suggesting another correction was needed.

- *Variance corrected speckle contrast*, κ_c: The extra correction needed, was found to be related to the dark variance of the images. Hence, in the experiments where a CCD camera was utilized, the speckle contrast calculation included both, shot and dark variance correction using the equation Equation 4.6. In the case of the sCMOS camera used in this work, the dark variance noise was found to be negligible, for the exposure times settings in the experiments, because the shot noise correction already extended the speckle contrast to the distances of interest in the experiments. However in case of a variance correction for a sCMOS camera, the variance calculation would require a different procedure [119].

For an observation on how the speckle contrast changes with the distance from the point source for every type of speckle contrast explained here, please refer to the results obtained from tissue phantoms and *in vivo* experiments (Figure 4.20(a) and Figure 4.28(a) respectively).

4.3.2 *Camera Choice*

In SCOS and SCOT, the purpose is to measure deep blood flow and to that end, the larger the source-detector separation at which the speckle contrast is usable, the deeper we can go probe the tissue to measure the blood flow. According to the noise corrections described previously, the contributions to the noise at large

distances come from the shot noise and the variance which are directly related to the specifications of a given camera. In order to choose a camera with the best characteristics to fit our expectations for the SCOS and SCOT systems, we performed some simulations based on the SNR model for camera sensors and the particular specifications for the cameras. Some experimental conditions were assumed and the f/# needed to match the speckle to pixel size, was calculated for each camera.

First, we assume a field-of-view (FOV) in which its horizontal dimension is 2.5 cm. The exposure time of the camera is fixed at 1 ms and the illumination wavelength is 785 nm corresponding to the actual wavelength used in the experiments.

The input parameters for each camera are:

- Pixel size [μm]
- Number of pixels in each direction (for some cameras, the whole detector is not used)
- Quantum efficiency, η [%]
- Inverse of overall system gain (1/K) [e−/DN]
- Saturation capacity [e^-]
- Temporal dark noise or readout noise [e^-]
- Bit depth

4.3.2.1 *Power Transference from the Object to the Detector*

Assuming a power emitted from a given speckle of area A, that is the *Emittance*, E, in units of [W/m^2], a perfect transmittance of the lens system, and an emitting speckle located at the center of the FOV, the radiance at a pixel in center of the detector is:

$$E' = \frac{E}{4f/\#^2} \tag{4.18}$$

Then, the mean number of photons that hit that pixel during the exposure time T_{exp}, is:

$$\mu_{photons} = \frac{A\lambda T_{exp}}{hc} E' \tag{4.19}$$

where h is the Planck constant and c is the speed of light.

Taking into account the quantum efficiency of the sensor at the working wavelength, it is possible to calculate the number of photons that are effectively converted into electrons as $\mu_{electrons} = \eta\mu_{photons}/100$.

To go from number of electrons detected at a pixel to digital units [DN] or counts, it is necessary to multiply them by the overall system gain, K. If it is not specified in the specs datasheet, it is possible to calculate it as $FWC/2^{bit\ depth}$, where FWC corresponds to the full well capacity of the system.

4.3.2.2 *Noise Model for a Given Detector*

With the aim of performing a comparison between detectors, the determination of the signal-to-noise relation (SNR) for each one is crucial. First we are going to define the different sources of noise that are involved in the detection process with a CCD camera. The principal source of noise, that is present in every sensor without exception, and that is related to the detection process is the *Shot noise*. This noise follows a Poisson statistics and as such, its variance is equal to its mean, having that $\sigma^2_{shot} = \mu_{electrons}$.

The sensor readout and the amplification circuits introduce a *dark noise* with variance $\sigma^2_{ampl} = \sigma^2_{readout} + \sigma^2_{darkcurrent}$. Also we have to include a contribution from the digitization or level quantization according to the bit depth of the camera, that is represented as $\sigma^2_q = 1/12\ DN^2$.

When calculating the noise of a signal that is detected with a camera, the different noises are expressed in units of electrons and are added up linearly, so according to the error propagation laws, the total noise is for a measured signal μ_y:

$$\sigma^2_y = K^2(\sigma^2_d + \sigma^2_e) + \sigma^2_q \tag{4.20}$$

Then, according to the EMVA 1288 standard, the SNR in terms of number of photons is defined as:

$$SNR(\mu_p) = \frac{\eta\mu_p}{\sqrt{\sigma^2_d + \eta\mu_p + \sigma^2_q/K^2}} \tag{4.21}$$

In the case of a perfect detector, the only noise present is the shot noise, so $SNR_{ideal} = \sqrt{\mu_p}$.

4.3.2.3 *Camera Models Compared*

Following the model described before and utilizing SNR relationship in Equation 4.21, we performed a comparison for some camera models we were aiming to use for SCOS measurements and decide on which could be the best alternative for this type of approach. The camera models included in this comparison are listed in Table 4.1.

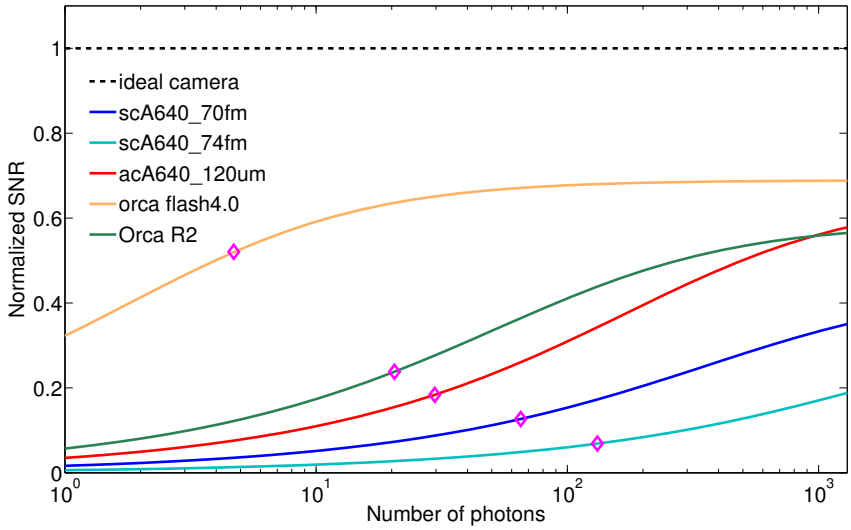

Figure 4.15: Normalized SNR for each compared camera with respect to incident photons. The diamonds (♢) at each curve represent the point at which SNR=1.

In Figure 4.15, we present the normalized SNR curves with respect to the number of incident photons at a pixel located in the center of the sensor, for all the cameras in Table 4.1. Besides, we have included the curve for an ideal camera, for which the normalized SNR would be equal to one for all the intensities. For every camera, there is a point indicating the number of photons at which the SNR is equal to 1. From this figure it is possible to observe that for the cameras scA640 and ac640, the number of photons needed to get a measurement is much higher than the number of photons

needed for the Orca flash 4.0. This is closely related to the saturation capacity, the number of bits and the readout noise of the camera. Hence, from this curve we would say that the best camera to perform SCOS measurements would be the Orca flash 4.0.

	sensor type	pixel size [µm]	# pixels	η@785nm [%]	1/K [$\frac{e^-}{DN}$]	sat. cap. [e^-]	$\sigma_{readout}$ [e^-]	bits
scA640 – 74fm	CCD	9.9	659x494	13.18	7	27000	17	12
scA640 – 70fm	CCD	7.4	659x494	18.94	3.6	14000	11	12
acA640 – 120um	CCD	5.6	659x494	42.22	4.1	16600	11	12
Orca – flash4.0	CMOS	6.5	1320x1216	47.5	0.4578	30000	1.3	16
Orca R2	CCD	6.45	700x500	16	0.2747	18000	6	12 / 16

Table 4.1: Specifications for the camera models used in the comparison

4.3.3 *Tissue Simulating Phantoms*

Every newly developed technique needs to be validated in some medium with known properties, in our case optical and dynamic properties; by comparing its results with those obtained with an already established technique. Following this statement, we validated SCOS in tissue-mimicking phantoms and compared its results to DCS measurements. For SCOT we created a phantom with a flow inhomogeneity and the results were validated in comparison to the flow rate given by the pump used to create the flow. In this section, a description of the tissue simulating phantoms used in the validations is presented, followed by the experimental methods developed in order to test SCOS's capability of retrieving the dynamic properties in such media and SCOT's ability to retrieve 3D flow information. The first SCOS experiment was performed in transmission geometry for multiple source-detector separation (S-D) separations at a given exposure time (T). This same setup allowed carrying out the tomographic measurement. Subsequently, SCOS measurements were carried out at different exposure times for a given S-D separation in the re-emission geometry. After this validation, a proof of SCOS in living tissue is shown with the description of the experiment.

4.3.3.1 *Tissue Simulating Phantoms*

Speckle contrast optical spectroscopy SCOS is a technique that allows measuring the dynamic properties of a medium. Particularly, it is capable to measure the blood flow in the tissue. Then, its validation has to be done in a medium that mimics the dynamic properties and the optical properties, in a range that matches those of the tissues being studied, that is, in a phantom [4]. Sometimes it is challenging to find the right materials to design a phantom that meets the conditions previously described. Provided that SCOS measures the same variable that is measured in DCS, and that we are comparing SCOS results with DCS measurements, we are going to use the same phantoms that are commonly utilized in DCS and other speckle based methods. According to DCS's literature, a suit-

4 Project: Optical Phantoms, http://omlc.org/ prahl/ projects/phantoms.html [Accessed 27 October 2014]

able phantom that closely resembles the dynamics of the tissue is a solution of Intralipid in water [27, 120].

Intralipid is a lipid solution that is clinically used for parenteral nutrition of patients who cannot be oral fed and it consists of soy bean oil, egg phospholipids and glycerin. A liquid phantom with a reduced scattering coefficient (μ_s') of 10 cm^{-1}, is usually achieved by preparing a 1% solution of Intralipid and a typical D_B value for this type of phantoms has been found to be 1×10^{-8} cm^2/s [27].

In Spain, the availability of Intralipid is reduced, but a substitute, Lipofundin® MCT/LCT 20% (B.Braun, Spain) is found. Although the concentration of the emulsion that we use for dilutions is the same as the Intralipid concentration cited in the literature [121], from our experience in the preparation of the liquid phantoms, we have found that for a 1% solution of Lipofundin, we usually get a μ_s'=7 cm^{-1}, so the volume of Lipofundin had to be adjusted during the preparation to obtain the targeted properties.

Having that the output of a SCOS measurement is the dynamic coefficient of a medium, it is important to show that it is capable of differentiating media with different dynamic properties. To prove that, we prepared two phantoms with different viscosity.

The first phantom consisted of a 1% solution of Lipofundin® MCT/LCT 20% (B.Braun, Spain) in water with $\mu_a = 0.026 cm^{-1}$, $\mu_s' = 6.31$ cm^{-1} and $D_B = (1.95 \pm 0.05) \times 10^{-8}$ cm^2/s. The second phantom was prepared with an increased viscosity which traduces in a reduced D_B value. It consisted of 50% Lipofundin® MCT/LCT (20%) and 50% glycerol (G2025, Sigma-Aldrich, Spain)- with $\mu_a = 0.02$ cm^{-1}, $\mu_s' = 9.72$ cm^{-1} and $D_B = (6.93 \pm 0.39) \times 10^{-10}$ cm^2/s. The optical properties of these phantoms were independently measured using time resolved spectroscopy (TRS) [122] at the wavelength used in both the SCOS and the DCS measurements. The D_B value was measured by DCS. From this point on, these phantoms will be denoted as Lipofundin phantom and glycerol phantom respectively.

For the tomographic method, a phantom with a flow heterogeneity was constructed. A container was filled with the Lipofundin® phantom which acted as background medium and to introduce the perturbation, a transparent plastic tube of 4mm diameter and 0.25mm wall thickness was placed inside the container. The tube was filled with the same liquid phantom used for the background and it was connected to a peristaltic pump (Watson-Marlow 520U) that allowed changing the velocity of the fluid inside the tube.

4.3.3.2 *SCOS in transmission geometry*

The first attempt to demonstrate the feasibility of SCOS was in a experiment in transmission geometry as illustrated in Figure 4.16. A continuous-wave, temperature controlled laser diode (Thorlabs L785P090, 785 nm, 90 mW) was focused down to 1 mm diameter and illuminated the sample from the bottom. The speckle patterns due to the transmitted light were imaged from the top with a monochrome scientific complementary metal-oxide- semiconductor camera (sCMOS; ORCA-Flash4.0, Hamamatsu, Japan $\gamma = 0.4578$). A lens with f=50 mm and f/#=16 was chosen to match the speckle size to pixel size. The sample liquid filled a transparent container with very thin walls up to a height of 1.5 cm giving a parallel plane slab geometry with thickness, $s = 1.5$cm.

Statistically independent speckle contrast measurements were acquired by scanning the point source in a three by twenty-five (3x25) grid centered in the field of view of the camera (4 cm x 3.5 cm). The exposure time was set to 1 ms and a frame rate of 100 fps was used to ensure that the speckles were temporally uncorrelated over the different images [106]. The point source illuminated each source position for 0.5 s, i. e., we have acquired up to fifty images at each position. In order to avoid any settling times, we have used only the latest thirty-five images for analysis.

For every image, we have defined 75 detectors with a size of twenty-five by twenty-five pixels (~0.75x0.75 mm^2). These detectors were positioned matching the 3x25 scanning grid. The speckle contrast was calculated in each of the defined detectors in regions

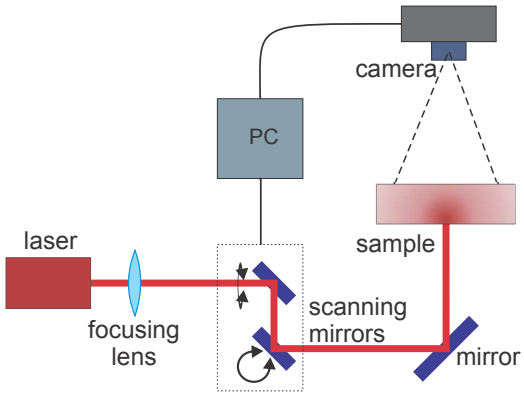

Figure 4.16: SCOS experimental set up in transmission: The laser is raster scanned illuminating the sample on one plane of a 1.5cm thick, parallel plane while the camera collects the transmitted speckles on the other plane. Figure reproduced from [110].

of five by five (5x5) pixels. Then these regions were temporally averaged over thirty-five frames and spatially averaged over the entire detector. This resulted in seventy-five by seventy- five source-detector pairs with a minimum source-detector distance of 1.5 cm, corresponding to the slab thickness, i.e. the phantom height.

4.3.3.3 *SCOT in transmission geometry*

The first demonstration of a three-dimensional flow reconstruction using SCOT was done in the tissue simulating phantom with a flow heterogeneity utilizing a transmission geometry. For this experiment, the setup, including the light source and detection system coincided with that presented in Section 4.3.3.2. The height of the background medium was set to 1.5 cm and its D_B value was obtained by SCOS. Then the tube was introduced into the background medium and filled with the same solution, guaranteeing in this sense, that the optical properties inside the tube and in the background medium were the same. The peristaltic pump allowed changing the velocity of the fluid inside the tube which was calculated from the relationship $V = 4F/(\pi d^2)$ between the diameter of the tube, d, and the flow, F, given by the pump in cm^3/s.

Given that SCOT is a tomographic method, it is necessary to perform measurements with multiple source-detector pairs. For this experiment, an array of 3 rows of 25 sources was defined, for a total of 75 sources. The distribution of the sources, the exposure time, time of the source at each position is exactly the same described in Section 4.3.3.2. The data acquisition geometry is shown in Figure 4.17, which consisted of a rectangular box of $5\text{cm} \times 3.8\text{cm} \times 1.5\text{cm}$. Even though the actual container of the liquid phantom was bigger, this geometry represents the imaging volume for the tomographic reconstruction. The sources were scanned along the three lines (dotted) where each line has 25 source positions and the intensity images are collected from the X-Z plane at Y=1.5 cm. This scanning was done using a pair of galvanometric mirrors (OFH-10, QS-7, Nutfield Technology,USA). This procedure was repeated for different velocities of fluid inside the tube starting from $V = 0$, representing the baseline for all the other velocities. The velocities used in the experiment were V =0.11, 0.21, 0.32, 0.43, 0.64, 0.85, 1.06, 2.12 and 3.18 cm/s.

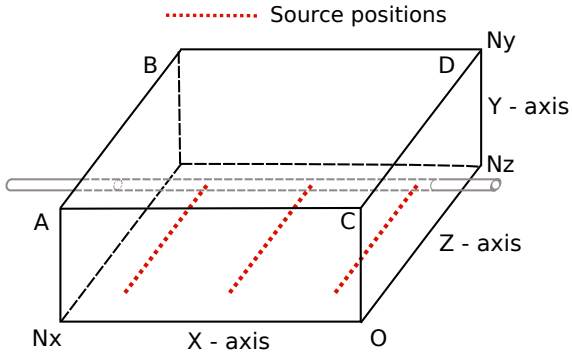

Figure 4.17: Data acquisition geometry of SCOT. Figure reproduced from [75].

In order to calculate speckle contrast, for each source in the image, 75 detectors were defined. These detectors were located exactly Y=1.5 cm above each source (X-Z plane), with a size of 25 by 25 pixels (~0.75x0.75 mm^2). Thereby, comprising a total of 75 by

75 source-detector pairs which serves as the SCOT data.

The shot noise corrected speckle contrast was calculated in every defined detector with a 5x5 sliding window size and averaged over frames to give a speckle contrast value for each detector.

4.3.3.4 *Re-emission geometry*

For many non-invasive *in vivo* applications, it is desirable to work with the re-emission geometry where the illumination and collection are done on the same surface. Here, we have used the same equipment, lens and field-of-view employed in the transmission experiment but the point source illumination was done through a 200µm multimode fiber in contact with the surface of the liquid phantom on the same plane as the camera field-of-view.

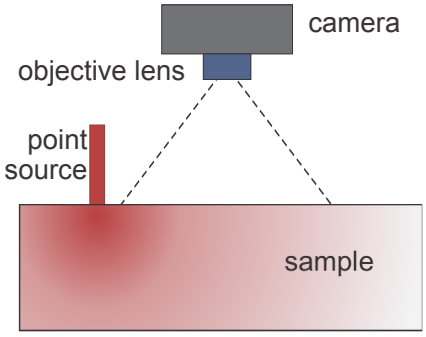

Figure 4.18: Re-emission geometry: The laser is coupled to a multi-mode optical fiber and illuminates the phantom on the same plane as the camera. Figure reproduced from [110].

To demonstrate the ability of SCOS to work with multiple exposure times even at a single source-detector separation, we have performed the measurement on the Lipofundin phantom where the fiber was fixed at one position for the whole experiment as presented in Figure 4.18. The active rows of the camera were reduced to eight to allow exposure times from 0.2 to 1 ms, and up to thousand images were obtained for each exposure time.

4.3.4 *In vivo Applications of SCOS*

After showing the feasibility of SCOS in tissue simulating phantoms, I present a demonstration of the method *in vivo* using a re-emission geometry on the human forearm muscle. The optical properties of the arm were measured with TRS obtaining $\mu_s' = 5.68\ cm^{-1}$ and $\mu_a = 0.11\ cm^{-1}$ and were utilized in the analysis to obtain a blood flow index "αD_B".

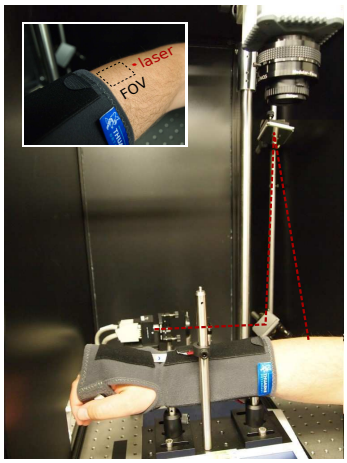

Figure 4.19: The photograph of the setup for the *in vivo* experiment. The inset figure depicts the approximate location of the source and the field-of-view. Figure reproduced from [110].

For this experiment, neutral density filters were placed after the focusing lens to ensure that the illumination power was below the maximum permissible exposure. The source position was fixed at one position out of the camera FOV for the whole measurement to avoid saturated pixels inside it. A CCD camera (Orca-R2, Hamamatsu, Japan, $\gamma = 0.2747$) was set to image a region of 2.4 x 1.8 cm^2 in the forearm with a lens with f=50mm and f/#=16 to match the pixel to speckle size. The camera was operated in the 16-bit mode and in the low light mode [123] to increase the quantum efficiency at the working wavelength. From the sensor, only 672x496 pixels were used and 1000 images were acquired at 16 fps for each exposure time from 250 µs to 5 ms. From these measurements, it is possible to work with both the dependence of the speckle contrast

on the distance from the point source and on the exposure time. Figure 4.19 shows a photograph of the set-up for the *in vivo* experiment. The arm is held in place using an adapted off-the-shelf wrist-cast.

HUMAN FOREARM MUSCLE - PRESSURE CUFF TEST Apart from the baseline measurement, and to show that SCOS is capable of measuring different ranges of human blood flow a cuff occlusion test was performed. The test consisted on measuring the baseline during 5 minutes, time at which the pressure cuff was inflated, as fast as possible, to 180 mm/Hg to occlude the arm by blocking the arterial blood flow. The occlusion was held at the same pressure during 3 minutes, followed by a rapid deflation of the pressure cuff to recanalize the flow. This recovery stage was measured during 5 minutes.

4.4 SCOS AND SCOT RESULTS

4.4.1 *Validation in Tissue Simulating Phantoms*

4.4.1.1 *Transmission Geometry-SCOS*

The speckle contrast of each 75x75 source- detector pair is plotted against the distance between each pair as shown in Figure 4.20(a) for the Lipofundin phantom [75]. We note that theoretically all pixels with a sufficient SNR can be utilized as an independent detector. The squares represent the speckle contrast calculated without any noise correction but it is seen that after about 1.7 cm there is a systematic deviation from the expected decay. In fact, even the early parts of this curve are affected by the additive variance due to shot-noise. The circles represent the corrected curve where working range is increased to about ~2.3 cm.

If we fit the uncorrected speckle contrast in the range from 1.5 cm to 1.7 cm we obtain a value of $D_B = 1.05 \times 10^{-9}$ cm^2/s which is one order of magnitude away from the measured value by DCS and indicates that the decay of this curve is not correct. On the other hand, the shot noise corrected data truncated at the point where SNR is too low as shown in Figure 4.20(b) gives

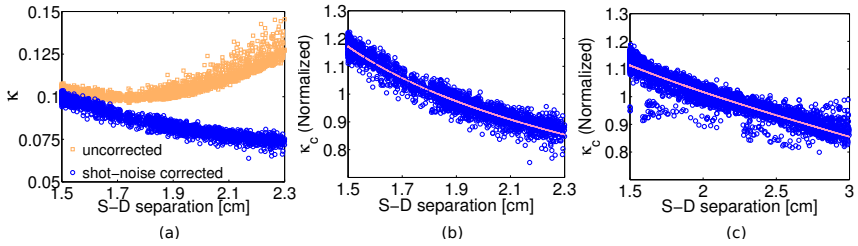

Figure 4.20: (a) The normalized speckle contrast for the Lipofundin phantom with (circles) and without (squares) shot noise correction [75]. (b) A comparison of experimental data to a fit for $D_B = 1.68 \times 10^{-8}$ cm^2/s obtained using SCOS for 1% Lipofundin phantom [75]. (c) Data and fit for $D_B = 5.31 \times 10^{-10}$ cm^2/s from a 50% glycerol-50% Lipofundin (20%) phantom.

$D_B = 1.68 \times 10^{-8}$ cm^2/s which is in reasonable agreement with the DCS measured value of $D_B = (1.95 \pm 0.05) \times 10^{-8}$ cm^2/s [75].

The same procedure described above was applied to characterize the glycerol phantom and the fitting results for this sample are presented in Figure 4.20 (c). The longer source-detector separation of 3.0 cm with good SNR in a sample with lower D_B is expected since the speckle contrast decreases slower compared to a sample with higher D_B. For the glycerol phantom, we have obtained $D_B = 5.31 \times 10^{-10}$ cm^2/s which is again in reasonable agreement with the DCS measured value of $D_B = (6.93 \pm 0.39) \times 10^{-10}$ cm^2/s.

4.4.1.2 *Transmission Geometry-SCOT*

The distribution of the flow inside the tube is depicted in the three dimensional slice plot in Figure 4.21a where the geometry shown is used for the simulations. As shown in Figure 4.21b, the sources are scanned along the XZ plane ($Y = 0$) and the intensity images are collected from the X-Z plane at $Y = N_y$ (plane ABCD) which serves as the detector plane. In particular, we discretize the (X,Y,Z) co-ordinates into 14, 8 and 16 points respectively which gives a total of 1792 voxels with a volume of 0.008 cm^3 for the three dimensional slab geometry.

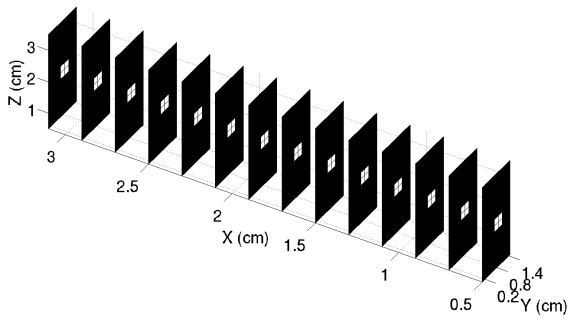

(a) The location of the tube (brighter region) in the geometry used for simulations.

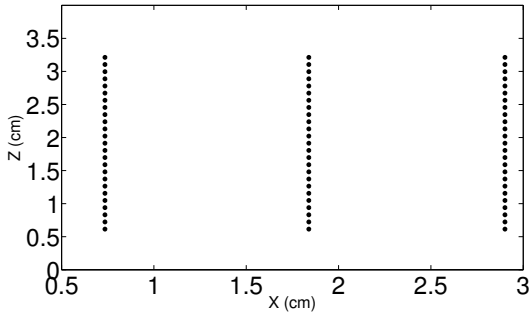

(b) The scanning positions of the sources and detectors. Here the sources and detectors are in two different planes (along Y-axis) which are 1.5cm apart.

Figure 4.21: The geometry of the scanning in SCOT along with the plot of Jacobian and location of the tube used to generate the flow. Figures reproduced from [75].

The speckle contrast due to the Brownian motion represented by κ_0, has to be determined *apriori* for the SCOT inversion procedure. This results correspond to the SCOS measurements in transmission mode presented in Section 4.3.3.2.

In Figure 4.22 we plot the perturbation in the speckle contrast from its background value along the Z- direction as a function of two different flows. Here v_1 is three times higher than the other (v_2). We clearly see the velocity dependent change in the speckle

contrast due to the flow in the tube.

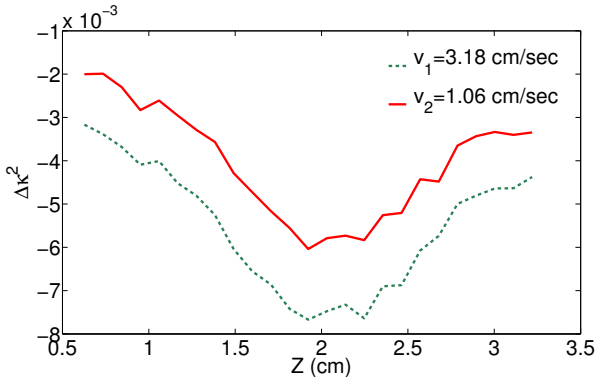

Figure 4.22: Perturbation in speckle contrast from the background, $\Delta\kappa^2$, for two different velocities differing approximately by three folds ($v_1 = 3v_2$). Figure reproduced from [75].

Here we consider only those detectors that lie within 2.3 cm of each source position. As sources are illuminated in a bounded rectangular geometry, the number of detectors per each source within a distance of 2.3 cm will vary according to the source positions. Therefore, the size of the Jacobian with the new set of detectors is 5269×1792. The normalized system of equation, as given in Equation 4.15, is solved for (V^2), whose square root gives the flow velocity.

For the reconstruction we have found, by trial and error, that $\lambda_2 = 10\lambda_1$ where we have obtain that $\lambda_1 = 0.1$ gives optimal results. The reconstructed flow profile, for the highest value of flow (3.18 cm/s), as a three dimensional slice plot is shown in Figure 4.23a. Similar plots for the velocities 1.06 cm/s and 0.32 cm/s are shown in Figures 4.23b and 4.23c respectively. The tube is clearly visible, albeit with a relatively poor resolution as expected from DOT images. Different velocities provide different amounts of contrast. To quantify the observed changes in velocity, we assign a predetermined volume (matching the original position of the tube) which comprises of the rectangular region formed by (X=0.5 to 3.1 cm, Y=0.65 cm to 0.85 cm and Z=1.7 cm to 1.9 cm)

with a total volume of 0.1040 cm^3. A plot of the integrated value of the reconstructed and original velocities in this predetermined volume is shown in Figure 4.24. The normalization is done by dividing the original and reconstructed flow corresponding to the flow value of 0.85 cm/s. A linear fit, using the data from original velocities ranging from 0.11 cm/s to 1.06 cm/s of the reconstructed flow gives a slope of 0.97. This slope is quite encouraging for this limited range. The underestimation for the larger perturbations, i.e. for larger velocities, is presumably due to the failure of the linearized Born approximation [124].

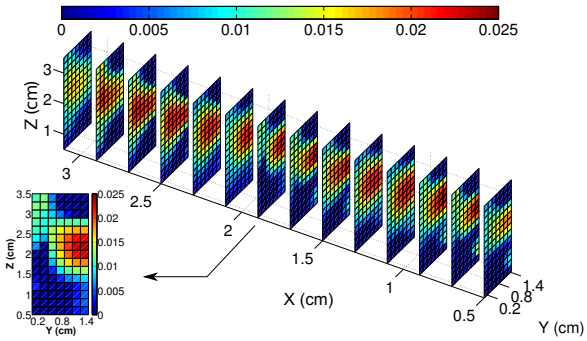

(a) Original velocity=3.18 cm/s.

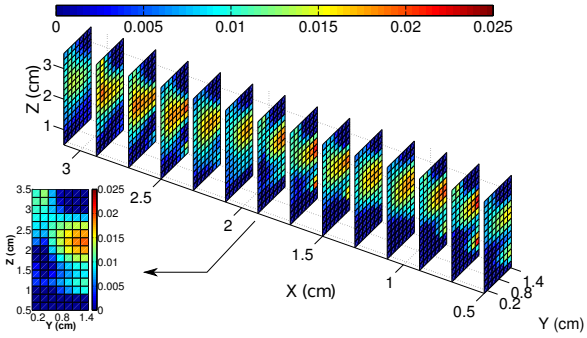

(b) Original velocity=1.06 cm/s

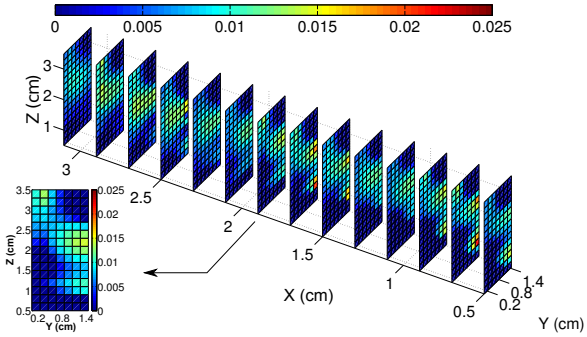

(c) Original velocity=0.43 cm/s

Figure 4.23: The three dimensional slice plot of the reconstructed flow velocity for original velocity of 3.18 cm/s, 1.06 cm/s and 0.43 cm/s are shown in (a), (b) and (c) respectively. Figures reproduced from [75].

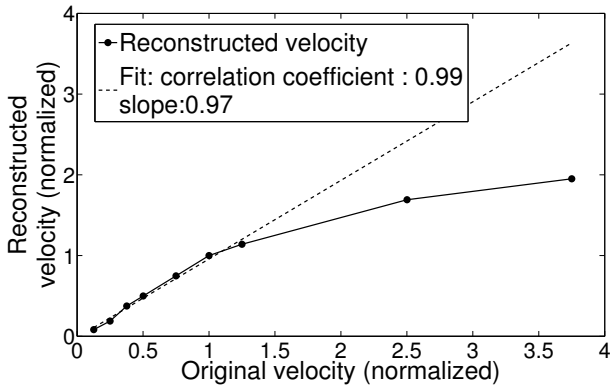

Figure 4.24: The volume integral of the reconstructed velocity against the original velocity, where the volume integration is done in a predetermined volume. Figure reproduced from [75].

4.4.1.3 *Re-emission Geometry*

Temporal speckle contrast analysis was done for every pixel with detectors at every 2.5 mm from 5 mm to 20 mm each one with a width of 0.75 mm. In Figure 4.25, we show the corrected speckle contrast as a function of the camera exposure time and the D_B obtained by fitting the theoretical model for the Lipofundin phantom at a detector located at 1.50 cm from the source. The obtained value was $D_B = 1.64 \times 10^{-8}$ cm^2/s which again, is in reasonable agreement with the values measured using DCS.

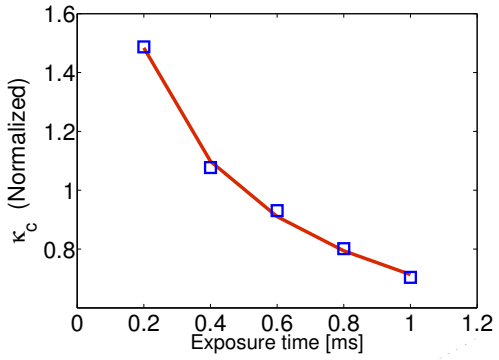

Figure 4.25: The normalized speckle contrast versus the exposure time at 1.5 cm from the source where $D_B = 1.64 \times 10^{-8}$ cm^2/s was obtained.

4.4.2 *In vivo Applications of SCOS*

4.4.2.1 *Human Forearm Muscle - Baseline Measurement*

After showing that SCOS is able to measure D_B with results comparable to those obtained with DCS in liquid phantoms, we present the results for the *in vivo* experiment shown in Figure 4.19. In order to check how the light intensity decays from the point source, we have averaged the intensity over thousand dark subtracted images and assigned a distance to every pixel taking as origin the position of the point source. Then, to improve the SNR in the measurements, and to average out inhomogeneities, we have defined ring detectors around the source each with a width of 0.5 mm. At

each ring, we have averaged all the pixels and assigned this intensity value to the mean distance between the inner and outer radii of the ring. This binned data is represented in Figure 4.26 which shows the intensity decay from 0.7 to 2 cm for an exposure time of 1 ms. Here it is also observed that the sensor was not saturated at shorter distances from the source available in the image and that at 2 cm the intensity was still decaying as expected from the diffusion theory. This is confirmed in the inset of this figure where we present the logarithm of the intensity in the same distance range.

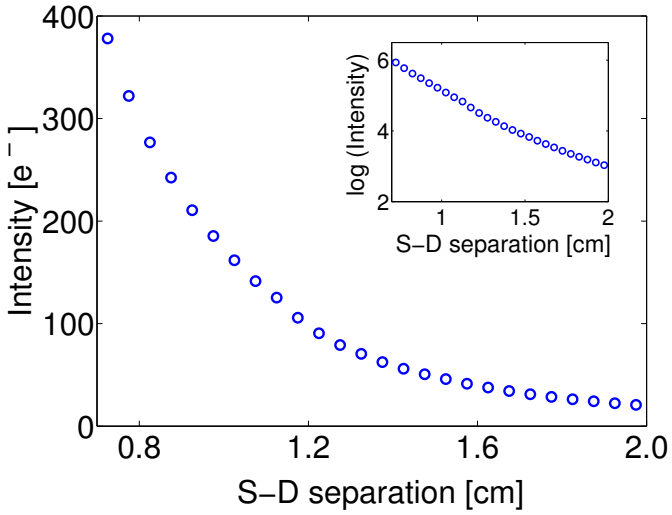

Figure 4.26: The *in vivo* data. The decay of the intensity over source-detector separation (S-D separation) in electrons. The inset shows the logarithm of the intensity. Figure reproduced from [110].

In order to demonstrate the correction procedure adopted for shot noise and the noises in dark images, Figure 4.27 shows different quantities that are used in it: the variance of the mean dark subtracted intensity ($\sigma^2(I - \mu_{I_D})$); the variance of the shot noise (σ_s^2); the shot variance corrected variance ($\sigma^2 - \sigma_s^2$); the dark variance (σ_d^2); and the dark and shot variance corrected variance ($\sigma^2 - \sigma_s^2 - \sigma_d^2$). All quantities are shown as a function of the measured intensity (in electrons) and the corresponding source-detector separation. For this graph, all the variables were calculated with a

sliding window to be comparable to all the speckle contrast calculations. The intersection of the shot noise variance and the dark variance define two regions at approximately $75e^{-}$, corresponding to a source-detector separation of approximately 1.3 cm. In other words, above $75e^{-}$ the shot noise dominates the dark variance and the previously described shot noise variance correction is mostly sufficient [112]. On the other hand, for the region below $75e^{-}$ where the dark variance noise dominates, the inclusion of dark variance correction is critical. These effects are particularly relevant for *in vivo* experiments where the SNR is low.

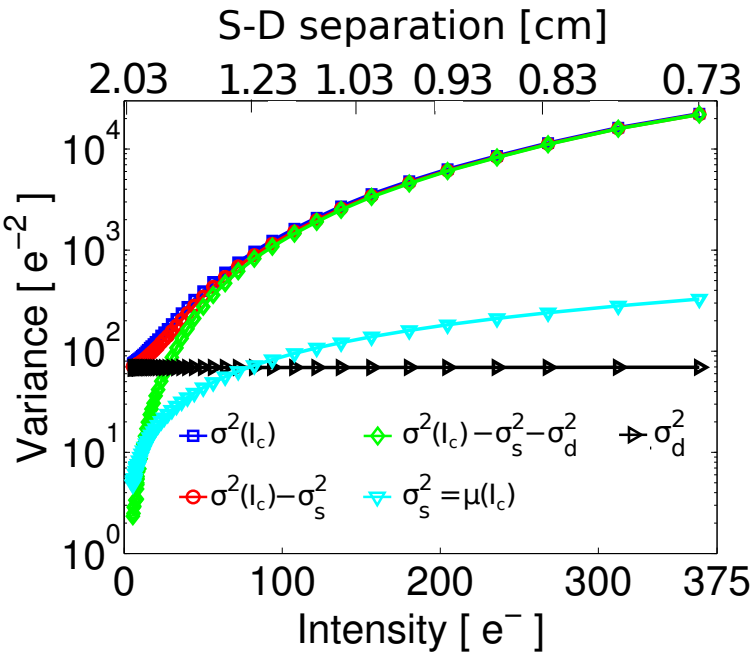

Figure 4.27: Representation of the variance of the dark subtracted intensity ($\sigma^2(I - \mu_{I_D})$), the variance of the shot noise (σ_s^2), the shot variance corrected variance ($\sigma^2 - \sigma_s^2$), the dark variance (σ_d^2) and the dark and shot variance corrected variance $\sigma^2 - \sigma_s^2 - \sigma_d^2$) used in the calculation of the corrected speckle contrast. All quantities are shown as a function of the measured intensity (in electrons, bottom axis) and the corresponding source-detector separation (top axis). Figure reproduced from [110].

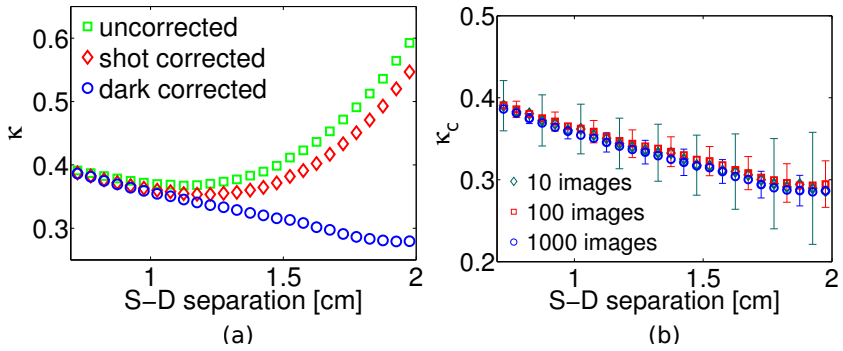

Figure 4.28: (a) The speckle contrast versus the source-detector separation with and without the two different corrections. (b) The standard deviation of the measurement for different number of averaged images. Figures reproduced from [110].

For this experiment, the speckle contrast was calculated in each image using a 5x5 sliding window and then a pixel based average was made using the acquired 1000 frames. Afterwards we binned the data as explained before for the intensity. The same procedure was applied for every acquired image sets under different exposure times. In Figure 4.28(a) we present the raw, the shot noise corrected and the shot and dark variance corrected speckle contrast as a function of source-detector separation for 1 ms exposure time. This figure demonstrates the effect of the noise variance in the speckle contrast calculation at large source-detector separations, where the intensity is very low and the detector dark variance dominates the measurements. It can be seen that the shot noise correction alone is sufficient for correcting the raw speckle contrast only up to about 1.2 cm. On the other hand, the shot noise and the dark corrections together extend the usable range of the speckle contrast in order to apply a model fitting up to above 1.9 cm. This could also be seen in Figure 4.26(b).

In this experiment, we have used 1000 images for the calculation of the averaged speckle contrast but to demonstrate the utility of the fast frame rates, in Figure 4.28(b) we present the calculation of the corrected speckle contrast when averaging 10, 100 and 1000 images with error bars representing the standard deviation of the speckle contrast at each distance. As expected, the SNR improves

with increased averages and allows the extension of the fitting range. In fact, fast CCD, CMOS cameras allow the acquisition of hundreds of samples in seconds and with this technology advancing rapidly, this could be improved. The only condition in the acquisition is that the time between images should be larger than the speckle decorrelation time.

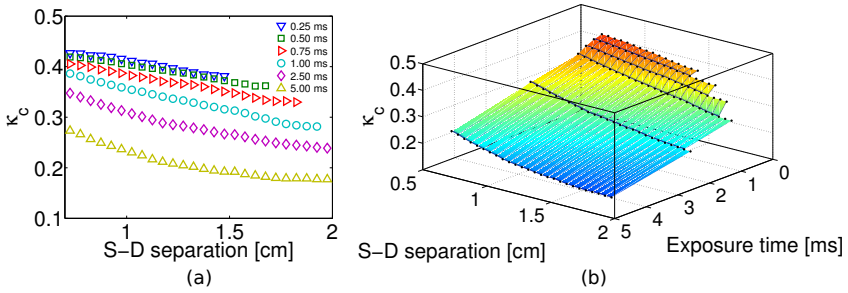

Figure 4.29: (a) Speckle contrast over distance for all the exposure times available in the SCOS measurement on a forearm muscle. (b) Surface plot of the data plotted in (a). Figure reproduced from [110].

The images for all the other exposure times were analyzed following the same procedure described before to calculate the speckle contrast and binning the data for the data taken at 1 ms exposure time. The results are presented in Figure 4.29(a), where the speckle contrast dependence with the distance is shown. It could be observed that for all exposure times, we have usable speckle contrast information up to 1.5 cm. Nevertheless, when the exposure time is increased, this distance is extended up to 2 cm for the largest exposure time which was 5 ms. An interesting way of presenting this data is shown in Figure 4.29(b), where a surface plot shows the dependence of the speckle contrast on both the distance and the exposure time for this particular experiment. The parts of the surface that appear cropped represent the regions for which the speckle contrast is dominated by the dark noise of the detector.

In Figure 4.30(a) The dark corrected speckle contrast as a function of distance in a range between 0.7 and 1.95 cm with a retrieved D_B of 1.34×10^{-9} cm^2/s is presented. On the other hand,

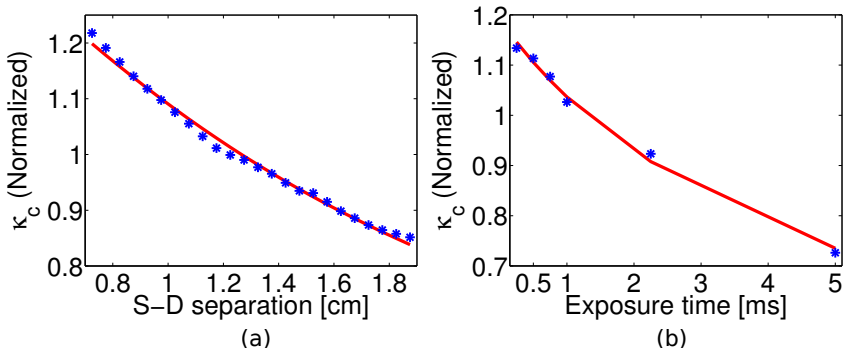

Figure 4.30: (a) Speckle contrast over distance in a forearm muscle where $D_B = 1.34 \times 10^{-9}$ cm^2/s was obtained with an exposure time of 2.5 ms. (b) Speckle contrast versus exposure times at 0.73 cm from the source for the same experiment with $D_B = 1.21 \times 10^{-9}$ cm^2/s. Figure reproduced from [110].

in Figure 4.30(b) where the exposure time approach at a distance of 0.73 cm is used, the D_B obtained was 1.21×10^{-9} cm^2/s. Both values are within the expected values from *in vivo* measurements and fitting the data in multiple different ways results in similar values.

4.4.2.2 *Human Forearm Muscle - Pressure Cuff Test*

Figure 4.31 shows the results before, during and after three minutes of arterial cuff occlusion of 180 mmHg. Multi-distance SCOS fitting as shown in Figure 4.30(a) was utilized at each time point corresponding to a temporal resolution of 3 seconds per point. The results are in overall agreement with previous work with DCS [125].

4.5 DISCUSSION

4.5.1 *Deep tissue blood flow measurements with SCOS*

In this chapter we have presented speckle contrast optical spectroscopy (SCOS) as a method to measure deep tissue blood flow non-invasively. The method was proposed and demonstrated using point source illumination and the simultaneous acquisition of

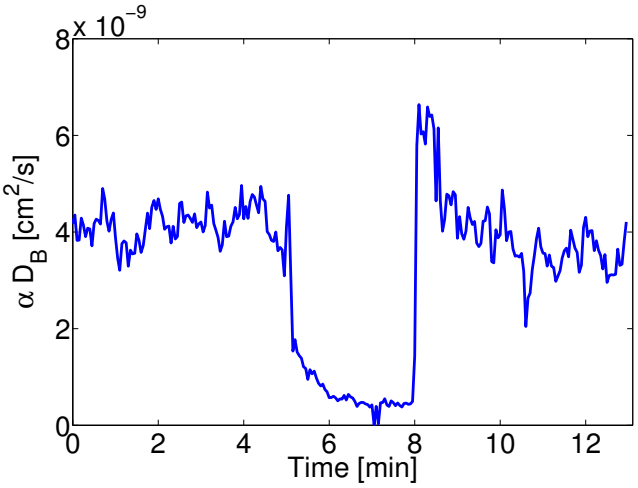

Figure 4.31: αD_B versus time using multi-distance SCOS as shown in Figure 4.30(a) before, during and after arterial cuff-occlusion. The cuff was rapidly occluded at ~ 5 minute to 180 mmHg and kept there for three minutes. Figure reproduced from [110].

speckle measurements at multiple distances using 2D array of detectors like a CCD or CMOS camera and/or measuring speckles at different exposure times. These results show that it is possible to model the dependence of the speckle contrast on the source-detector separation and the exposure time with a photon diffusion model. This model is fitted to the data and the information about the blood flow is obtained.

We have first demonstrated the theoretical behaviour of the speckle contrast with respect to the source-detector separation as well as the exposure time using the diffuse propagation model given a point source illumination. Then, in order to validate the theoretical model, we have performed experiments in tissue mimicking liquid phantoms. All these experiments were validated by a direct comparison to DCS which is a well known deep tissue blood flow measurement [10, 56, 57]. Our results in transmission geometry for two samples with different viscosity demonstrated that SCOS can measure the Brownian, particle diffusion coefficient of the scatterers accurately. Furthermore, to demonstrate the utility of SCOS

for a more easily accessible geometry, i. e., the re-emission geometry one liquid phantom was measured in a way to study both the source-detector separation and exposure time dependence of the measurements and we have obtained comparable results between both approaches. Finally, having validated SCOS in tissue mimicking phantoms, in both transmission and re-emission geometries, we have extended it to non-contact *in vivo* measurement of blood flow in the forearm muscle.

Overall, we assert that our results show that SCOS allows deep tissue blood flow measurements with comparable results to those obtained by DCS but the fact that SCOS uses fairly standard CCD/CMOS cameras, makes it a relatively low cost, fast method.

To put SCOS in a better context, we now compare it to the state-of-the-art in related techniques; laser speckle flowmetry (LSF), laser Doppler flowmetry (LDF) and diffuse correlation spectroscopy (DCS).

LSF uses the speckle contrast as a wide-field imaging method that uses a uniform illumination of the whole field- of-view and provides relatively fast mapping of blood flow with tens of micrometer spatial axial resolution with none or limited (~4 mm, using structured illumination) [126] depth resolution. It has been shown that, by employing LSF in transmission geometry, it is possible to sample deeper layers of the tissue (10-15 mm) but without quantification or depth resolution [127]. In contrast to the traditional full field illumination, doing a line beam scanning illumination improves the sampling depth of blood flow imaging [128] while doing laser speckle contrast imaging with point source illumination modulated in frequency over the exposure time allows the determination of the scattering properties of a static turbid medium [129].

As was mentioned earlier, it is noted that SCOS is a more general and quantitative method compared to similar speckle contrast point source measurements proposed previously [107, 108] due to the fact that it is a model based measurement. In these works, the authors introduced the proper model to relate the speckle contrast to the dynamics of the scatterers but they did not extract the dy-

namic parameters information directly from the speckle contrast measurement for a single source-detector separation and a single exposure time.

They kept their measurements in a range in which the dynamic parameters and the speckle contrast are linearly related and considered the inverse of the speckle contrast as an index of blood flow. In this work, we show how to use the dependence of the speckle contrast on the source- etector separation and/or the exposure time to do a model based, quantitative fitting as well as how to account for the systematic problems due to noise.

Laser Doppler flowmetry (LDF) is, in general, a point-by- point measurement using point-sources. Wide-field variants of LDF have been proposed in the past by utilizing two dimensional (2D) detectors [130] which is comparable to LSF in speed but requires a very high frame rate camera [104], although some variants including heterodyne optical-mixing detection allow the use of 8Hz CCD cameras [131].

LDF can be performed using large (1.5 cm) source-detector separations in order to analyze large tissue volumes but, in this approach, the main limitation of the LDF method is that the modeling and data acquisition becomes intractable with increased distance, leading itself to the time-domain methods such as DCS [132].

Diffuse correlation spectroscopy (DCS) is a diffuse optical method which probes deep tissues up to several centimeters using point-sources and detectors placed several centimeters away [10, 56, 57]. A common issue with DCS is the low signal-to-noise ratio (SNR) which is due to the need to sample each speckle independently using single-mode or few-mode fibers with small collection areas [10]. This implies that very few (order of 10,000) photons/second are detected by each (expensive) detector. For a given averaging time, the path for improved SNR is to use a collection of multiple detectors sampling several independent speckles simultaneously [133], i.e., ideally an array of fast single photon detectors. However, to achieve breakthrough improvements in SNR is prohibitively ex-

pensive and complex with the current technologies since the SNR increases with the square-root of the number of speckles.

SCOS is analogous to all three methods in being sensitive to the motion of the scatterers, i.e. red blood cells, in tissues. It is able to exploit the relatively inexpensive detectors with high frame rates that LSF can utilize with the multiple scattering, i.e. deep tissue, sensitivity of DCS. These detectors allow the potential of improved SNR by averaging thousands of speckles in space and/or time. As our previous paper has demonstrated, this also allows for a tomographic approach [75] and this work paves the way towards its *in vivo* application.

In our SCOS experiments, we have established the importance of accounting for the contributions of both the shot noise and the sensor noise to the speckle contrast. In Figure 4.20(a) we have shown that it is crucial to correct for the shot noise contribution in order to get an accurate measurement of blood flow. Then, as seen in Figure 4.28(a) we have shown that it is further important to correct for the dark variance at large detection distances when working at lower light levels. These corrections are not critical in traditional LSF measurements because the intensity over all the images is homogeneous and, usually, when working with different exposure times, the intensity at the detector is set to be constant for all of them to keep the shot noise constant over all the experiment [109].

Several aspects of SCOS require further research and improvement. We now discuss some important effects and suggest potential solutions. For example, there are other sources of noise from both CCD and CMOS cameras whose variance may cause systematic errors. This is evident in the *in vivo* experiment in re-emission geometry where even after including the noise corrections, we are not able utilize the whole range where the intensity continues to decay according to the photon diffusion level. In other words, the SNR of the intensity is greater than one but there are sources of variance that dominate the speckle contrast. A further characterization of the camera technologies and the consideration of different technologies such as single-photon counting avalanche photo

detector arrays may allow us to overcome this limitation. Nevertheless, our results show that we can work at source- detector separations up to ≈2 cm at the current state of SCOS which is relevant for numerous applications ranging from small animal measurements to adult humans.

We note that Equation 4.2 is an integral over the correlation delay times over the field auto-correlation function. Therefore, in general, SCOS does not retain the fine-details that DCS measurements which are contained in the complete shape of the auto-correlation curve. This is not expected to be very important for *in vivo* experiments of relatively homogeneous tissues but may be relevant in multi-layered tissues with large differences between the blood flow in different layers. This could be partially accounted for by doing tomography, i.e. by SCOT. This also implies a potential issue with volumes of high blood flow which is also limitation for DCS in exceptional cases. Finally, the same integral may imply a loss of sensitivity to very small changes in blood flow when using larger exposure times that are comparable to the correlation decay time. To overcome this, the exposure time could be further reduced but this has implications in SNR. These effects should carefully be characterized in the future.

In all the measurements presented in this work, we have matched the speckle size to pixel size, but perhaps, according to some references [134, 135] the results could be improved by increasing the speckle to pixel size ratio. This is readily possible by controlling the aperture of the camera lenses but we have chosen to stick to the simpler, more generally utilized approach to demonstrate the feasibility of SCOS. Finally, since SCOS is a non-contact measurement, it relies on the correct calibration of the source-detector distance with a source that is often out of the field-of-view which is a challenge for *in vivo* measurements on curved surfaces. Motion and surface artifacts also affect the measurements. These could be dealt with by building better interfaces with appropriate windows and/or by using fiber- coupled cameras as was suggested previously [108].

4.5.2 *Tomographic reconstruction of blood flow with SCOT*

We have presented a new tomographic imaging method, speckle contrast optical tomography (SCOT), to measure the blood flow distributed in deeper regions of the tissue. We have proposed and demonstrated that by scanning the point laser source over the sample and acquiring multiple speckle measurements simultaneously using a array of detectors like a CCD or CMOS camera, we are able to model the speckle statistics with a photon diffusion model, fit the model to the data to obtain information about sample dynamics and use in a tomographic inverse problem.

After deriving the physical model and a linearized inversion model, we have carried experiments in a liquid phantom with a cylindrical inclusion with varying flow rates of scatters in the transmission geometry. We were able to obtain three dimensional reconstructions and quantify the flow rate over a large range. For the *in vivo* applications, this technique would allow us to image local or temporal variations in blood flow for example due to neuronal stimuli, pharmacological or physiological changes in time or heterogeneities due to local ischemia or a tumor.

In general, the inverse problem associated with the recovery of MSD from the speckle contrast measurement can be re-casted as nonlinear optimization problem. We have adopted the standard procedure to linearize the non-linear inverse problem using the Born approximation. We have derived the sensitivity relation connecting the perturbations in speckle contrast measurements from its baseline value to the changes in flow velocity. In the discretized geometry, the sensitivity relation is called the Jacobian which was plotted for a given source-detector pair to show that it preserves the so-called banana path as observed in DOT. We have further plotted the corrected speckle contrast as a function of spatial coordinates versus different values of flow velocity to show the sensitivity of the data for inversion to the perturbations in flow. Having computed the Jacobian and measure the perturbation in speckle contrast from its baseline value, we presented the recovery of the flow velocity using Tikhonov-regularized least square minimization. In a nutshell, SCOT overcomes the limited dynamic range

and low SNR of DWS (and hence DCT) and lower penetration depth of LSF and provides a three dimensional distribution of flow in tissue using faster and cheaper instrumentation.

We acknowledge that the spatial localization of the reconstructed flow velocity values needs further improvement as evident from plots in Figure 4.23. This suggests the implementation of a denser scanning of the source in the XZ plane as the slices near to the source positions are having good spatial localization of the flow profile. This also reduces the inherent ill-posedness associated with the inverse problems involving the diffusion equation. This type of denser scanning would have been prohibitively expensive and/or time consuming with the current DCT technologies. However, with SCOT, this can readily be implemented.

The limited linear range in measuring the flow velocity as revealed by the plot in figure Figure 4.24 suggests to adopt an iterative Born inversion instead of the first Born approximation. As discussed above, the estimation of errors associated with the Born's approximation was previously carried out in the context of DOT [114] and was experimentally demonstrated [124]. A more accurate nonlinear-iterative reconstruction algorithm can be adopted to improve the accuracy of the reconstruction as was already presented for DCT and DOT using numerical methods such as finite element methods (FEM) [70, 72].

The results shown here are still a bit limited in dynamic range since the data is plagued by systematic deviations from the theoretical model due to unaccounted sources of noise. For them, only shot noise along with a method to remove its effect has been considered. Other noise sources like read noise, flat pixel noise, variability of hot pixels have to be accounted to derive an accurate noise model, that is still not included in the noise model presented in this work, due to the nature of the sCMOS detectors in which every pixel has its own electronics. The next step for SCOT is to translate these measurements to non-invasive, non-contact measurements of the 3D blood flow *in vivo*, which now seem feasible after the demonstration of SCOS *in vivo* in the re-emission geome-

try shown in Section 4.4.2.

4.6 CONCLUSIONS

Deep tissue perfusion imaging is considered as one of the important imaging problems in the medical imaging research. In summary, in this chapter, we have proposed and demonstrated speckle contrast optical spectroscopy (SCOS), as a diffuse optical method to non-invasively measured the deep tissue blood flow using fairly standard CCD/sCMOS cameras. This is based in the fact that it is possible to model the speckle statistics with a photon diffusion model, fit the model to the data and obtain information about sample dynamics. The method was demonstrated in both transmission and reflectance geometries using both spatial and temporal speckle contrast analysis in liquid tissue mimicking phantoms. Afterwards, the feasibility of SCOS in *in vivo* experiments was presented using both dependences of the speckle contrast in the source-detector separation and the exposure time.

Moreover, we have developed and experimentally demonstrated a new optical method for three dimensional imaging of blood flow in tissues. Speckle contrast optical tomography (SCOT) is based on laser speckle contrast approaches and combines the physical models utilized in diffuse correlation tomography (DCT) with laser speckle flowmetry (LSF). When multiple SCOS measurements were performed by scanning the laser point source over the sample and acquiring multiple speckle measurements simultaneously using a array of detectors like a CCD or CMOS camera, we have proposed and demonstrated that it is possible to build a jacobian and use it in a tomographic inverse problem to retrieve flow inhomogeneities in a sample. With SCOT, we have presented the first demonstration of a tomographic reconstruction of flow using speckle contrast as measurement in flow phantoms.

5

CONCLUSIONS

In this thesis we developed and tested optical imaging methods for blood perfusion. There are two major contributions presented in this thesis, one being the development of an LSF-OIS based system to study ischemic stroke models in rodents. The second major contribution is the development of a novel diffuse optics based three dimensional deep tissue blood flow imaging method, called speckle contrast optical spectroscopy (SCOS) and its tomographic extension, speckle contrast optical tomography (SCOT).

During this work, I have contributed with the construction, validation and application of a multimode device to measure simultaneously, cerebral blood flow (CBF) and blood oxygenation in animal models: LSF-OIS device. Although this device is based on existing technologies, laser speckle flowmetry (LSF) and optical intrinsic signal imaging (OIS), the experimental methods developed for the co-registration of images obtained at different points in a longitudinal study are one contribution of this work. Furthermore, this device was applied in a multidisciplinary study with the department of Brain Ischemia and Neurodegeneration at the Institute for Biomedical Research in Barcelona (IIBB), to understand the role of the Mannose-binding lectin (MBL) protein after the reperfusion following a temporal middle cerebral artery occlusion (tMCAO). The measurements performed with this device helped validating the hypothesis that the MBL protein promotes the activation of the thrombin, enhancing the coagulation after the reperfusion.

We have introduced speckle contrast optical spectroscopy (SCOS), a new deep tissue blood flow measurement, which comprises a coherent point source illumination and a two dimensional array, e. g., CCD, which measures the dynamic speckle patterns formed by the scattered light. SCOS utilizes the speckle contrast measurements along with the correlation diffusion model to quantitatively measure deep tissue blood flow. We introduced a noise correction method to account for the effect of shot and dark noises, associated with CCD/sCMOS, in speckle contrast measurements. We also presented two methods to perform SCOS measurements, one uses the dependence of the speckle contrast on the source-detector separation and the other utilizes speckle contrast obtained at multiple exposure times. We validated SCOS in tissue mimicking phantoms in transmission and re-emission geometries. We further tested SCOS feasibility to measure blood flow changes during arterial cuff occlusion in human arm muscle.

In order to account for heterogeneous distribution of blood flow, we developed a tomographic imaging method, speckle contrast optical tomography (SCOT), which integrates the principles of SCOS. We developed an inversion algorithm based on First Born approximation, based on which a sensitivity relation, connecting relative changes in blood flow to the changes in speckle contrast measurements, was derived. The inversion model that we presented is general such that both, the Brownian motion as well as the random flow can be accounted for. SCOT was validated in tissue mimicking flow phantoms, where we were able to recover three dimensional flow distribution. Having validated SCOS *in vivo* experiments, we are currently trying to deploy SCOT in re-emission geometry, for in vivo experiments.

Currently there is a need of a low-cost, minimally invasive technique that allows three dimensional deep imaging of cerebral blood flow (CBF) in the rodent brain in order to have information comparable to those obtained by imaging techniques for humans. This facilitates the translation of the results in animal models of diseases, such as stroke, to the humans. In such studies, the measurement of the infarct volume is a standard to determine the severity of the stroke. The current method to measure the infarct volume consists

in sacrificing the animal, staining the brain with Triphenyl tetrazolium chloride (TTC), slicing it and measure the infarct area in the brain slices. Hence, in a longitudinal study, in which different times after the occlusion are observed to evaluate the evolution of the stroke, some animals would be sacrificed at each of these time points. To avoid this, SCOT could be used as a non-invasive technique to determine the infarct volume evolution after the stroke at different time points, not only reducing the number of animals involved in the experiment but also reducing the variabilities induced by the use of different animals at different time points.

The main potential advantage of SCOS and SCOT is the deep perfusion imaging capability along with rapid data acquisition even with a very dense sampling of sources and detectors without being prohibitively expensive. An improved SNR, due to the wide-field acquisition with thousands of speckles in a small region as well as high density tomographic measurements makes SCOS and SCOT promising techniques for deep perfusion measurement and imaging.

BIBLIOGRAPHY

[1] AK Jayanthy, N Sujatha, and M Ramasubba Reddy. Measuring blood flow: Techniques and applications-a review. *arpapress. com*, 6:203–216, 2011.

[2] Vladimir C Hachinski, Linnette D Iliff, Elias Zilhka, George H Du Boulay, Victor L McAllister, John Marshall, Ralph W Ross Russell, and Lindsay Symon. Cerebral blood flow in dementia. *Archives of neurology*, 32(9):632–637, 1975.

[3] Norbert Schuff, Shinji Matsumoto, Joseph Kmiecik, Colin Studholme, Antao Du, Frank Ezekiel, Bruce L Miller, Joel H Kramer, William J Jagust, Helen C Chui, et al. Cerebral blood flow in ischemic vascular dementia and Alzheimer's disease, measured by arterial spin-labeling magnetic resonance imaging. *Alzheimer's & Dementia*, 5(6):454–462, 2009.

[4] Alan D Lopez, Colin D Mathers, Majid Ezzati, Dean T Jamison, and Christopher JL Murray. Global and regional burden of disease and risk factors, 2001: systematic analysis of population health data. *The Lancet*, 367(9524):1747–1757, 2006.

[5] Matthias Endres, Britta Engelhardt, Jari Koistinaho, Olle Lindvall, Stephen Meairs, Jay P Mohr, Anna Planas, Nancy Rothwell, Markus Schwaninger, Martin E Schwab, et al. Improving outcome after stroke: overcoming the translational roadblock. *Cerebrovascular Diseases*, 25(3):268–278, 2008.

[6] Aysan Durukan and Turgut Tatlisumak. Acute ischemic stroke: overview of major experimental rodent models, pathophysiology, and therapy of focal cerebral ischemia. *Pharmacology Biochemistry and Behavior*, 87(1):179–197, 2007.

[7] Ulrich Dirnagl, Costantino Iadecola, and Michael A Moskowitz. Pathobiology of ischaemic stroke: an integrated view. *Trends in neurosciences*, 22(9):391–397, 1999.

[8] DO Wiebers, HP Adams, and JP Whisnant. Animal models of stroke: are they relevant to human disease. *Stroke*, 21(1): 1–3, 1990.

[9] Walter J Koroshetz and Michael A Moskowitz. Emerging treatments for stroke in humans. *Trends in pharmacological sciences*, 17(6):227–233, 1996.

[10] T Durduran, R Choe, W Baker, and A G Yodh. Diffuse Optics for tissue monitoring and tomography. *Rep Prog Phys*, 73(7):076701–076744, 2010.

[11] Frank Kober, Guillaume Duhamel, and Patrick J Cozzone. Experimental comparison of four FAIR arterial spin labeling techniques for quantification of mouse cerebral blood flow at 4.7 T. *NMR in biomedicine*, 21(8):781–792, 2008.

[12] Elizabeth MC Hillman. Optical brain imaging in vivo: techniques and applications from animal to man. *Journal of biomedical optics*, 12(5):051402–051402, 2007.

[13] Aysan Durukan and Turgut Tatlisumak. Ischemic stroke in mice and rats. In *Cardiovascular Genomics*, pages 95–114. Springer, 2009.

[14] Cenk Ayata, Andrew K Dunn, Yasemin Gursoy-Özdemir, Zhihong Huang, David A Boas, and Michael A Moskowitz. Laser speckle flowmetry for the study of cerebrovascular physiology in normal and ischemic mouse cortex. *Journal of Cerebral Blood Flow & Metabolism*, 24(7):744–755, 2004.

[15] Phill B Jones, Hwa Kyoung Shin, David A Boas, Bradley T Hyman, Michael A Moskowitz, Cenk Ayata, and Andrew K Dunn. Simultaneous multispectral reflectance imaging and laser speckle flowmetry of cerebral blood flow and oxygen metabolism in focal cerebral ischemia. *Journal of biomedical optics*, 13(4):044007–044007, 2008.

[16] Demirhan Kobat, Nicholas G Horton, and Chris Xu. In vivo two-photon microscopy to 1.6-mm depth in mouse cortex. *Journal of biomedical optics*, 16(10):106014–106014, 2011.

[17] Vivek J Srinivasan, Sava Sakadžić, Iwona Gorczynska, Svetlana Ruvinskaya, Weicheng Wu, James G Fujimoto, and David A Boas. Quantitative cerebral blood flow with optical coherence tomography. *Optics express*, 18(3):2477–2494, 2010.

[18] Minghua Xu and Lihong V Wang. Photoacoustic imaging in biomedicine. *Review of scientific instruments*, 77(4):041101, 2006.

[19] Elizabeth Hillman, David A Boas, Anders M Dale, and Andrew K Dunn. Laminar optical tomography: demonstration of millimeter-scale depth-resolved imaging in turbid media. *Optics letters*, 29(14):1650–1652, 2004.

[20] J David Briers. Laser Doppler and time-varying speckle: a reconciliation. *JOSA A*, 13(2):345–350, 1996.

[21] Vasilis Ntziachristos. Going deeper than microscopy: the optical imaging frontier in biology. *Nature methods*, 7(8):603–614, 2010.

[22] HC Van De Hulst. *Light scattering by small particles*. Dover Publications, 1981.

[23] Jorge Ripoll Lorenzo. *Principles of Diffuse Light Propagation*. World Scientific Publishing, 2012. ISBN 978-981-4293-76-1.

[24] Arjun Yodh and Britton Chance. Spectroscopy and imaging with diffusing light. *Physics Today*, 48(3):34–41, 1995.

[25] Subrahmanyan Chandrasekhar. *Radiative transfer*. Courier Dover Publications, 1960.

[26] Boris Davison and John Bradbury Sykes. *Neutron transport theory*. Oxford University Press, 1957.

[27] David A. Boas. *Diffuse Photon Probes of Structural and Dynamical Properties of Turbid Media: Theory and Biomedical Applications*. PhD thesis, University of Pennsylvania, 1996.

[28] Akira Ishimaru. *Wave propagation and scattering in random media*, volume 2. Academic press New York, 1978.

[29] Ashley J. Welch and Martin J.C. van Gemert, editors. *Optical-Thermal Response of Laser-Irradiated Tissue*. Springer, second edition, 2011.

[30] T Durduran, AG Yodh, B Chance, and DA Boas. Does the photon-diffusion coefficient depend on absorption? *JOSA A*, 14(12):3358–3365, 1997.

[31] Matthias Kohl, Ute Lindauer, Georg Royl, Marc Kühl, Lorenz Gold, Arno Villringer, and Ulrich Dirnagl. Physical model for the spectroscopic analysis of cortical intrinsic optical signals. *Physics in medicine and biology*, 45(12):3749, 2000.

[32] Simon R Arridge, M Cope, and DT Delpy. The theoretical basis for the determination of optical pathlengths in tissue: temporal and frequency analysis. *Physics in medicine and biology*, 37(7):1531, 1992.

[33] J. D. Briers. Speckle fluctuations and biomedical optics: implications and applications. *Optical Engineering*, 32(2):277–283, 1993. doi: 10.1117/12.60734. URL http://dx.doi.org/10.1117/12.60734.

[34] Hector J Rabal and Roberto A Braga Jr. *Dynamic laser speckle and applications*. CRC Press, 2010.

[35] Joseph M Schmitt, SH Xiang, and Kin M Yung. Speckle in optical coherence tomography. *Journal of biomedical optics*, 4 (1):95–105, 1999.

[36] Artur Zdunek, Anna Adamiak, Piotr M Pieczywek, and Andrzej Kurenda. The biospeckle method for the investigation of agricultural crops: A review. *Optics and Lasers in Engineering*, 52:276–285, 2014.

[37] Hui Wang and Andrew M Rollins. Speckle reduction in optical coherence tomography using angular compounding by B-scan Doppler-shift encoding. *Journal of biomedical optics*, 14(3):030512–030512, 2009.

[38] L Allen and DGC Jones. An analysis of the granularity of scattered optical maser light. *Physics Letters*, 7(5):321–323, 1963.

[39] BM Oliver. Sparkling spots and random diffraction. *Proceedings of the IEEE*, 51(1):220–221, 1963.

[40] JD Rigden and EI Gordon. Granularity of scattered optical maser light. In *Proceedings of the Institute of Radio Engineers*, volume 50, page 2367, 1962.

[41] Hans M Pedersen. Theory of speckle dependence on surface roughness. *JOSA*, 66(11):1204–1210, 1976.

[42] Kishore V. Chellappan, Erdem Erden, and Hakan Urey. Laser-based displays: a review. *Appl. Opt.*, 49(25):F79–F98, Sep 2010. doi: 10.1364/AO.49.000F79. URL http://ao.osa.org/abstract.cfm?URI=ao-49-25-F79.

[43] Chien-Yue Chen, Wei-Chia Su, Ching-Huang Lin, Ming-De Ke, Qing-Long Deng, and Kuan-Yao Chiu. Reduction of speckles and distortion in projection system by using a rotating diffuser. *Optical review*, 19(6):440–443, 2012.

[44] Joseph W Goodman. *Speckle phenomena in optics: theory and applications*, volume 1. Roberts and Company, 2007.

[45] David Monaghan, Damien Kelly, Bryan Hennelly, and Bahram Javidi. Speckle reduction techniques in digital holography. In *Journal of Physics: Conference Series*, volume 206, page 012026. IOP Publishing, 2010.

[46] Y. Aizu and T. Asakura. Bio-speckle phenomena and their application to the evaluation of blood flow. *Optics & Laser Technology*, 23(4):205–219, 1991. ISSN 0030-3992. doi: 10.1016/0030-3992(91)90085-3. URL http://www.sciencedirect.com/science/article/pii/0030399291900853.

[47] Gary Cloud. Optical Methods in Experimental Mechanics. *Experimental Techniques*, 31(1):15–17, 2007. ISSN 1747-1567. doi: 10.1111/j.1747-1567.2006.00129.x. URL http://dx.doi.org/10.1111/j.1747-1567.2006.00129.x.

[48] Gary Cloud. Optical Methods in Experimental Mechanics. *Experimental Techniques*, 31(2):17–19, 2007. ISSN 1747-1567. doi: 10.1111/j.1747-1567.2007.00167.x. URL http://dx.doi.org/10.1111/j.1747-1567.2007.00167.x.

[49] JC Dainty. I The statistics of speckle patterns. *Progress in optics*, 14:1–46, 1977.

[50] Joseph W Goodman. Some fundamental properties of speckle. *JOSA*, 66(11):1145–1150, 1976.

[51] Joseph W Goodman. Statistical properties of laser speckle patterns. In J. Christopher Dainty, editor, *Laser speckle and related phenomena*, volume 9 of *Topics in Applied Physics*, pages 9–75. Springer-Verlag, 1975.

[52] P-A Lemieux and DJ Durian. Investigating non-Gaussian scattering processes by using< i> n th-order intensity correlation functions. *JOSA A*, 16(7):1651–1664, 1999.

[53] Chao Zhou. *In-vivo optical imaging and spectroscopy of cerebral hemodynamics*. PhD thesis, Department of Physics and Astronomy, 2007.

[54] BJ Ackerson, RL Dougherty, NM Reguigui, and U Nobbmann. Correlation transfer-application of radiative transfer solution methods to photon correlation problems. *Journal of thermophysics and heat transfer*, 6(4):577–588, 1992.

[55] RL Dougherty, BJ Ackerson, NM Reguigui, F Dorri-Nowkoorani, and U Nobbmann. Correlation transfer: development and application. *Journal of Quantitative Spectroscopy and Radiative Transfer*, 52(6):713–727, 1994.

[56] D. A. Boas, L. E. Campbell, and A. G. Yodh. Scattering and Imaging with Diffusing Temporal Field Correlations. *Phys. Rev. Lett.*, 75:1855–1858, Aug 1995. doi: 10.1103/PhysRevLett.75.1855. URL http://link.aps.org/doi/10.1103/PhysRevLett.75.1855.

[57] DA Boas and AG Yodh. Spatially varying dynamical properties of turbid media probed with diffusing temporal light correlation. *JOSA A*, 14(1):192–215, 1997.

[58] Stefan A Carp, Nadàege Roche-Labarbe, Maria-Angela Franceschini, Vivek J Srinivasan, Sava Sakadžić, and David A Boas. Due to intravascular multiple sequential scattering, diffuse correlation spectroscopy of tissue primarily measures relative red blood cell motion within vessels. *Biomedical optics express*, 2(7):2047–2054, 2011.

[59] Daniele Contini, Fabrizio Martelli, and Giovanni Zaccanti. Photon migration through a turbid slab described by a model based on diffusion approximation. I. Theory. *Applied optics*, 36(19):4587–4599, 1997.

[60] Richard C. Haskell, Lars O. Svaasand, Tsong-Tseh Tsay, Ti-Chen Feng, Bruce J. Tromberg, and Matthew S. McAdams. Boundary conditions for the diffusion equation in radiative transfer. *J. Opt. Soc. Am. A*, 11(10):2727–2741, Oct 1994. doi: 10.1364/JOSAA.11.002727. URL http://josaa.osa.org/abstract.cfm?URI=josaa-11-10-2727.

[61] R Bonner and R Nossal. Model for laser Doppler measurements of blood flow in tissue. *Applied optics*, 20(12):2097–2107, 1981.

[62] Turgut Durduran and Arjun G Yodh. Diffuse correlation spectroscopy for non-invasive, micro-vascular cerebral blood flow measurement. *NeuroImage*, 85:51–63, 2014.

[63] Rickson C Mesquita, Turgut Durduran, Guoqiang Yu, Erin M Buckley, Meeri N Kim, Chao Zhou, Regine Choe, Ulas Sunar, and Arjun G Yodh. Direct measurement of tissue blood flow and metabolism with diffuse optics. *Philosophical Transactions of the Royal Society A: Mathematical, Physical and Engineering Sciences*, 369(1955):4390–4406, 2011.

[64] J David Briers. Laser Doppler, speckle and related techniques for blood perfusion mapping and imaging. *Physiological measurement*, 22(4):R35, 2001.

[65] Joseph W Goodman. Statistical optics. *New York, Wiley-Interscience, 1985, 567 p.*, 1, 1985.

[66] R. Bandyopadhyay, AS Gittings, SS Suh, PK Dixon, and DJ Durian. Speckle-visibility spectroscopy: A tool to study time-varying dynamics. *Review of scientific instruments*, 76(9): 093110–093110, 2005.

[67] Pavel Zakharov, Andreas Völker, Alfred Buck, Bruno Weber, and Frank Scheffold. Quantitative modeling of laser speckle imaging. *Optics letters*, 31(23):3465–3467, 2006.

[68] Charles S Johnson and Don A Gabriel. *Laser light scattering*. Courier Dover Publications, 2012.

[69] J David Briers and Sian Webster. Laser speckle contrast analysis (LASCA): a nonscanning, full-field technique for monitoring capillary blood flow. *Journal of biomedical optics*, 1(2): 174–179, 1996.

[70] Simon R Arridge. Optical tomography in medical imaging. *Inverse problems*, 15(2):R41, 1999.

[71] Simon R Arridge and John C Schotland. Optical tomography: forward and inverse problems. *Inverse Problems*, 25(12): 123010, 2009. URL http://stacks.iop.org/0266-5611/25/i=12/a=123010.

[72] Hari M Varma, AK Nandakumaran, and RM Vasu. Study of turbid media with light: Recovery of mechanical and optical properties from boundary measurement of intensity autocorrelation of light. *JOSA A*, 26(6):1472–1483, 2009.

[73] Akambadath Keerthiyil Nandakumaran, Hari M Varma, and RM Vasu. Analysis of the inverse problem associated with diffuse correlation tomography. *Journal| MESA*, 3(1): 79–97, 2012.

[74] Simon R Arridge. Methods in diffuse optical imaging. *Philosophical Transactions of the Royal Society A: Mathematical, Physical and Engineering Sciences*, 369(1955):4558–4576, 2011.

[75] Hari M. Varma, Claudia P. Valdes, Anna K. Kristoffersen, Joseph P. Culver, and Turgut Durduran. Speckle contrast

optical tomography: A new method for deep tissue three-dimensional tomography of blood flow. *Biomed. Opt. Express*, 5(4):1275–1289, Apr 2014. doi: 10.1364/BOE.5.001275. URL http://www.opticsinfobase.org/boe/abstract.cfm?URI=boe-5-4-1275.

[76] Mehmet Süzen, Alexia Giannoula, and Turgut Durduran. Compressed sensing in diffuse optical tomography. *Optics express*, 18(23):23676–23690, 2010.

[77] Joseph P Culver, Andrew M Siegel, Jonathan J Stott, and David A Boas. Volumetric diffuse optical tomography of brain activity. *Optics letters*, 28(21):2061–2063, 2003.

[78] Heinz Werner Engl, Martin Hanke, and Andreas Neubauer. *Regularization of inverse problems*, volume 375. Springer, 1996.

[79] Andrew K Dunn, Anna Devor, Hayrunnisa Bolay, Mark L Andermann, Michael A Moskowitz, Anders M Dale, and David A Boas. Simultaneous imaging of total cerebral hemoglobin concentration, oxygenation, and blood flow during functional activation. *Optics letters*, 28(1):28–30, 2003.

[80] Janos Luckl, Wesley Baker, Zheng-Hui Sun, Turgut Durduran, Arjun G Yodh, and Joel H Greenberg. The biological effect of contralateral forepaw stimulation in rat focal cerebral ischemia: a multispectral optical imaging study. *Frontiers in neuroenergetics*, 2, 2010.

[81] Wesley B Baker, Zhenghui Sun, Teruyuki Hiraki, Mary E Putt, Turgut Durduran, Martin Reivich, Arjun G Yodh, and Joel H Greenberg. Neurovascular coupling varies with level of global cerebral ischemia in a rat model. *Journal of Cerebral Blood Flow & Metabolism*, 33(1):97–105, 2012.

[82] Xiaoli Sun, Pengcheng Li, Weihua Luo, Shangbing Chen, Nengyun Feng, Jia Wang, and Qingming Luo. Investigating the effects of dimethylsulfoxide on hemodynamics during cortical spreading depression by combining laser speckle imaging with optical intrinsic signal imaging. *Lasers in surgery and medicine*, 42(9):809–815, 2010.

[83] Nicolas Brieu, Eric Beaumont, Simon Dubeau, Julien Cohen-Adad, and Frederic Lesage. Characterization of the hemodynamic response in the rat lumbar spinal cord using intrinsic optical imaging and laser speckle. *Journal of Neuroscience Methods*, 191(2):151–157, 2010. ISSN 0165-0270. doi: 10.1016/j.jneumeth.2010.06.012. URL http://www.sciencedirect.com/science/article/pii/S0165027010003158.

[84] Abhishek Rege, Kartikeya Murari, Alan Seifert, Arvind P Pathak, and Nitish V Thakor. Multiexposure laser speckle contrast imaging of the angiogenic microenvironment. *Journal of biomedical optics*, 16(5):056006–056006, 2011.

[85] Syed Mohammad Shams Kazmi, Ashwin B Parthasarthy, Nelly E Song, Theresa A Jones, and Andrew K Dunn. Chronic imaging of cortical blood flow using Multi-Exposure Speckle Imaging. *Journal of Cerebral Blood Flow & Metabolism*, 33(6):798–808, 2013.

[86] Thomas C Harrison, Albrecht Sigler, and Timothy H Murphy. Simple and cost-effective hardware and software for functional brain mapping using intrinsic optical signal imaging. *Journal of neuroscience methods*, 182(2):211–218, 2009.

[87] Ryan Sun, Matthew B Bouchard, and Elizabeth Hillman. SPLASSH: Open source software for camera-based high-speed, multispectral in-vivo optical image acquisition. *Biomedical optics express*, 1(2):385–397, 2010.

[88] Johannes Schindelin, Ignacio Arganda-Carreras, Erwin Frise, Verena Kaynig, Mark Longair, Tobias Pietzsch, Stephan Preibisch, Curtis Rueden, Stephan Saalfeld, Benjamin Schmid, et al. Fiji: an open-source platform for biological-image analysis. *Nature methods*, 9(7):676–682, 2012.

[89] Alvaro Cervera, Anna M Planas, Carles Justicia, Xabier Urra, Jens C Jensenius, Ferran Torres, Francisco Lozano, and Angel Chamorro. Genetically-defined deficiency of mannose-binding lectin is associated with protection after experimental stroke in mice and outcome in human stroke. *PLoS One*, 5(2):e8433, 2010.

[90] Michael Osthoff, Mira Katan, Felix Fluri, Philipp Schuetz, Roland Bingisser, Ludwig Kappos, Andreas J Steck, Stefan T Engelter, Beat Mueller, Mirjam Christ-Crain, et al. Mannose-binding lectin deficiency is associated with smaller infarction size and favorable outcome in ischemic stroke patients. *PLoS One*, 6(6):e21338, 2011.

[91] Maciej M Markiewski and John D Lambris. The role of complement in inflammatory diseases from behind the scenes into the spotlight. *The American journal of pathology*, 171(3): 715–727, 2007.

[92] Thiruma V Arumugam, Ian A Shiels, Trent M Woodruff, D Neil Granger, and Stephen M Taylor. The role of the complement system in ischemia-reperfusion injury. *shock*, 21(5): 401–409, 2004.

[93] William B Gorsuch, Elvina Chrysanthou, Wilhelm J Schwaeble, and Gregory L Stahl. The complement system in ischemia–reperfusion injuries. *Immunobiology*, 217(11):1026–1033, 2012.

[94] Anthony L D'Ambrosio, David J Pinsky, and E Sander Connolly. The role of the complement cascade in ischemia/reperfusion injury: implications for neuroprotection. *Molecular medicine*, 7(6):367, 2001.

[95] Xavier de la Rosa, Alvaro Cervera, Anna K Kristoffersen, Claudia P Valdés, Hari M Varma, Carles Justicia, Turgut Durduran, Ángel Chamorro, and Anna M Planas. Mannose-Binding Lectin Promotes Local Microvascular Thrombosis After Transient Brain Ischemia in Mice. *Stroke*, 45(5):1453–1459, 2014.

[96] Xavier De La Rosa. *Efectes de la reperfusiò després de la isquèmia cerebral: Proteines d'estrès cel lular, estrès oxidatiu i activació del complement*. PhD thesis, Facultat de Medicina, 2014.

[97] R Sastry, J-S Wang, DC Brown, RAB Ezekowitz, AI Tauber, and KN Sastry. Characterization of murine mannose-binding protein genes Mbl1 and Mbl2 reveals features com-

mon to other collectin genes. *Mammalian Genome*, 6(2):103–110, 1995.

[98] Shuai Yuan, Anna Devor, David A Boas, and Andrew K Dunn. Determination of optimal exposure time for imaging of blood flow changes with laser speckle contrast imaging. *Applied optics*, 44(10):1823–1830, 2005.

[99] Chao Zhou, Tomokazu Shimazu, Turgut Durduran, Janos Luckl, Daniel Y Kimberg, Guoqiang Yu, Xiao-Han Chen, John A Detre, Arjun G Yodh, and Joel H Greenberg. Acute functional recovery of cerebral blood flow after forebrain ischemia in rat. *Journal of Cerebral Blood Flow & Metabolism*, 28 (7):1275–1284, 2008.

[100] DP Kernick, JE Tooke, and AC Shore. The biological zero signal in laser Doppler fluximetry–origins and practical implications. *Pflügers Archiv*, 437(4):624–631, 1999.

[101] Abraham Martín, Emilie Macé, Raphael Boisgard, Gabriel Montaldo, Benoit Thézé, Mickael Tanter, and Bertrand Tavitian. Imaging of perfusion, angiogenesis, and tissue elasticity after stroke. *Journal of Cerebral Blood Flow & Metabolism*, 32(8):1496–1507, 2012.

[102] Anna Devor, Sava Sakadžić, Vivek J Srinivasan, Mohammad A Yaseen, Krystal Nizar, Payam A Saisan, Peifang Tian, Anders M Dale, Sergei A Vinogradov, Maria Angela Franceschini, et al. Frontiers in optical imaging of cerebral blood flow and metabolism. *Journal of Cerebral Blood Flow & Metabolism*, 32(7):1259–1276, 2012.

[103] Martin J. Leahy, Joey G. Enfield, Neil T. Clancy, Jim O Doherty, Paul McNamara, and Gert E. Nilsson. Biophotonic methods in microcirculation imaging. *Medical Laser Application*, 22(2):105–126, 2007.

[104] Vinayakrishnan Rajan, Babu Varghese, Ton G van Leeuwen, and Wiendelt Steenbergen. Review of methodological developments in laser Doppler flowmetry. *Lasers in medical science*, 24(2):269–283, 2009.

[105] J.D. Briers. Laser speckle contrast imaging for measuring blood flow. *Optica Applicata*, 37(1/2):139, 2007.

[106] David A. Boas and Andrew K. Dunn. Laser speckle contrast imaging in biomedical optics. *Journal of Biomedical Optics*, 15 (1):011109, 2010.

[107] Renzhe Bi, Jing Dong, and Kijoon Lee. Deep tissue flowmetry based on diffuse speckle contrast analysis. *Opt. Lett.*, 38 (9):1401–1403, May 2013. doi: 10.1364/OL.38.001401. URL http://ol.osa.org/abstract.cfm?URI=ol-38-9-1401.

[108] Renzhe Bi, Jing Dong, and Kijoon Lee. Multi-channel deep tissue flowmetry based on temporal diffuse speckle contrast analysis. *Opt. Express*, 21(19):22854–22861, Sep 2013. doi: 10.1364/OE.21.022854. URL http://www.opticsexpress.org/abstract.cfm?URI=oe-21-19-22854.

[109] Ashwin B Parthasarathy, W James Tom, Ashwini Gopal, Xiaojing Zhang, and Andrew K Dunn. Robust flow measurement with multi-exposure speckle imaging. *Optics Express*, 16(3):1975–1989, 2008.

[110] Claudia P Valdes, Hari M Varma, Anna K Kristoffersen, Tanja Dragojevic, Joseph P Culver, and Turgut Durduran. Speckle contrast optical spectroscopy, a non-invasive, diffuse optical method for measuring microvascular blood flow in tissue. *Biomedical optics express*, 5(8):2769–2784, 2014.

[111] AF Fercher and JD Briers. Flow visualization by means of single-exposure speckle photography. *Optics Communications*, 37(5):326–330, 1981.

[112] S. Yuan. *Sensitivity, noise and quantitative model of laser speckle contrast imaging*. PhD thesis, Tufts University, 2008.

[113] MCW van van Rossum and Th M Nieuwenhuizen. Multiple scattering of classical waves: microscopy, mesoscopy, and diffusion. *Reviews of Modern Physics*, 71(1):313, 1999.

[114] Vadim A Markel and John C Schotland. On the convergence of the Born series in optical tomography with diffuse light. *Inverse problems*, 23(4):1445, 2007.

[115] Joseph P Culver, Turgut Durduran, Daisuke Furuya, Cecil Cheung, Joel H Greenberg, and AG Yodh. Diffuse optical tomography of cerebral blood flow, oxygenation, and metabolism in rat during focal ischemia. *Journal of cerebral blood flow & metabolism*, 23(8):911–924, 2003.

[116] B.C White. *Developing high-density diffuse optical tomography for neuroimaging*. PhD thesis, Whasington University in Sant Louis, 2012.

[117] Claudia Valdés and Efraín Solarte. Coherence measurements of a Nd-YAG laser by image processing of Michelson interferometer fringe patterns. In *ICO20: Lasers and Laser Technologies*, volume 6028, pages 60281F–60281F–6, 2005. doi: 10.1117/12.667189. URL http://dx.doi.org/10.1117/12.667189.

[118] John Canny. A computational approach to edge detection. *Pattern Analysis and Machine Intelligence, IEEE Transactions on*, PAMI-8(6):679–698, 1986.

[119] Fang Huang, Tobias MP Hartwich, Felix E Rivera-Molina, Yu Lin, Whitney C Duim, Jane J Long, Pradeep D Uchil, Jordan R Myers, Michelle A Baird, Walther Mothes, et al. Video-rate nanoscopy using sCMOS camera-specific single-molecule localization algorithms. *Nature methods*, 10(7):653–658, 2013.

[120] Cecil Cheung, Joseph P Culver, Kasushi Takahashi, Joel H Greenberg, and AG Yodh. In vivo cerebrovascular measurement combining diffuse near-infrared absorption and correlation spectroscopies. *Physics in medicine and biology*, 46(8):2053, 2001.

[121] Stephen T Flock, Steven L Jacques, Brian C Wilson, Willem M Star, and Martin JC van Gemert. Optical properties of Intralipid: a phantom medium for light propagation studies. *Lasers in Surgery and Medicine*, 12(5):510–519, 1992.

[122] Alessandro Torricelli, Davide Contini, Antonio Pifferi, Matteo Caffini, Rebecca Re, Lucia Zucchelli, and Lorenzo

Spinelli. Time domain functional NIRS imaging for human brain mapping. *Neuroimage*, 85:28–50, 2014.

[123] *ORCA-R2 Technical Note*. Hamamatsu, Japan, 2008.

[124] M.A. O'Leary. *Imaging with diffuse photon density waves*. PhD thesis, University of Pennsylvania, 1996.

[125] Guoqiang Yu, Turgut Durduran, Gwen Lech, Chao Zhou, Britton Chance, Emile R Mohler, and Arjun G Yodh. Time-dependent blood flow and oxygenation in human skeletal muscles measured with noninvasive near-infrared diffuse optical spectroscopies. *J. Biomed. Opt.*, 10(2):024027–02402712, 2005.

[126] Amaan Mazhar, David J. Cuccia, Tyler B. Rice, Stefan A. Carp, Anthony J. Durkin, David A. Boas, Bernard Choi, and Bruce J. Tromberg. Laser speckle imaging in the spatial frequency domain. *Biomed. Opt. Express*, 2(6):1553–1563, Jun 2011. doi: 10.1364/BOE.2.001553. URL http://www.opticsinfobase.org/boe/abstract.cfm?URI=boe-2-6-1553.

[127] JF Dunn, KR Forrester, L Martin, J Tulip, and RC Bray. A transmissive laser speckle imaging technique for measuring deep tissue blood flow: an example application in finger joints. *Lasers in surgery and medicine*, 43(1):21–28, 2011.

[128] Heng He, Ying Tang, Fangyuan Zhou, Jia Wang, Qingming Luo, and Pengcheng Li. Lateral laser speckle contrast analysis combined with line beam scanning illumination to improve the sampling depth of blood flow imaging. *Optics letters*, 37(18):3774–3776, 2012.

[129] JD McKinney, MA Webster, KJ Webb, and AM Weiner. Characterization and imaging in optically scattering media by use of laser speckle and a variable-coherence source. *Optics Letters*, 25(1):4–6, 2000.

[130] Matthijs J Draijer, Erwin Hondebrink, Ton G van Leeuwen, and Wiendelt Steenbergen. Connecting laser Doppler perfusion imaging and laser speckle contrast analysis. In *Biomed-*

ical Optics (BiOS) 2008, pages 68630C–68630C. International Society for Optics and Photonics, 2008.

[131] Michael Atlan, Michel Gross, Benoit C Forget, Tania Vitalis, Armelle Rancillac, and Andrew K Dunn. Frequency-domain wide-field laser Doppler in vivo imaging. *Optics letters*, 31 (18):2762–2764, 2006.

[132] T Binzoni, TS Leung, D Boggett, and D Delpy. Non-invasive laser Doppler perfusion measurements of large tissue volumes and human skeletal muscle blood RMS velocity. *Physics in medicine and biology*, 48(15):2527, 2003.

[133] Gregor Dietsche, Markus Ninck, Christian Ortolf, Jun Li, Franck Jaillon, and Thomas Gisler. Fiber-based multispeckle detection for time-resolved diffusing-wave spectroscopy: characterization and application to blood flow detection in deep tissue. *Applied Optics*, 46(35):8506–8514, 2007.

[134] Sean J Kirkpatrick, Donald D Duncan, and Elaine M Wells-Gray. Detrimental effects of speckle-pixel size matching in laser speckle contrast imaging. *Optics letters*, 33(24):2886–2888, 2008.

[135] JC Ramirez-San-Juan, R Ramos-Garcia, G Martinez-Niconoff, and B Choi. Simple correction factor for laser speckle imaging of flow dynamics. *Optics Letters*, 39(3):678–681, 2014.

PUBLICATIONS

Some ideas and figures have appeared previously in the following publications:

Hari M. Varma, Claudia P. Valdes, Anna K. Kristoffersen, Joseph P. Culver, and Turgut Durduran. Speckle contrast optical tomography: A new method for deep tissue three-dimensional tomography of blood flow. *Biomed. Opt. Express*, 5(4):1275-1289, 2014.

Xavier de la Rosa, Alvaro Cervera, Anna K. Kristoffersen, Claudia P. Valdés, Hari M. Varma, Carles Justicia, Turgut Durduran, Ángel Chamorro, and Anna M Planas. Mannose-Binding Lectin Promotes Local Microvascular Thrombosis After Transient Brain Ischemia in Mice. *Stroke*, 45(5):1453-1459, 2014.

Claudia P. Valdes, Hari M. Varma, Anna K. Kristoffersen, Tanja Dragojević, Joseph P. Culver, and Turgut Durduran. Speckle contrast optical spectroscopy, a non-invasive, diffuse optical method for measuring microvascular blood flow in tissue. *Biomed. Opt. Express*, 5(8):2769-2784, 2014.

COLOPHON

This document was typeset using the typographical look-and-feel `classicthesis` developed by André Miede. The style was inspired by Robert Bringhurst's seminal book on typography *"The Elements of Typographic Style"*. `classicthesis` is available for both LaTeX and LyX:

http://code.google.com/p/classicthesis/

Final Version as of October 27, 2014